COUPLED EQUIVALENT CIRCUIT MODEL FOR FLUID FLOW AND HEAT TRANSFER IN LARGE CONNECTED MICROCHANNEL NETWORKS

MOU NASI

(M.Eng. Shandong University, China)

A THESIS SUBMITTED

FOR THE DEGREE OF DOCTOR OF PHILOSOPHY

DEPARTMENT OF MECHANICAL ENGINEERING

NATIONAL UNIVERSITY OF SINGAPORE

2016

DECLARATION

I hereby declare that this thesis is my original work and it has been written by me in its entirely. I have duly acknowledged all the sources of information which have been used in this thesis.

This thesis has also not been submitted for any degree in any university previously.

Mou Nasi , 13 Jan, 2016

Mou Nasi

13 January 2016

ACKNOWLEDGEMENTS

I would like to express my sincere gratitude to my supervisor, Prof. Lee Poh Seng, for his guidance and support during my years at National University of Singapore (NUS). I would also like to thank my co-supervisor Prof. Saif A. Khan for his encouragement and support in this research collaboration. They have been playing very important roles in my professional development. Their professionalism and high standard in research always encourage and inspire me throughout the whole course of my study.

I would like to acknowledge the financial support received from NUS, and the MOE Academic Research Fund (AcRF) – Tier 2 research project for the support in the development of work in various ways.

I would like to thank my research group members particularly Prof. Jin Liwen, Dr. Fan Yan, Dr. Lee Yong Jiun, Dr. Pawan Kumar Singh, Dr. Hassanali Ghaedamini, Dr. Mrinal Jagirdar, Dr. Sun Chuan, Liang Tian Shen, Kong Xin Xian, Omer Bugra Kanargi, Pradeep Kumar Bal, Zeng Shi and Wu Tianqing for their discussions and inputs to this work. I also would like to thank Dr. Bernard Saw Lip Huat and Dr. Tong Wei for their friendship.

I would like to acknowledge our lab technologist Ms. Roslina Abdullah for her help in purchasing equipment and creating a good environment in Thermal

Process Lab 2.

I am especially grateful to my husband Dr. Ye Yonghuang and all my family members for their supreme support and encouragement. Without them, my dream would not have come true.

TABLE OF CONTENTS

SUMMARY

A coupled equivalent circuit model, which exploits the electric-hydraulic analogy and electric-thermal analogy, is developed to predict the mass flow distribution and temperature distribution in an oblique fin array used in enhanced heat transfer applications. Methods to obtain accurate correlations for calculation of flow-dependent hydraulic ‘resistances’ are outlined and developed for both primary and secondary channels in the oblique fin array. Appropriate Nusselt number correlations and thermal resistance models are also employed to predict the temperature distribution associated with the mass flow distribution. Detailed full-domain numerical (CFD) simulations, which are experimentally validated by micro particle image velocity (μPIV) in this study, are performed to obtain parameters for the hydraulic resistance correlations, and also to serve as benchmarks for the proposed equivalent circuit model. Detailed comparisons between the results of simplified model and numerical simulation showed that the simplified model can accurately predict the mass flow distribution and temperature distribution, within ±5%, for varying fin number, aspect ratio, fin pitch, fin length, oblique angle and inlet velocity. Slightly higher deviations of mass flow prediction are observed for high inlet velocities as a result of the presence of vortices close to the trailing edge of the oblique fin region.

The further numerical validation of coupled equivalent circuit model in variable pitch oblique fin microchannel heat sink and novel spiral microchannel heat sink with

curved cuts was conducted. Detailed comparisons between the results of reduced model and numerical simulation show that the coupled equivalent circuit model is able to accurately predict the mass flow distribution in variable pitch oblique fin arrays and the temperature distribution for heat sinks with small heat flux difference imposed. For more complex cases like heat sinks with large heat flux difference and non-pure pressure driving flow, additional models are required to improve the accuracy.

The findings of this work could be used to establish a fast and computationally efficient method to predict the performance of oblique fin arrays thus facilitating the design and optimization. More importantly, this work serves as an example of representing complicated spatio-temporally varying heat and mass flows in the form of simpler, lumped circuit models. Thus, the reduced equivalent circuit model is generally applicable for studies on fluid flow and heat transfer performance of microchannel heat sinks and can potentially facilitate the optimization of various configurations for heat transfer enhancement.

LIST OF TABLES

LIST OF FIGURES

NOMENCLATURE

A_{eq}	Area of cross section, m^2
B	Precision error
a	Short side length of rectangular channel, m
b	Long side length of rectangular channel, m
C	Constants
D	Diameter
D_h	Hydraulic diameter, m
E	Total error
H	Channel height, m
h	Convective heat transfer coefficient, $W/m^2 \cdot K$
I	Electrical current, A
k	thermal conductivity, $W/m \cdot K$
L	Length, m
M	Local magnification factor
Nu	Nusselt number
P	Perimeter, m
Po	Poiseuille number
Q	Mass flow rate, kg/s
q	Rage of heat flow, W
R	Resistance, Ω
R_{hyd}	Hydraulic resistance, $Pa \cdot s/kg$
R_t	Thermal resistances, K/W
Re	Reynolds number
S	Bias error
V	Electrical potential, V
f	Apparent friction factor
l	Fin length, m
l_u	Fin pitch, m
m	Number of fin per row
n	Number of fin row
p	Pressure, Pa
u	Velocity, m/s
u_∞	Free stream velocity, m/s
W_b	Curved secondary channel width, mm

W_f	Spiral fin width, *mm*
W_s	Spiral channel width, *mm*
w_{ch}	main channel width, *m*
w_{ob}	oblique channel width, *m*
w_w	fin width, *m*

Greek symbols

α	Aspect ratio
θ	Oblique angle, ^{o}
Δ	Gradient
μ	Dynamic viscosity, $Pa \cdot s$
ρ	Mass density, kg/m^3
v	Kinematic viscosity, m^2/s

Subscripts

ch	Channel
m	Mean
main	Main channel
sec	Secondary channel
ob	Oblique channel

Publication arising from this thesis

Journal Papers

1. **N. Mou,** YJ Lee, PS Lee, P Singh, SA Khan**,** Investigations on the influence of flow migration on flow and heat transfer in Oblique Fin Microchannel Array, ASME. *J. Heat Transfer.* 2016. doi:10.1115/1.4033540.

2. **N. Mou**, P.S. Lee, S.A. Khan, Coupled equivalent circuit models for fluid flow and heat transfer in large connected microchannel networks – the case of oblique fin heat exchangers, *International Journal of Heat and Mass Transfer*, Accepted.

3. Zhong Lin Chiam, Poh Seng Lee, Pawan Kumar Singh, **Nasi Mou** , Investigation of fluid flow and heat transfer in wavy micro-channels with alternating secondary branches, *International Journal of Heat and Mass Transfer,* Accepted.

Conference Papers

1. **N Mou ,** Y Fan, LW Jin, XX, Kong, PS Lee, TS Liang, A New Design for Heat Transfer Enhancement Using Curved Cuts, *2012 International Symposium on Refrigeration Technology*, Zhu Hai.

2. **N. Mou**, P.S. Lee, S.A. Khan, A Simplified 'Effective Circuit'Fluid Flow Model for Forced Convection in Oblique Fin Configuration, *ASME 2014 International Mechanical Engineering Congress and Exposition*, American Society of Mechanical Engineers, 2014, pp. V8A-V10A

3. Fan Y., Lee P. S., Jin L. W., Chua B. W., **Mou N. S**., Jagirdar M., 2013, "A Parametrical Numerical Study in Cylindrical Oblique Fin Minichannel," *Proceedings of the ASME 2013 International Technical Conference and Exhibition on Packaging and Integration of Electronic and Photonic Microsystems, Burlingame*, CA, USA, Jul 16-18.

CHAPTER 1 INTRODUCTION

1.1. Background

As early as 1965, experts predicted that the future of integrated electronics is the future of the electronics itself and the advantage of integration will bring about a proliferation of electronics. Ever since then，the speedy development of integrated electronics has indicated the correctness of that prediction. According to the famous Moore's Law suggested by Gorden E. Moore [1], the number of transistors that could be placed inexpensively on an integrated circuit would double approximately every 18 months for more than 40 years. The continuous miniaturization of electronic devices with advanced packaging technology led to the ever-increasing packaging densities and the associated heat fluxes that need to be dissipated. Waste heat generated from electronics must be sufficiently removed to ensure that the operating temperature is kept within the optimum range. High temperature with addition of hot spot can accelerate the meantime to failure (MTTF) and reduce the lifespan of electronic devices as described by Black's equation [2]. To make the problem worse, the emerging trend of product miniaturization eliminates the useful surface area for waste heat removal, leading to serious thermal management challenges.

Microchannels offer advantage in thermal management due to their high surface to volume ratio and their small volumes. The large surface to volume ratio leads to high rate of heat and mass transfer, making microdevices excellent tools for compact heat

exchangers and heat sinks. Fluid flow through microchannels was first proposed and demonstrated as an effective means of dissipating heat from silicon integrated circuits by Tuckerman and Pease [3]. This novel idea led to a number of innovative designs and spawned extensive research efforts in the area of microchannel cooling.

From the boundary layer theory for internal flow, the thickness of boundary layer grows continuously as the fluid flows downstream. The velocity and temperature gradient on the cross-sections decreases as the thickening of boundary layers. Thus the heat transfer becomes inefficient in the fully developed region. A conventional microchannel heat sink which employs straight channels is with high possibility to meet such a heat transfer deterioration. In the long channels, flow enters and becomes fully developed within the first few diameter lengths, and then remains developed through the remainder of the channel. As a result, the fluid mixing is poor and the heat transfer becomes inefficient. Numerous research studies into new fin designs and layouts designed to improve microchannel heat sink performance highlight secondary flows as one of the most promising heat transfer augmentation techniques [4-6].

Based on this, novel oblique fin geometry, as shown in Figure 1-1 was proposed by Lee et al.[5]. By breaking the continuous fins into oblique sections, the boundary layer development is disrupted and reinitialized continuous. In the meanwhile, fluid in the adjacent main channels periodically mixes through the secondary channels. Thus, significant local and global heat transfer enhancement is achieved [7].

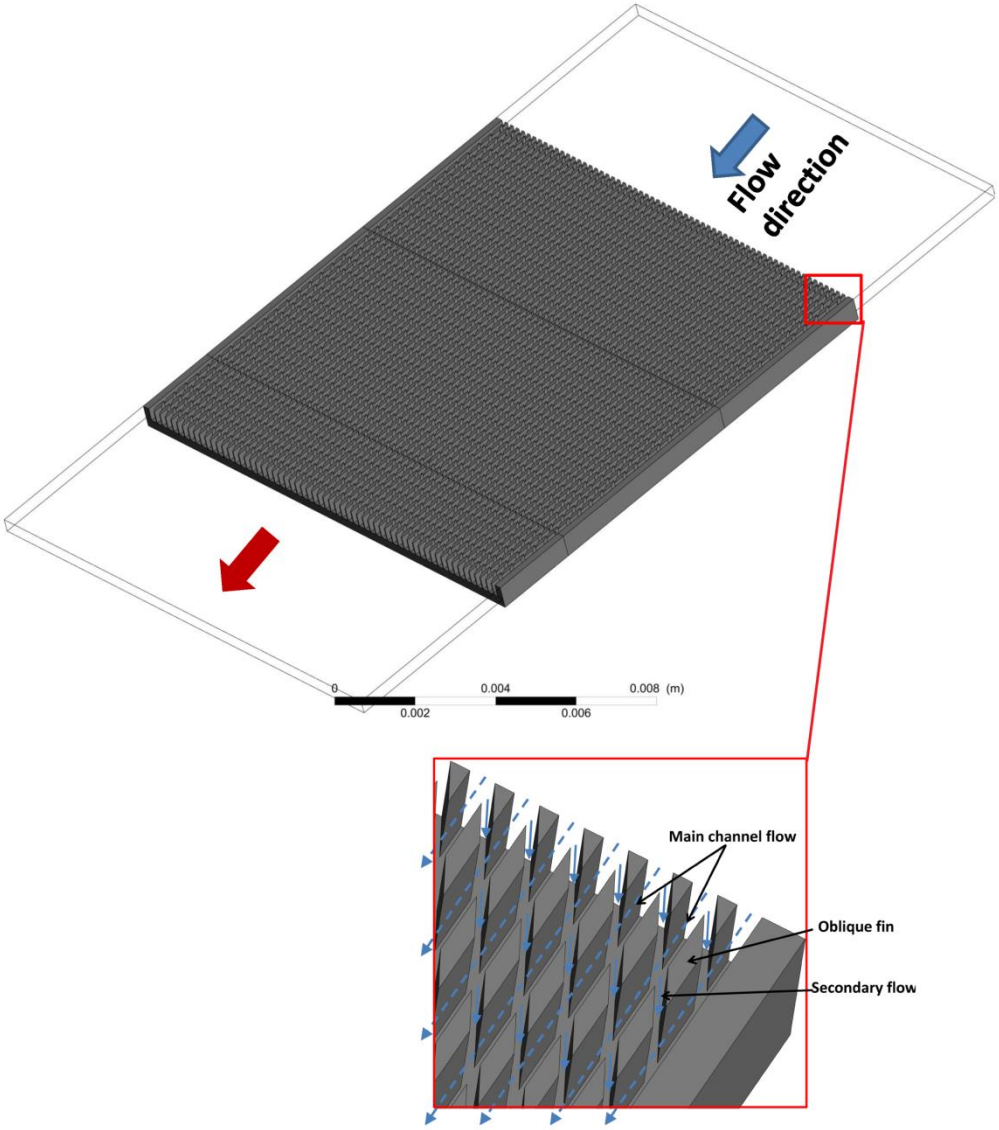

Figure 1-1 Full domain configuration for novel oblique fin minichannel heat sink

These advantages notwithstanding, the application of secondary flow to heat transfer enhancement may also have some drawbacks. As the coolant travels downstream, secondary flow generation and flow migration occurs continuously, thus leading to flow maldistribution in some configurations. Edge effects due to flow maldistribution may induce non-uniform temperature distributions along the heat sink footprint. When such a heat sink is used to cool an electrical component, the non-uniform

temperature distribution might cause uneven thermal expansion of the device and could damage its electrical performance [8]. Thus, full domain simulations are needed when conducting numerical studies on planar oblique fin arrays to capture the edge effects. However, full domain simulations are more cumbersome to set up and can be computationally expensive, which limit their use in practical engineering applications. As such, it is highly desirable to develop simplified models that are easy to use while at the same time reasonably accurate.

1.2. Objectives

The main aim of this study is to develop a reduced model to complement the full domain simulation on fluid flow and heat transfer in large connected microchannel networks. The reduced model should fulfill the following requirements: (1) to predict the flow distribution in planar secondary flow generating oblique fin configurations with certain accuracy, (2) to greatly simplify simulation procedures, (3) to shorten the simulation time and post-processing time, and (4) to reduce the dependence on computer performance.The specific objectives of this research are to:

- Experimentally validate the models and setups used for the numerical simulation investigation on novel oblique fin microchannel geometry.
- Propose a coupled equivalent circuit model to rapidly and accurately predict the mass flow distribution and temperature distribution in an oblique fin array used in enhanced heat transfer applications.

- Numerically validate the prediction of mass flow distribution and temperature distribution in planar oblique fin array from the coupled equivalent circuit model.

- Numerically investigate the availability of proposed coupled equivalent circuit model in more complex cases which contains the variable pitch oblique fin microchannel heat sink for hot spot mitigation and novel spiral microchannel heat sink with curved cuts.

1.3. Significance and Scope of the Study

The findings of this study could be used to establish the method required to fast and efficiently predict the performance of oblique fin arrays, which can be very useful for design and optimization of the oblique fin microchannel heat sink. More generally, this study serves as an example of representing complicated spatio-temporally varying heat and mass flows in the form of simpler, lumped circuit models. Thus, our simplified nonlinear equivalent circuit model is generally applicable for studies on fluid flow and heat transfer performance of other heat sink arrays and can potentially facilitate the optimization of various configurations for heat transfer enhancement.

The present research mainly focuses on pressure driven laminar flow for single-phase cooling. An in-depth discussion of the influence of other forces such as gravity and centrifugal force is not conducted. However, the coupled equivalent circuit model should be able to capture such influences if these forces are considered in the determination of hydraulic resistances.

1.4. Organization for Dissertation

This thesis contains seven chapters in total. They are organized in the following manner.

Chapter 1 introduces the background and motivation of the research. The objectives and scope are also outlined along with the organization of the thesis.

Chapter 2 reviews the literature relevant to the present study. These include thermal applications for planar minichannel heat sink, single-phase heat transport in straight and spiral microchannels, optimization techniques for heat sinks and analogies and modeling of single-phase flow and heat transfer.

Chapter 3 provides a description on the numerical investigation and microPIV validation of fluid flow for two different novel oblique fin microchannel geometries. The objective is to validate the CFD model used for the simulation of oblique fin microchannel heat sink. The CFD approach, experimental setup, test section design, experimental procedure, and data analysis are presented in detail. The velocity profiles and pressure drop characteristics for oblique fin minichannel heat sinks are analyzed and discussed.

In Chapter 4, a reduced equivalent circuit fluid flow model is developed to rigorously and accurately predict the flow distribution in planar secondary flow generating oblique fin configurations. The highly *nonlinear* relationship between pressure drop and mass flow rate is modeled via resistive electrical circuits with nonlinear current

(flow rate)-dependent resistances. Detailed numerical simulations are employed to fit parameters in correlations for the hydraulic resistances of main and secondary channels, and also for subsequent model validation. Detailed comparisons between the results of reduced model and numerical simulation are presented.

In Chapter 5, a reduced equivalent circuit thermal model is developed to predict temperature distribution in an oblique fin array used in enhanced heat transfer applications. Appropriate Nusselt number correlations and thermal resistance models are employed to predict the temperature distribution associated with the mass flow distribution obtained from the equivalent circuit flow model described in Chapter 4. Detailed full-domain numerical (CFD) simulations are performed to serve as benchmarks for the proposed equivalent circuit model. Detailed comparisons between the results of reduced model and numerical simulation are performed.

Chapter 6 examines the application of coupled equivalent circuit model in predicting fluid flow and heat transfer in oblique fin microchannel heat sinks with varying fin pitch and non-uniform heat flux distribution on the substrate base and in novel spiral microchannel heat sink with curved cuts.

Chapter 7 provides the key conclusions and recommendations for future works.

CHAPTER 2 LITERATURE REVIEW

In this chapter, planar heat sources such as integrated circuit chips, LED, solar absorbers and their methods of heat removal are reviewed. In addition, various studies in developing effective heat removal techniques are presented and evaluated in terms of their performance and reliability. These include single-phase heat transfer in straight and spiral micro/mini channels, and optimization techniques for heat sinks. In the last section of this chapter, various analogies and models for single-phase fluid flow and heat transfer are reviewed.

2.1. Thermal Applications of Heat Sink

As an effective heat removal technique, heat sinks have long been used in various thermal management systems. The development of packaging technique and advancement of power capacity which have led to higher and more concentrated heat flux drive the rapid advance of a variety of heat removal techniques. Among all these applications, an overwhelming majority of the heat sources are of planar footprint, while the most common are rectangular or circular. The reviews in this section focus on the thermal application of planar heat sinks such as in integrated circuit chips cooling, LED cooling and solar collectors.

2.1.1. Integrated Circuit Chips

An integrated circuit (more often called an IC) is a piece of specially prepared semiconductor into which a very complex electronic circuit is etched using

photographic techniques [9]. Integrated circuits are at the heart of a majority of modern electronic devices, including computers, stereo systems, and fuel injection systems in auto-engines. Transistors are smaller than vacuum tubes, but for some of the newest electronics, for example missile guidance, they weren't small enough. The chip is typically very fragile and is normally surrounded by a tough plastic package. Electrical contact with the chip is provided through metal legs sticking out of the package.

Technical advances in packaging technology have led to smaller chip size associated with higher and more concentrated heat flux of up to hundreds even thousands of W/cm^2 [10]. In the meanwhile, industry trends have been moving towards miniaturization of electronics and cloud computing that require more power-efficient and reliable IC systems. Moore's law has described this as an exponential growth with a doubling of transistor numbers every 18 months [1].To further shorten global interconnect lengths, improve the circuit functionality and minimize the footprint of the chip and heterogeneous integration, 3D IC architecture incorporates are developed by incorporating multiple device layers. Although such an exponential trend cannot continue indefinitely due to fundamental limits imposed by basic physics and technology, such barriers have to be overcome by innovations. The dissipation of energy in the form of heat has long been recognized as an issue that might limit information processing. Now, however, it seems this is the barrier that is the most difficult to break. Therefore, cooling of electronic devices is a persistent challenge in package design, which involves selection of cooling method and materials as well as

design of heat sinks.

Air cooling is one of the most used cooling techniques for IC cooling, such as the fan system in most of current computers. Air cooling system is preferred because of its light weight, simplicity in design and operation and low cost. Although the increasing heat load densities also drive the continued advancement in fan designs [11-13] to address various challenges such as thinner and smaller size, power saving, higher quality and reliability, its effectives in maintaining the devices at most efficient temperature is questionable. Meanwhile, the noises made by the fans and the increasing cooling cost also limit the application of air cooling in the IC system [14, 15]. Various designs of extended surfaces (heat sinks) are also introduced to further enhance the cooling performance of air cooling system. The combined use of appropriate fans and heat sink may provide a cost-effective means to satisfy the high heat removal requirement in some cases.

Liquid cooling is the method that uses liquid such as water as the heat conductor to remove the heat from various heat sources. It is generally understood that forced-convective liquid cooling using water, which has higher thermal conductivity and specific heat capacity comparing to air, is more efficient in removing waste heat. Furthermore, the liquid cooling produces little noise because it doesn’t use fan as the active air cooling does. However, the acceleration of metal corrosion, coolant leakage and difficulty in replacement also increase the design difficulty and cost of manufacture and operation of liquid cooling system. Even so, the tremendous ability

of the combination of liquid cooling and heat sink to transfer heat away from heat sources and maintain a more uniform temperature distribution still attract vast attentions of the researchers. As the world's first liquid cooled gaming laptop, Asus ROG GX700 is able to reach all new levels of performances not yet seen in any other laptops [16].

Heat pipe is another effective method for heat dissipation. As one of the most attractive advantages of heat pipes, the thermal conductivity can be as high as 100,000W/m·K[17], which is significantly higher than that of copper around 400W/m·K. The combination of heat pipes and appropriate finned heat sink can further improve the thermal performance with a minimum of weight increase [18]. The numerical study of Elnaggar et al.[19] on a vertically mounted finned U-shape twin heat pipe showed excellent hat transfer performance. Using a combined heat pipe and thermoelectric module, the maximum temperature of a heat source of 200W can be maintained below 75 ℃[20]. However, the using of heat pipe is still considered as high cost currently.

High conductivity materials have been one of the key aspects of thermal management research. Conventionally aluminium and copper are the two most commonly used metal for thermal management, each with its pros and cons; aluminium is light but its thermal conductivity is not as good as copper. Several new materials such as carbon nanotubes (CNTs), graphite composites, metal matrix composites and phase change material have been developed over the past decade. Thereinto, CNTs and TPG

(Thermal pyrolytic graphite) material are two of the promising new materials developed for thermal management. CNTs are stable at high temperatures and their predicted heat transmission is roughly double that of pure diamond at room temperature [21]. On the other hand, the thermal conductivity of TPG is 4 times that of copper [22], lighter than aluminium and is compatible with many encapsulating technique. Combined designs of high conductivity materials and heat sinks are able to achieve high fin efficiency and very effective heat spreading.

The cooling methods reviewed above only refer to some most frequently-used techniques. On the whole, liquid cooling is attracting more and more attention compared to air cooling, while the application of heat pipe and new materials is to some extent limited due to their high cost. The design of IC cooling system should comprehensively consider the effects of multi-factors, such as thermal performance, stability and cost, while heat sink is always a cost-effective choice.

2.1.2. LED

During the last twenty years, accompanied with the developments in LED semiconductors, the LED applications have also been greatly changed from that of luminous indicator to that of illuminator. With LEDs now advancing into several lighting fields, LEDs have become one of the standard methods of producing light, joining more traditional sources such as incandescent, fluorescent and high-intensity discharge (HID) [23]. Different from the traditional lighting that the light source is usually a filament, gas discharge, or arc, the source of light in LED is a semiconductor.

This also leads to changes of the technology associated with the development of lighting, use of lighting, as well as thermal management.

In high-power lighting, the required power for LED luminaires is undergoing continuous increase, rated to 100, 200 or even 600 watt. Meanwhile, the load for heat dissipation is also becoming heavier. A numerical study was conducted by Weng et al. [24] to look into the thermal performance of various LED package designs. It concluded that due to the high power operation, suitable thermal management is mandatory to achievement and guarantee the optimal performance and reliability of the system. When passive cooling is applied, the contact pad increases in size and weight exponentially for better cooling as the heat load increases. When dissipating 12W (at 1A drive, 25℃ ambient), the size of contact pad is 3.75×7.9mm which is larger than its predecessor [25]. The consequence is escalation of costs for tooling, assembly, shipping, and installation. It turns out that active cooling (i.e., the use of fan-cooled heat sinks) can exhibit dramatic size, weight and cost reductions at those elevated power levels. For a LED light of 400-watt, the weight of required high-bay fixture might be heavier than 75 pounds if the passive cooling technique is involved, and the size would be much large. However, the weight and size could be greatly cutdown if an active-cooled version is adopted.

Considerations for active light cooling systems are mainly involves: 1) noiselessness; 2) long lifetime; 3) low power consumption; 4) low susceptibility to dust/foreign contamination; 5) ability to tolerate cyclic loading and 6) low cost. With all this issues

considered, varies thermal management designs have already developed and applied to high-power LED, such as silicon-based thermoelectric (TE) device [26], air cooling heat sinks [27-29], liquid cooling heat sinks [30], phase change heat sinks [31] and heat pipe heat sinks [32-34].

2.1.3. Solar Collector

Interest in solar energy has been growing in recent years and is considered one of the main promising alternative sources of energy to replace the fossil energy resources. Solar water heating systems are one of the major applications of solar energy and can be used for various purposes, such as heating in apartments, family houses, schools, agricultural farms, hospitals, restaurants and different industries. Flat-plate and evacuated-tube solar collectors are mostly used to collect heat for space heating, domestic hot water or cooling with absorption chillier.

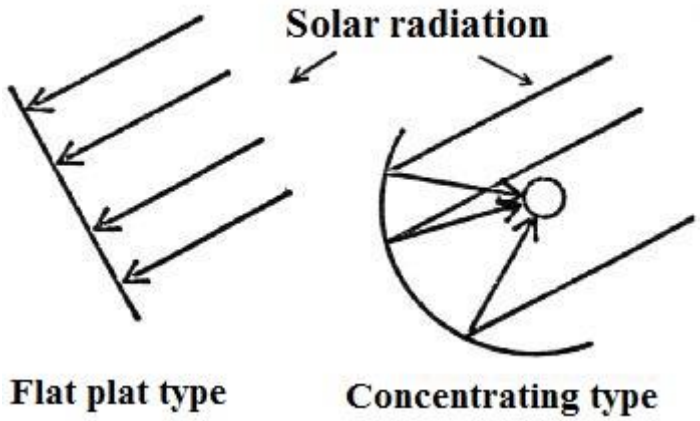

Figure 2- 1 Sketch of solar collectors

Among various designs, flat-plate collectors are the most widely used type. Typically a flat-plat collector consist of four parts: (1) a dark flat-plate absorber, (2) a

transparent cover that reduces heat losses, (3) a heat-transport fluid (air, antifreeze or water) to remove heat from the absorber, and (4) a heat insulating backing. The absorber consists of a thin absorber sheet (of thermally stable polymers, aluminum, steel or copper, to which a matte black or selective coating is applied), which is often backed by a grid or coil of fluid tubing placed in an insulated casing with a glass or polycarbonate cover. In water heat panels, fluid is circulated through tubing to transfer heat from the absorber to an insulated water tank. This may be achieved directly or through a heat exchanger.

For most air heated collector design and most water heated collected design, a completely flooded absorber consists of two sheets of metal which the fluid passes between. Such an arrangement can extend the heat exchange area, leading to marginally more efficient absorbers than traditional ones [35]. Sunlight passes through the glazing and arrives at the absorber plate. Then the absorber plate heats up, changing solar energy into heat energy. The heat is transferred to liquid passing through pipes attached to the absorber plate. Absorber plates are commonly painted with "selective coatings," which absorb and retain heat better than ordinary black paint. Absorber plates are usually made of metal—typically copper or aluminium—because the metal is a good heat conductor. Copper is more expensive, but is a better conductor and less prone to corrosion than aluminium.

Numerical analysis conducted to study thermal efficiency of flat plate solar collectors indicated that important parameters such as absorber thickness, riser position, shape

of tube cross section, absorber material, absorber absorptivity, glass transmissivity, and mass flow rate have enormous impact on the thermal efficiency of the collector [36]. A cost-effect, black liquid, flat-plate solar collector was designed by Minardi et al.[37] and its performance has attracted plenty of attention[38-41]. Solid-gas-suspensions were also use for the direct absorption of concentrated solar radiation in the early years [42]. An experimental study to determine the extinction index of four liquids (water, ethylene glycol, propylene glycol, and Therminol VP-1) was conducted by Otanicar et al.[43]. Mixing nanoparticles in a liquid (nanofluid) has been proven to have a dramatic effect on the liquid thermophysical properties such as thermal conductivity. Based on this thoughtfulness, a nanofluid-based direct absorbtion solar collector was developed [44].

Compared to the abundant studied on working fluid, the innovation in structural design is relatively rare. Although most flat-plate collectors are still tube-involved, the design concept of heat sink is also feasible. By applying a properly designed heat sink on the reverse side, the effective exposure area can also increase, thus improve the heating efficiency of solar absorber. A properly designed heat sink can also introduce high heat transfer performance, lighten the solar thermal collector, and increase the system efficiency.

2.2. Single-Phase Fluid Flow and Heat Transfer in Microchannels

Microchannels offer advantage due to their high surface to volume ratio and their small volumes. The large surface to volume ratio leads to high rate of heat and mass

transfer, making microdevices excellent tools for compact heat exchangers and heat sinks. Fluid flow through microchannels was first proposed and demonstrated as an effective means of dissipating heat from silicon integrated circuits by Tuckerman and Pease [3]. This novel idea led to a number of innovative designs and spawned extensive research efforts in the area of microchannel cooling. The first demonstration involved the design and testing of a very compact water-cooled integral heat sink fabricated into silicon. Microscopic channels in 50 μm width and 300 μm depth were etched on silicon, and deionized water was pumped through as the coolant. A power density of 790 W/cm^2 was achieved with a corresponding substrate temperature rise of 71 °above the inlet water temperature.

The application of microchannels to electronics cooling imposes severe design constraints on the system design. For a given heat dissipation rate, the flow rate, pressure drop, fluid temperature rise, and fluid inlet to surface temperature difference requirements necessitate optimization of microchannel geometry. A numbers of investigators have studied the geometrical optimization of microchannel heat exchangers.

2.2.1. Single-phase Fluid Flow and Heat Transfer in Straight Microchannels

Water flow through a circular microchannel was studied by Sharp et al.[45] with the Reynolds number varying from 50-2500 and a good agreement of friction factor between the measured values and that calculated from the conventional theory was observed. The results of experimental investigations on aluminium microchannels

with the hydraulic diameters varying from 46.8 to 344.3μm and copper microchannels with hydraulic diameters varying from 29.29 to 79.08 μm by Xu et al.[46] also showed good agreement with the conventional results obtained by using the Navier–Stokes equation for an incompressible, Newtonian fluid in the laminar regime. However, the study by Ding et al.[47] found that the friction factor for R134a and R12 in a triangular and a rectangular microchannel with a hydraulic diameter of 400 and 600μm was higher than the conventional prediction, while the studies on microchannels with much smaller hydraulic dimensions showed smaller friction factor than the conventional prediction [48]. A similar deviation trend was also observed by Judy et al.[49]. The studies on the friction characteristic of air, water and liquid refrigerant R134a through ten circular microchannels with a diameter from 173 to 4010 μm by Yang et al.[50] observed the friction factor for water and refrigerant R134a agreed very well with the conventional theory in the laminar and in the turbulent regime while for air flow in the turbulent regime the measured friction factors were significantly lower than those predicted by the conventional theory The effects of channel height on hydrodynamics and heat transfer in 2D mini and microchannels were experimentally studied by Gao et al.[51]. For the various channel sizes from 0.1mm to 1mm, the overall friction coefficient and local Nusselt numbers were measured and showed that: 1) the classical laws of hydrodynamics and heat transfer are verified for channel height larger than 0.4 mm; 2) for lower values of channel height, a significant decrease of the Nusselt number is observed whereas the Poiseuille number keeps the conventional value of laminar developed flow; 3) the

transition to turbulence is not affected by the channel size. From all the open literatures, we can concluded that for the water flow in microchannels made of copper, aluminum and silicon, the friction factor for laminar flow is still feasible for most cases, while for gaseous cases the situations would be more complicated and most conclusions are conflicting. A comparison studies on convective heat transfer in flat microchannels also yield conflicting conclusions. The conventional laws and correlations describing the convective heat transfer in ducts of large dimension are directly applicable to the microchannels under some research conditions[52-54] while the contrary is also true under other conditions[55-57].

With the help of 3D numerical simulation, Li et al. [58] optimized the geometric parameters of a water-cooled silicon microchannel heat sink based on the minimized thermal resistance. It was shown that for a constant pumping power, the overall cooling capacity for the optimized geometry was able to be enhanced by more than 20% compared to the initial experimental result obtained by Tuckerman et al.[3]. A similar optimization work conducted by Ryu et al. [59] demonstrated that among all design variables, the channel width appears to be the most crucial parameter determining the performance of a microchannel heat sink. Besides, both optimized dimensions and thermal resistance were found to have a power-law dependence on the pump power. On the other hand, five approximate analytical approaches were proposed and validated by the detailed computational fluid dynamics model by Liu et al. [60] to simplify the design of microchannel heat sinks. These approaches included a 1D resistance model, a fin approach, two fin-liquid coupled models, and a porous

medium approach. Although some research limitations/implications existed, the results obtained still demonstrated sufficient accuracy for practical designs and being straightforwarded to use. Lee et al. [61] then expanded the 1D thermal resistance optimization model by adopting the thermally developing Nusselt number correlation proposed by Lee et al. [62]. Their results showed that the channel width can be relaxed by 20% if the optimization is based on the assumption of thermally developing flow, which is true for most of the microchannel flow [63].

The works reviewed above revealed the importance of optimized geometries of channels in maximizing the potential of microchannel heat sink. It is however evident that producing the optimized microchannel geometries is not as easy in the actual fabrication. Saw blade or end mill required to create the optimum channel width might not be commercially available and the produced width is highly dependent on the condition of the cutting collaterals. Also, the lower part of an etched channel is usually tapered, deviating significantly from the intended rectangular profile [64] while the dimensions of an uncompensated wire-cut channel can vary from the designed value by as much as 50 μm.

From the boundary layer theory for internal flow, the thickness of boundary layer grows continuously as the fluid flows downstream. The velocity and temperature gradient on the cross-sections also decreases as the development of boundary layers. Thus the heat transfer becomes inefficient in the fully developed region. A conventional microchannel heat sink which employs straight channels is with high

possibility to meet such heat transfer deterioration. In the long channels, flow enters and becomes fully developed within the first few diameter lengths, and then remains developed through the remainder of the channel. As a result, the fluid mixing is poor and the heat transfer becomes inefficient. Besides this, significant temperature variations across the chip can persist since the heat transfer performance deteriorates in the flow direction as the boundary layers thicken. These will in turn compromise the reliability of the ICs and can lead to early failures. Therefore, various heat transfer enhancement methods have been developed for the optimization of microchannel heat sink.

2.2.2. Fluid flow and Convective Heat Transfer for In-Plane Spiral Coils

The concept of the spiral-plate heat exchanger was apparently first proposed late in the 19th century, according to Hewitt et al.[65]. Ever since then, in-plane spiral tubes have been widely used in engineering application due to their higher heat transfer performance, compact structure, and ease of manufacture, such as heat exchanger, electronic cooling, chromatography, fuel cell coolant channel, chemical reactor, and many others applications. Due to the significant effect of centrifugal forces in spiral tubes, secondary flows occur in the cross sections. Thus, transport phenomena occurring in spiral tubes are more complicated than those in straight ducts. As such, spiral tubes have attracted considerable attention from engineering researchers even though they are still currently less popular compared to helical tubes [66-70].

Dean [71, 72]was among first researchers who studied fluid flow inside a toroidal

(in-plane) constant radius duct. This study revealed that circular tubes develop a secondary flow when the Dean number exceeds a critical value. And the secondary flow changes the heat transfer and pressure drop [73]. Several experimental and numerical studies have been conducted in attempts to examine the transport phenomena in the spiral tubes.

Kalb et al.[74] performed numerical studies for uniform wall heat flux with peripherally uniform wall temperature for Dean numbers in the range of 1-1200, Prandtl numbers of 0.005-1600, and curvature ratios of 10 to 100 for fully developed velocity and temperature fields. They found that the curvature ratio parameter has insignificant effect on the average Nusselt number for any given Prandtl number. Goering et al.[75] and Naphon et al.[76] also studied the effect of curvature ratios on flow development and heat transfer in a heated horizontal curved tube with a constant wall-temperature, and found that at a given water mass flow rate, the average Nusselt number for lower curvature ratio are higher than those for higher ones across the studied range of water mass flow rate due to the increase of centrifugal force caused by the higher radius curvature. Bai et al.[77] experimentally studied turbulent heat transfer from horizontal helical coils. They concluded that as the Reynolds number is increased, the contribution of secondary flow to the heat transfer diminished and the heat transfer approaches that of a straight tube. This is due to the fact that as the Reynolds number increases the boundary layer becomes smaller. It is the large boundary layer that is shed off into the center of the tube by the secondary flow that increases the heat transfer coefficient, and this effect decreases with increasing

Reynolds number. The local heat transfer coefficient on the outer wall can be 3 to 4 times higher than that of the inner wall.

Further numerical analysis was performed by Yoo et al.[78] to investigate flow and heat transfer characteristics in spiral coiled tube heat exchanger. Radius of curvature of the spiral coiled tube was gradually increased as total rotating angle reached 12π. As the varying radius of curvature became a dominant flow parameter, three-dimensional flow analysis was performed to this flow together with different Reynolds numbers while constant wall heat flux condition was set in thermal field. From their analysis, centrifugal force due to curvature effect is found to have significant role in behavior of pressure drop and heat transfer. The centrifugal force enhances pressure drop and heat transfer to have generally higher values in the spiral coiled tube than those in the straight tube. Even then, friction factor and Nusselt number are found to follow the proportionality with square root of the Dean number. Individual effect of flow parameters of Reynolds number and curvature ratio was investigated and effect of Reynolds number is found to be stronger than that of curvature effect. A parametric study of laminar flow and heat transfer characteristics of coils made of tubes of several different cross—sections e. g. square, rectangular, half-circle, triangular, and trapezoidal were conducted by Kurnia er al.[79]. The results indicate that, on average, in-plane spiral ducts give higher heat transfer rate. However, it should be noted that for constant heat flux conditions, the heat transfer rate of in-plane spiral with rectangular, triangular and half circular cross-sections are lower than those of straight duct. They also impose significantly higher pressure drop

penalty compared to the straight duct. Hence, careful consideration of the operating conditions is important in selecting the geometry of in-plane spiral duct for heat transfer application.

Gyves et al.[80] examined the fully developed laminar flow and conjugated forced convection heat transfer in curved rectangular channels. The wall average Nusselt number is presented as a function of the wall conduction parameter, the Dean number and the channel aspect ratio. Burmeister et al. [81]numerically studied laminar flow and heat transfer in three-dimensional spiral ducts of rectangular cross-section with different aspect ratios. The boundary conditions were assumed to be axially and peripherally uniform wall heat flux and a peripherally uniform wall temperature. Hashemi et al.[82] experimentally investigated the heat transfer and pressure drop characteristics of nanofluid flow inside horizontal helical tube under constant wall flux. They studied the effect of different parameters, such as Reynolds number, fluid temperature, and nanofluid particle weight concentration, on heat transfer coefficient and pressure drop of the flow. Ghobadi et al [83] experimentally investigated the cooling performance systems employing spiral geometry using different working fluids. According to their study, the spiral geometry is able to significantly enhance heat transfer compared to a straight channel. Furthermore, the spiral channel does not increase the augmentation significantly for low flow rates. Nevertheless, the pressure drop penalty becomes more significant as the flow rate increases. In addition, the results show that there is no difference in feeding the heat sink from the side or the middle.

From the above review, it can be seen that the investigation of the single-phase heat transfer characteristics in spirally coiled heat exchangers have been relatively rare. As an efficient technique in heat transfer enhancement especially for cooling of the heat sources with circular footprint, the large pressure drop penalty is still a main drawback for the application of in-plane spiral channels compared to the straight microchannels.

2.3. Optimization of Microchannel Heat Sinks

Among numerous researches in new fin design and layout for improving microchannel heat sink performance, secondary flow is considered as one of the most promising heat transfer augmentation techniques. Steinke and Kandlikar [84] suggested two potential methods in generating secondary flow for microchannel application. The first suggestion was to add smaller channels at a certain angle between two main liquid channels. This design is widely adopted in flat tube-plate fin heat exchangers, where multiple louvered fins (to act as smaller secondary flow path) are closely formed on the plate fin (main larger flow path). Alternatively, secondary flow can also be generated by a venturi effect, by connecting the constriction area to the larger area section of an adjacent microchannel. Moreover, the use of twisted tape, helical ribs and screw threads is also effective method to improve the convective heat transfer of laminar flow in tubes [85-87]. Another effective method to produce secondary flow is to mount or punch vortex generators (VGs) on convective heat transfer surfaces [88-90]. Ahmed et al.[91] overviewed various parameters of VGs covering: attack angle of VG, geometry of VG, standard and novel types of VG,

spacing between the VG tips, number of pairs of VGs in the flow direction, rectangular or circular array arrangement of VGs, common-flow upper (CFU) or common-flow down (CFD) configuration of VG, pointing up (PU) or pointing down (PD) arrangement of VG with flow direction, Re number, channel aspect ratio, number of tubes of fin-tube heat exchanges (HE), circular or oval tubes of fin-tube HE, and location of VG respect to the tube of HE or from leading edge of the channel, which have pronounced effect on the convective heat transfer coefficient and pressure drop penalty. Offset strip-fin were also proven examples of flow disruption devices widely used in heat exchangers [92]. On the other hand, Tatsumi et al. [93] created notches on parallel plate fin arrays and these notches were either arranged parallel to each other or obliquely in the spanwise direction for comparison. Additional heat transfer enhancement techniques are also applied to the in-plane spiral coils [94, 95]. The studies showed that although the introduction of obstacles can further enhance the local heat transfer performance especially in the laminar flow region, the increase in pressure drop penalty is also inevitable, which leads to a compromise in thermal performance factor. Lee et al.[5] combined secondary flow generation and boundary layer reinitialization, and proposed the oblique fin design in microchannel heat sinks; by breaking the continuous fins into oblique sections, the heat transfer enhancement factor is close to 1.6 with Re ~ 300, compared to that of conventional microchannel heat sinks, while the pressure drop penalty is negligible. Fan et al. [6] introduced the concept of oblique fins into the design of cylindrical heat sinks and obtained a much larger average Nusselt number (75.6% larger) compared with that of conventional

straight fin heat sink.

Although a large amount of research has been done on heat sinks, the current studies are mainly focused on heat sinks with rectangular bases while for some devices such as LED heat sinks with circular bases are more befitting. Yu et al. [96] proposed a radial heat sink consist of a horizontal circular base and rectangular fins that are arranged in radial pattern. Cooler flow entering the heat sink is heated as it flows between the rectangular fins and then rise from inner region of the heat sink. For the spaces between fins increased in the radial direction, the design was mended to a structure with long fins and short fins being alternately arranged [97]. Many studies on pin-fin suggested that this is an effective technique for enhancing heat transfer performance [98-101]. Jang et al. [27] introduced the pin-fin technology into the design of heat sinks with circular bases and found that a radial heat sink with pin-fin is much lighter while maintaining a similar cooling performance to that of a plate-fin heat sink. A novel centrifugal heat sink, into which the blades of a fan are integrated between the fins of the circular heat sink, was designed by Kim et al. [28]. Due to the integration of the blades into the space between the fins, additional space for the blades of the fan is no longer required, which led to more efficient use of available cooling space.

Numerous researches into secondary flow find that Reynolds number shows profound influence in flow pattern, flow distribution and heat transfer [102-107]. According to the studies on louvered-fin arrays, as the Reynolds number increased, longer

development lengths were required to achieve certain flow periodicity[104]; thinner boundary layers were detected on fin surfaces [105] and mass flow percentage of louver channels also increased[106]. Increased Reynolds number also promoted unsteady flow and induced recirculation zones near walls, which locally increased heat transfer performance with an obvious increased pressure drop penalty.[103, 107]

These advantages notwithstanding, the application of secondary flow to heat transfer enhancement may also have some drawbacks. As the coolant travels downstream, secondary flow generation and flow migration occurs continuously, thus leading to flow maldistribution in some configurations. Edge effects due to flow maldistribution may induce non-uniform temperature distributions along the heat sink footprint. When such a heat sink is used to cool an electrical component, the non-uniform temperature distribution might cause uneven thermal expansion of the device and could damage its electrical performance [8]. Significant flow difference due to the bounding wall effect between five-fin and nineteen-fin model was found by Springer and Thole [102] in their experimental studies on flow field of louvered fins. Fan et al. [108] investigated the influences of edge effect on flow and temperature uniformities for both partly blockaded and non-blockaded oblique-finned structure on cylindrical heat source surfaces through numerical and experimental studies. The flow field and temperature distribution analysis showed that edge effect, which was present in the blockaded cylindrical oblique fin configuration, could cause the formation of localized hotspots due to the non-uniform flow distribution through the full domain minichannel heat sink. Thus, full domain simulations are needed when conducting

numerical studies on such geometries to capture the flow maldistribution effects.

However, full domain simulations are more cumbersome to set up and can be computationally expensive, which limit their use in practical engineering applications. As such, it is highly desirable to develop powerful reduced models for optimal configurations under practical design constraints.

2.4. Analogies and Modelling of Single-Phase Flow and Heat Transfer

The analogy between electrical and mechanical (including fluidic) systems has been widely used since the early last century [109]. The well-known Hagen-Poiseuille law can be used to obtain an expression for the pressure drop Δp in terms of the flow rate Q and a proportionality factor R_{hyd} which is called the hydraulic resistance. The Hagen-Poiseuille Law is completely analogous to Ohm's law which relates the electrical current I through a wire with the electrical resistance R of the wire and the electrical potential drop ΔV across the wire. Given the analogy between the Hagen-Poiseuille Law and Ohm's Law, it is quite appropriate to apply well-established methods from electric circuit theory to microchannel flow ('microfluidic') networks. Utilizing this electrical analogy, it is possible to draw the equivalent electric circuit for a given microfluidic network. Channels with hydraulic resistances R_{hyd} become resistors, flow rates Q become currents, and pumps providing the pressure differences Δp become voltage sources (or current sources). Bras et al. [110] used equivalent circuit theory involving hydraulic resistances, pressures, and flow rates to describe the low-voltage, cascade, electro-osmotic

micropump developed by Takamura er al.[111] and the results were in good agreement with the published experimental data and full CFD numerical simulation results. This analogy has also been exploited for pipeline networks for the prediction of flow distribution [112-114]. Bruus [115] listed the hydraulic resistances for straight channels with different cross-sectional shapes.

Similar to the electrical-hydraulic analogy, there exists an electrical analogy with heat transfer that can be exploited in problems solving thermal potential 'circuit' distributions. Here, heat flow rate q is analogous to current I, and the temperature difference ΔT is analogous to voltage drop ΔV.

Thermal circuit elements have long been used in the calculation of heat spreading. Calculation of spreading resistance for the situation with heat rejected into one side of a plate and extracted from the entire reverse side were discussed separately by Lee[116], Muzychka et al.[117] and Culham et al.[118], while Guenin[119] conducted a study on the situation that a plate was centrally heated and uniformly cooled in its peripheral region. In the calculation of the heat sink thermal resistance, Simons[120] introduced fin efficiency theory to calculate the thermal resistance of fin surfaces, while Kang et al.[121] further proposed a new thermal resistance model for the heat transfer from fin to fluid. The thermal heat conduction from a circular heat source to a circular conductive substrate exposed to distinct convective heat sinks on its upper and lower surfaces is treated rigorously by formally solving a mixed boundary value problem through the singular integral equation technique by Kabir et

al. [122]. The effects of the two heat sinks are consolidated into one effective heat sink that is derived by application of a current source transformation to the DC circuit representation of the problem. The spreading resistances to the upper and lower surfaces each are found to depend on the boundary conditions on both surfaces. All of the results of the spreading resistances and the source temperature are reflected in the total resistance of the homogeneous problem and the temperature weighting factor. A calculation method using an equivalent heat transfer coefficient to model fins was developed by Simons [123]. Fin efficiency theory was adopted in the calculation process. The method is very attractive in the design of compound fin heat sink structure with rectangular geometries while the application to other optimized fin geometries is limited by bottlenecks such as the determination of convective heat transfer coefficient and fluid temperature. The same limitation was also observed in the thermal equivalent circuit model developed by Drofenik et al.[124] for a forced-cooled heat sink.

The generalized Leveque equation, which was theoretically derived for the first time in André Lévêque's thesis [125], is a purely theoretical asymptotic equation for developing thermal boundary layers in fully developed laminar and turbulent channel flow. It predicts heat-transfer coefficients as being proportional to $\left(\zeta \cdot \mathrm{Re}^2\right)^{1/3}$. Holger Martin [126] used the equation to predict the performance of chevron-type plate heat exchangers and concluded that the prediction is in good agreement with experimental observations quoted in the corresponding literatures. The Leveque analogy was then adopted by Kumar et al. [127] for the exergy analysis of regenerator beds with the

pressure drop data being predicted by analysing similar data with the help of Artificial Neural Network. Further improvement of the Leveque analogy was conducted by Martin [128, 129] for the prediction of heat transfer performance of both inline and staggered tube bundles and also showed satisfactory agreement. Similar results were also obtained for the study of offset strip-fin surfaces [130], finned-tube bundles [131] and solid ceramic sponges [132]. However, there are few papers in the open literature validating its feasibility in micro-geometries and turbulent region.

The above studies have provided powerful reduced modeling approaches for optimal configurations under practical design constraints, in view of the complexity and computational expense of a full CFD approach for predicting convective heat transfer in microchannel heat sinks. They are, however, mostly limited to prediction of thermal resistances and not able to capture the temperature distribution unless when CFD models are used. Thus, it is of much interest to combine the prediction of mass flow distribution and thermal equivalent resistances, to build coupled equivalent circuit models for fluid flow and heat transfer in large connected microchannel networks.

CHAPTER 3 FULL DOMAIN NUMERICAL INVESTIGATION AND MICROPIV VALIDATION OF FLUID FLOW IN NOVEL OBLIQUE FIN MICROCHANNLES

This chapter describes the numerical investigation and micro-PIV validation of fluid flow for two different novel oblique fin microchannel geometries. In section 3.1, the details of the CFD simulation approach are provided. In section 3.2, the experiment setup, test sections, experimental procedure and uncertainty analysis will be presented in detail. In Section 3.3, simulation and experiment results are discussed. The velocity profiles and pressure drop characteristics are analyzed in detail. Lastly in Section 3.4, the conclusions for this chapter are presented.

3.1. CFD Simulation Approach

3.1.1. Simulation Model Setup

Two oblique fin microchannel geometries with different design dimensions were investigated in this study. The full simulation domains of novel oblique fin microchannel geometry Case 1 and Case 2 are shown in Figure 3-1. All dimensions are listed in Table 3-1.Extensions are applied to all inlets and outlets to be consistent with the experimental setup. Two coordinate systems are also shown in Figure 3-1, originating at the starting of the middle line of

the 11th row of main channel for Case 1 and the 6th row of main channel for Case 2 with *x* lying along the main channel and *z* in the transverse direction.

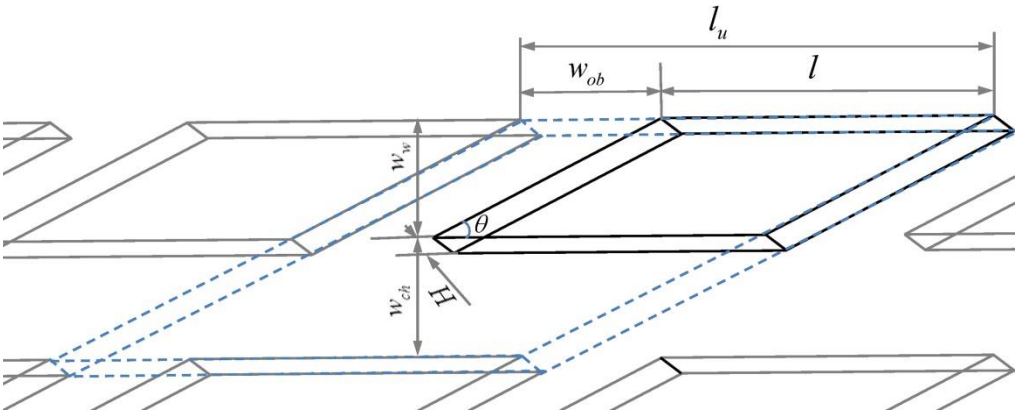

(a)

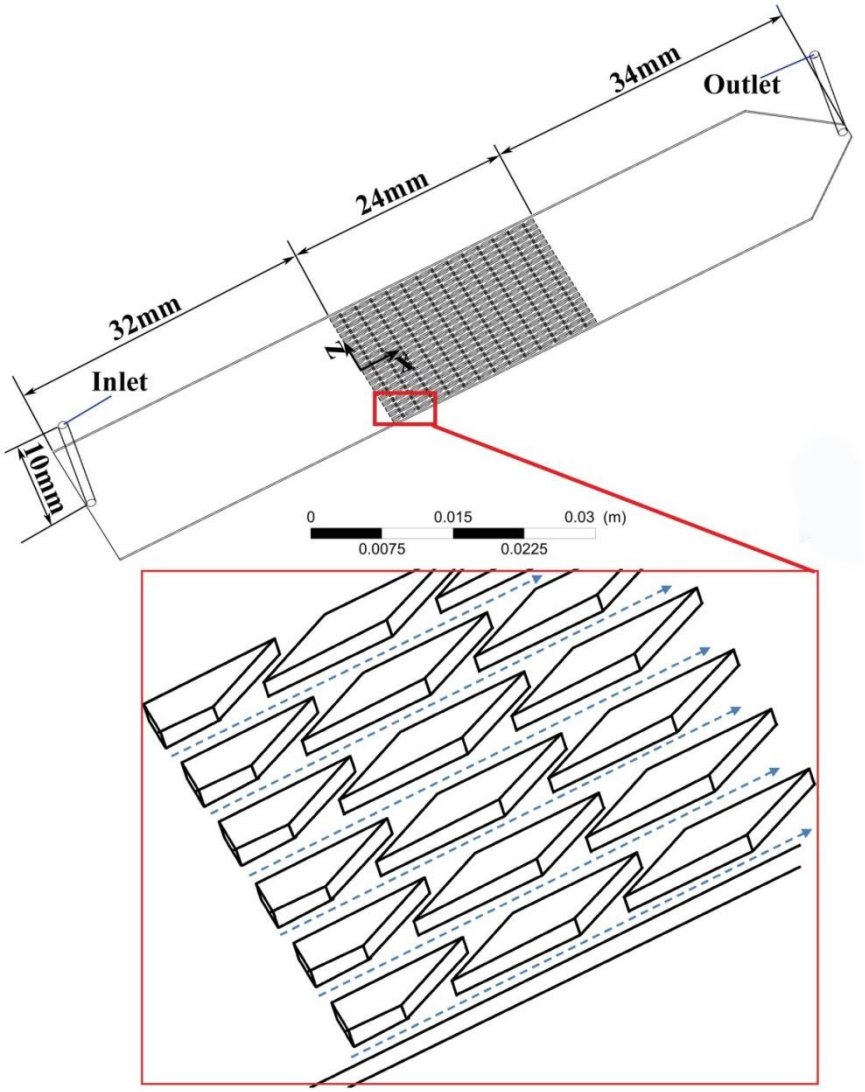

(b)

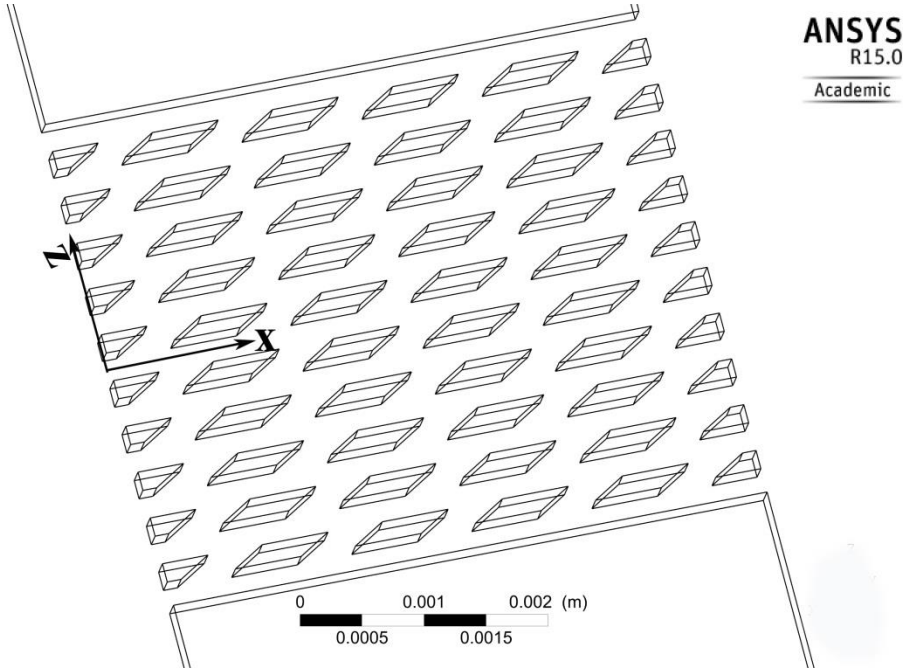

(c)

Figure 3-1 (a) Sketch of an oblique unit, and 3D computational domain of oblique fin microchannel geometry (b) Case 1; (c) Case 2

Table 3-1 Geometrical details for oblique fin microchannels

Characteristic	Case 1	Case 2
Material	PMMA	
Substrate dimension, L×W(mm)	120×50	65×45
Fin region L×W,(mm)	24×18.486	5×4.237
Number of fin rows	20	10
Channel height H, (mm)	0.216	0.105
Main channel width (mm)	0.486	0.240
Fin width (mm)	0.414	0.16
Aspect ratio, α	0.445	0.44
Number of fins per row	13	5

Fin pitch (mm)	1.8	1.012
Oblique fin length (mm)	1.289	0.554
Oblique angle θ (°)	26.4	30.8

3.1.2. Governing Equation

The commercial CFD software ANSYS–CFX is used in this work to solve the Navier–Stokes equations using a fully conservative, element-based finite volume method. To ensure robustness, CFX provides flexibility in choosing discretization schemes for each governing equation. The discretized equations, along with the initial condition and boundary conditions, were solved using the coupled method.

Take the complexity of flow in oblique fin arrays into account, steady Reynolds Averaged Navier–Stokes (RANS) equations for incompressible fluid flow with constant properties are used in this study. The governing equations of flow field are the continuity and the RANS equations, which are given by:

$$\frac{\partial u_j}{\partial x_j} = 0 \tag{3-1}$$

$$\frac{\partial u_i u_j}{\partial x_j} = -\frac{1}{\rho}\frac{\partial p}{\partial x_i} + \frac{\partial}{\partial x_j}(\nu S_{ij} - \overline{u_i' u_j'}) \quad j = 1,2,3... \tag{3-2}$$

where S_{ij} is the main strain rate and calculated by: $S_{ij} = \frac{1}{2}(\frac{\partial u_i}{\partial x_j} + \frac{\partial u_j}{\partial x_i})$, and $\overline{u_i' u_j'} = \tau_{ij}$ is Reynolds stress tensor while u_i' represents the velocity fluctuation

in *i*-direction. These terms arise from the nonlinear convection in the un-averaged equation and they reflect the fact that convective transport due to turbulent velocity fluctuations will act to enhance mixing over and above that caused by thermal fluctuations at the molecular level.

The Shear–Stress Transport $k-\omega$ model (SST) is employed to predict the flow behaviour in the present study. It is based on the following two transport equations:

$$\frac{\partial(\rho u_i k)}{\partial x_i} = \gamma P_k - \beta_1 \rho k\omega + \frac{\partial}{\partial x_i}[(\mu + \frac{\mu_t}{\sigma_k})\frac{\partial k}{\partial x_i}] \tag{3-3}$$

$$\frac{\partial(\rho u_i \omega)}{\partial x_i} = \alpha\rho S^2 - \beta_2 \rho\omega^2 + \frac{\partial}{\partial x_i}[(\mu + \frac{\mu_t}{\sigma_{\omega 1}})\frac{\partial \omega}{\partial x_i}] + 2(1-F_1)\rho\frac{1}{\sigma_{\omega 2}\omega}\frac{\partial k}{\partial x_i}\frac{\partial \omega}{\partial x_i} \tag{3-4}$$

Where $\sigma_{\omega 1}$=2, $\sigma_{\omega 2}$=1.168, β_1=0.09, k is the turbulent kinetic energy, ω is the specific dissipation that determines the scale of the turbulence, F_1 is a blending function, and it is designed to be one in the near wall region which activates the standard $k-\omega$ model, and zero away from the wall, which activates the transformed $k-\varepsilon$ model. The model also includes a slight amendment to the eddy viscosity for a better prediction of the turbulent shear stress. It could give a highly accurate prediction of the onset and the amount of flow separation under adverse pressure gradients by the inclusion of transport

effects into the formulation of the eddy-viscosity. The superior performance of this model has been demonstrated in a large number of validation studies (Bardina et al.[133]).

3.1.3. Boundary Condition

Since the Navier-Stokes equations were solved inside the domain, no-slip boundary condition was applied on the channel walls for all cases. Since the fluorescent polymer microspheres used for subsequent flow visualization were very small and should not affect the flow pattern of water, the flow media was set as pure water in the simulations. A prescribed velocity was applied at the inlet and gauge pressure at the outlet was set as 0 Pascal. A residual value of 1×10^{-6} was set as the convergence criteria for the continuity equation, x-velocity, y-velocity z-velocity and energy equation.

3.1.4. Grid Independence Study

In order to conduct an accurate computational simulation, grid independence was conducted on the oblique fin microchannel Case 1. The entire computational domain was meshed with minimum edge size of 0.02 mm and a total number of 22,850,008 elements were finally selected for the fluid domain in order to preserve both accuracy and cost after the study of grid independence. The same grid size and model set were also used to numerically simulate the configuration with 500μm nominal channel width described by

Lee et al.[134], and compared with the results from their experimental studies, as shown in Figure 3-2. It is found that the deviation between experimental and numerical simulation results is relatively small under all conditions. The same grid size was also replicated into all the simulation cases in this study.

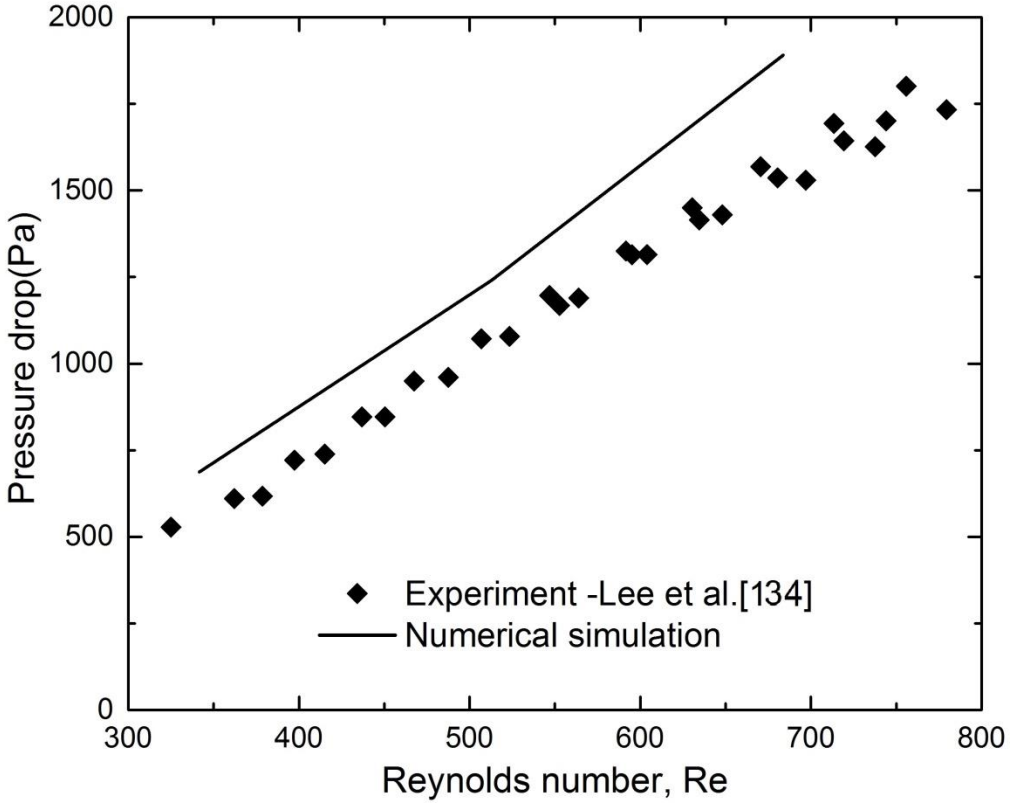

Figure 3-2 Comparison of pressure drop between numerical simulation and corresponding experiments

3.2. Experimental Setup and Procedures

3.2.1. Experimental Setup

Particle image velocimetry (PIV) is a well-established technique for measuring velocity fields in macroscopic fluid systems [135]. Positions of flow-tracing particles are recorded at two known times by illuminating the

particles using either a pulsed light source or a continuous light source gated near the camera using a mechanical or electronic shutter in a double-pulsed PIV system,. The displacement of the particles is then estimated statistically by correlating the particle image pairs [136].

Figure 3- 3 shows the schematic of the Micro-PIV setup in current experiment study. The light source is a double pulsed Nd:YAG laser that is focused by an epifluorescent microscope with a high numerical aperture on a micro-fluidic device. The lasers produce light at a wavelength of 532 nm and have adjustable power settings. A microscope lens collects the particle signal that has a longer wavelength than the illuminating light. This signal is separated from the laser light by a filter cube and is recorded by a double-frame CCD camera. The double frame images are evaluated with conventional PIV algorithms. The DaVis software from LaVision was used to synchronize the camera and laser. Safety glasses were worn at all times working with the laser and a status indicator lamp was installed on the outside wall to prevent untrained staffs entering the laser room when laser is working.

The LaVision Imager Pro SX 5M, a high speed CCD camera with 5 million pixels spatial resolution and frame rates up to 15 Hz, was used to capture the images of the illuminated particles in the flow. Before imaging, the camera was calibrated. This process used a miniature channel replica which was filled

with water and resting atop the channel with a calibration plate inside. On the plate was a grid of 0.12 mm diameter dots spaced at 0.5 mm intervals.

The microflow was seeded with fluorescent particles. To achieve microscale spatial resolution requirement, the particles were chosen small enough to follow the flow faithfully without (1) disrupting the flow field, (2) clogging the microdevice, and (3) producing unnecessarily large images [137]. At the same time, the particles must be chosen large enough so that they scatter sufficient light to be recorded and sufficiently dampen out Brownian motion. For the Lavision micro-PIV system, the particle size is required as 2-4 pixel with an particle density about 0.05ppp (particles per pixel). In the current experiment, Fluoro-Max red fluorescent polymer microspheres (Thermo Fisher Scientific Inc.) with a particle diameter of 0.86μm were used to seed the microflow.

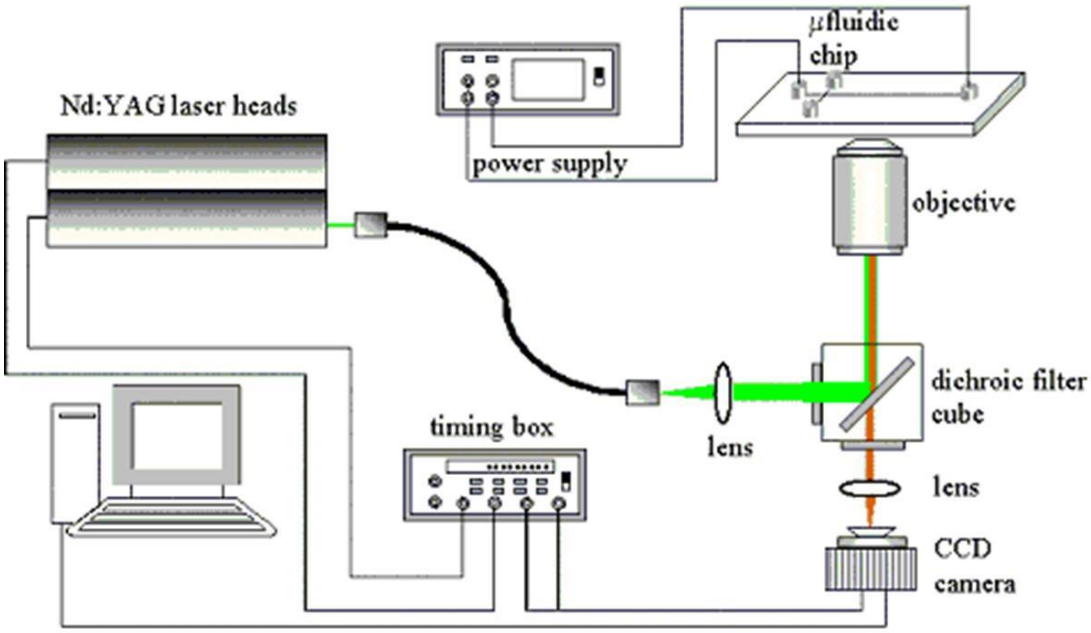

Figure 3- 3 A schematic Micro-PIV system of experimental setup

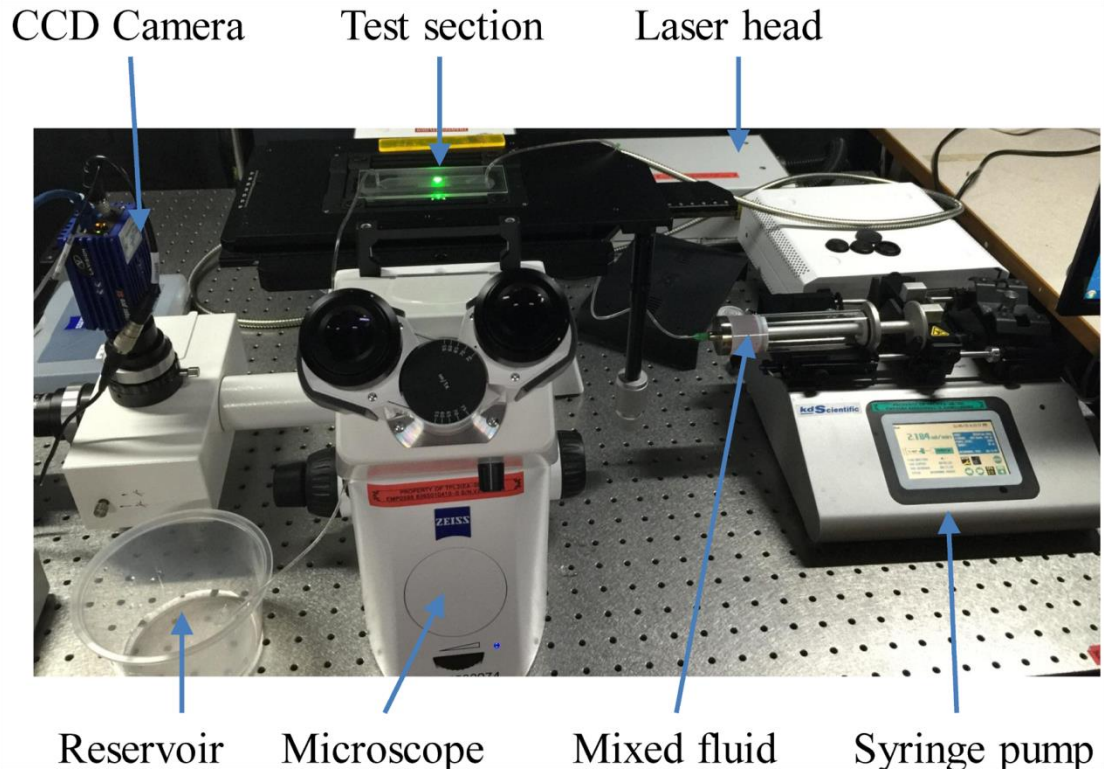

Figure 3- 4 Photograph of experimental set up

A photograph of experimental set up is shown in Figure 3- 4. The flow loop consists of a syringe pump (Model: LEGATO 270), test section and a

reservoir.

3.2.2. Test Section

The test section, shown in Figure 3- 5(a), consists of a transparent substrate and a transparent film. The channels were fabricated using PMMA substrate through milling to fulfill the transparent requirement of the micro-PIV system. Both the inlet manifold and outlet manifold were designed large enough to eliminate the influence of plastic tubes. The detailed dimensions are identical with those shown in Table 3-1.

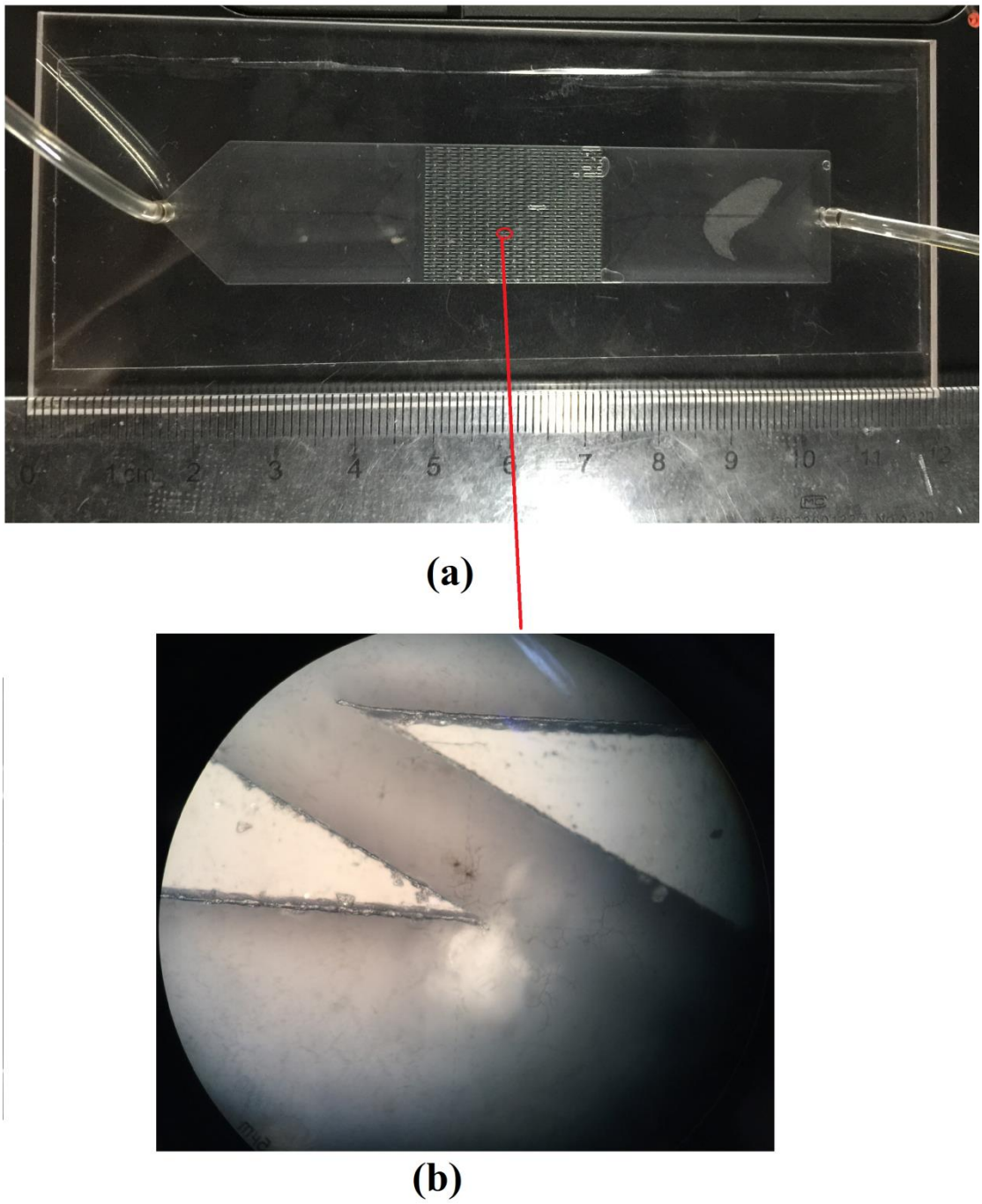

Figure 3- 5 (a) Photograph of test section; (b) Detail image of channels

3.2.3. Experimental Procedure

In order to obtain accurate data, the camera was calibrated before imaging. This process used a miniature channel replica which was filled with water and resting atop the channel with a calibration plate inside. On the plate was a grid

of 0.12 mm diameter dots spaced at 0.5 mm intervals.

After the test section was assembled and calibrations were completed, the pure water in the syringe was replaced with water mixed with fluorescent polymer microspheres. The syringe pump was switch on and the desired flow rate within the flow loop was set. When the flow was stabilized, the power of the laser was turned on. Flow within the interrogation region was recorded using 35 images. Then the interrogation region was changed and the recording repeated. Experiments were conducted at flow rate of 1.165 ml/min and 0.567ml/min for the two test sections respectively. The low mass flow rate is due to the microscale of the channels and to prevent the transparent film from bulging.

3.2.4. Uncertainty Analysis

In order to estimate the uncertainties caused by the PIV measurement system, several essential factors need to be taken into consideration, such as image distortion caused by the lens and the CCD sensor chip, inorthogonality of optical axes, laser light sheet thickness, traceability of tracer particles, and three-dimensional behavior in a fluid[138]. In the present study, the uncertainties of PIV measurements were evaluated by the sum-square of the precision index and the bias limit by elemental errors as the same method used by Iwaki et al. [139].

According to the principle of PIV measurement, the velocity, u, is expressed as follows:

$$u = \frac{1}{M} \times \frac{\Delta x}{\Delta t} \tag{3-5}$$

where Δt is the time interval of two captured images, Δx is the number of pixels corresponding to the displacement of particles in the images, M is the local magnification factor. Then, in order to evaluate the uncertainties of the obtained velocity, each uncertainty which propagate to the independent variables, M, Δx and Δt, need to be taken into consideration. The precision error, B, and bias error, S, of the variables based on each element error source were estimated separately by their integration, Thus, the total error, E, was obtained as follows:

$$E = \sqrt{(2 \times B)^2 + S^2} \tag{3-6}$$

Forliti et al.[140] found that, for a 128x128 domain using Gaussian fit, the bias error, S is 0.03pixel and the precision error, B, is 0.03pixel. Consequently, the total uncertainty resulting from this measurement method was estimated to be 6.7% for 95% confidence interval.

3.3. Results and Discussion

In this section, detailed analysis of velocity profile from both simulation and experiment are presented for the novel oblique fin microchannels. The

pressure drop characteristics are also discussed in this section.

3.3.1. Validation and Velocity Profile

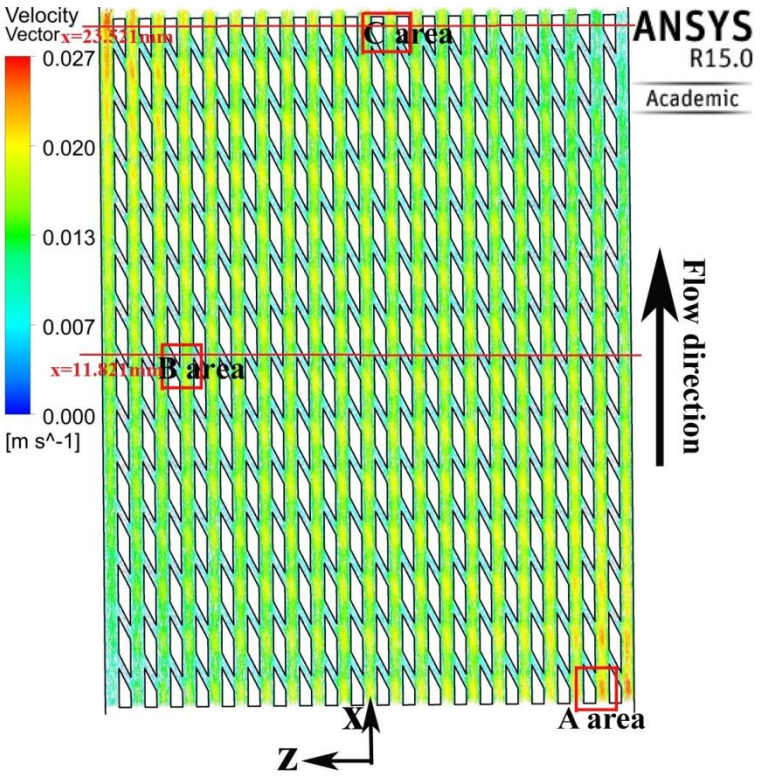

(a)

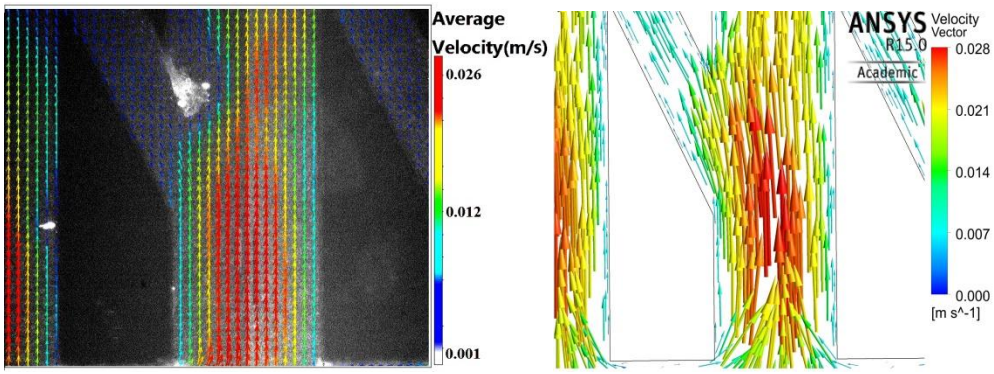

(b1) **(b2)**

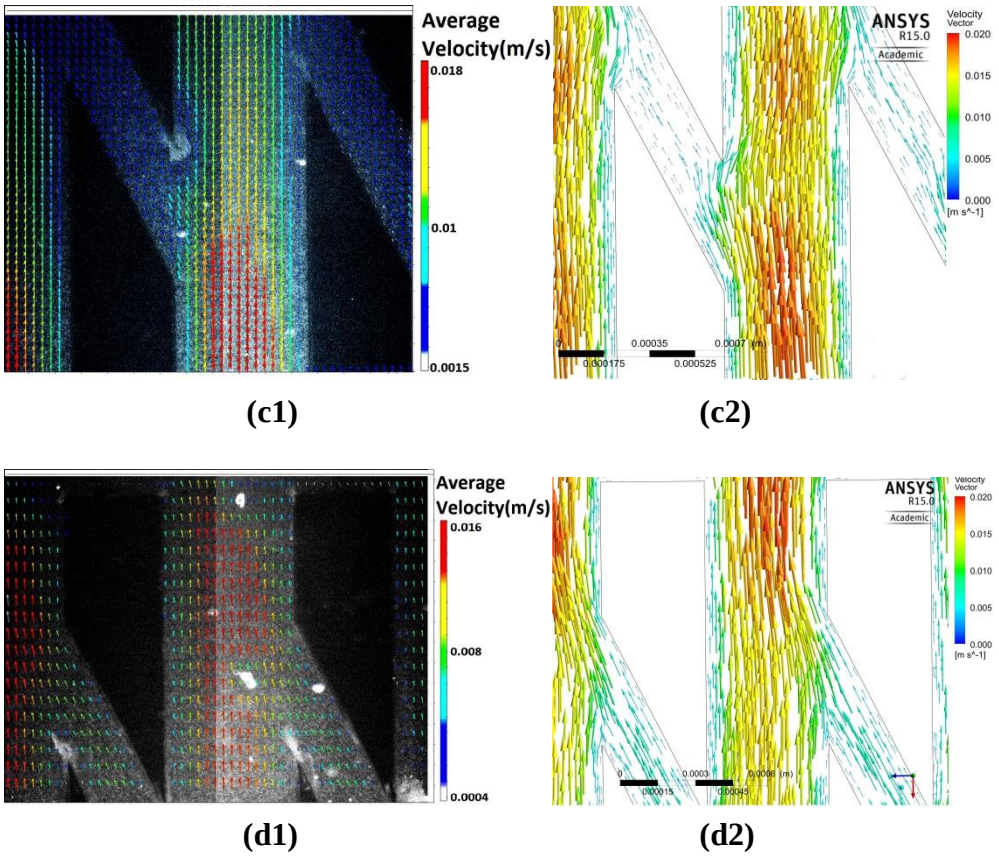

Figure 3-6 Velocity profile for oblique fin microchannel geometry Case 1 of (a) full fin region from simulation (the coordinate here is just for showing direction); (b1) A area from experiment; (b2) A area from simulation; (c1) B area from experiment; (c2) B area from simulation; (d1) C area from experiment; (d2) C area from simulation;

The full domain simulation results of geometry Case 1 reveal a noteworthy difference in velocity distribution across the whole fin region. Figure 3-6(a) shows the velocity profile for Case 1 at mid-depth of the whole fin region. At the inlet of the oblique fin region where x is quite near 0, significantly higher velocity is observed in the main channels near the right sidewall (negative *z*), while the velocity in the main channels near the left sidewall (positive *z*) is relatively lower than the velocity in a majority of main channels . As the fluid flows downstream, the velocity in the main channels near the right sidewall

progressively decreases. Conversely, the velocity in the main channels near the left sidewall increases continuously. Consequently, the velocity distribution at the outlet of oblique fin region presents an opposite tendency. Higher velocities appear in main channels near the left sidewall (positive *z*) and lower velocities appear in the main channels neat the right sidewall (negative *z*). This flow migration could be attributed to the continuous secondary flows generated in the oblique channels in the same direction. In order to maintain a uniform pressure drop between the inlet surface and outlet surface with the flow migration occurring within the fin array, the flow is re-distributed in the inlet manifold. Despite the velocity variation in the near wall regions, no obvious influence of the flow migration is observed in middle region.

Local velocity profiles of three different areas obtained from the experiment and simulation are also presented in Figure 3-6 (b), (c) and (d). Similar velocity distributions in main channels and secondary channels are presented in the vectors obtained from the micro-PIV system and CFD simulations, which indicates that the model used for the CFD simulations is sound for the oblique fin microchannel geometries and the results are credible. As shown from the velocity profiles, the momentum boundary layer development is disrupted at the trailing edge of each oblique fin and reinitialized at the leading edge of the next downstream fin. Meanwhile, fluid mixing continuously takes place as fluid in the adjacent main channels is connected by oblique secondary

channels. Both phenomena could contribute to enhanced heat transfer in oblique fin microchannel heat sink.

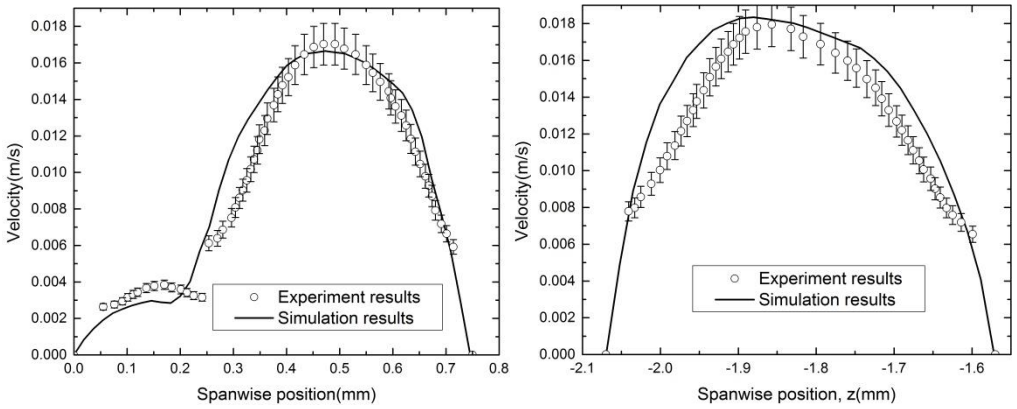

(a) **(b)**

Figure 3-7 Comparison of velocity magnitude from experiment and simulation for oblique fin geometry Case 1 along lines at (a) *x*=11.821mm in B area and (b) *x*= 23.521mm in C area

Further comparisons of velocities from experiment and simulation of oblique fin microchannel geometry Case 1 are shown in Figure 3-7. It can be seen that the results are quantitatively quite consistent. The velocity distribution is not parabolic but slightly skewed due to the impact of secondary flows. The fluctuation in the area $z<0.2$ shown in Figure 3-7(a) is due to the fact that the flow enters secondary channel, which is accurately captured by both the microPIV system and CFD simulation.

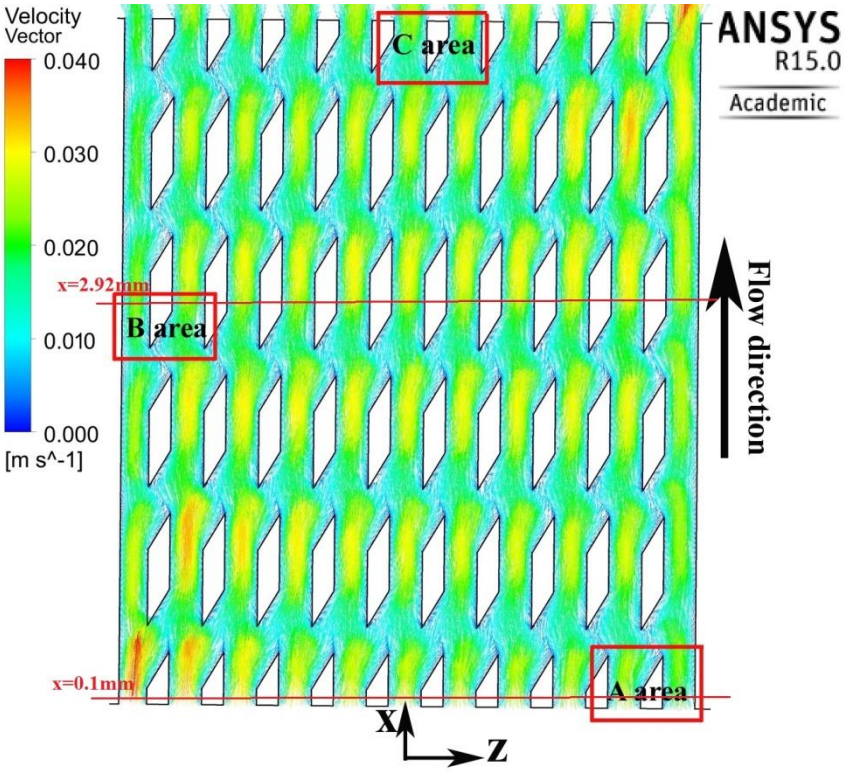
Velocity
Vector
0.040
0.030
0.020
0.010
0.000
[m s^-1]
C area
B area
A area
x=2.92mm
x=0.1mm
Flow direction
ANSYS
R15.0
Academic
X
Z

(a)

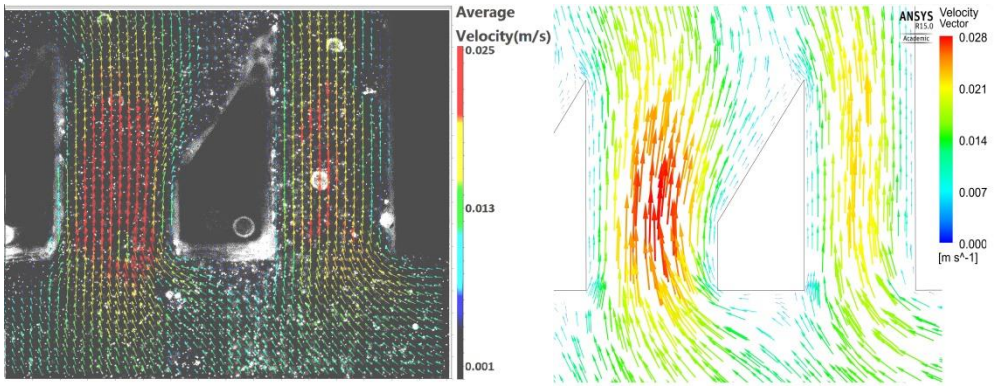
Average
Velocity(m/s)
0.025
0.013
0.001
Velocity
Vector
0.028
0.021
0.014
0.007
0.000
[m s^-1]

(b1) **(b2)**

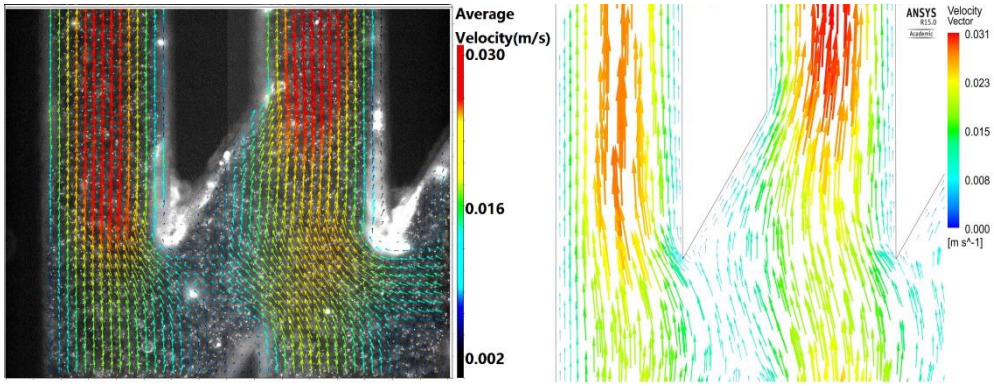
Average
Velocity(m/s)
0.030
0.016
0.002
Velocity
Vector
0.031
0.023
0.015
0.008
0.000
[m s^-1]

(c1) **(c2)**

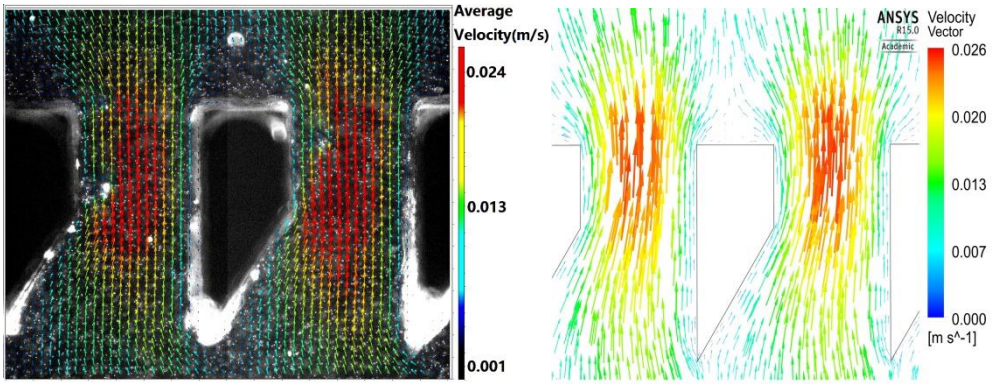

(d1) **(d2)**

Figure 3-8 Velocity profile for oblique fin microchannel geometry Case 2 of (a) full fin region from simulation (the coordinate here is just for showing direction); (b1) A area from experiment; (b2) A area from simulation; (c1) B area from experiment; (c2) B area from simulation; (d1) C area from experiment; (d2) C area from simulation;

The full domain simulation results of geometry Case 2 reveal a quite different velocity profile at mid-depth of the whole fin region from that of Case 1. From Figure 3-8(a), the velocity profiles in main channels for Case 2 are observed severely skewed towards the oblique secondary channels at each joint point. Although larger average velocity is imposed to the domain of Case 2, the velocity variation across the fin region is not severer than that of Case 1.

Local velocity profiles of three different areas obtained from the experiment and simulation are also presented in Figure 3-8(b), (c) and (d). Similar velocity distributions in main channels and secondary channels are presented in the vectors obtained from the micro-PIV system and CFD simulations, which further indicates the reliability of the CFD model. The disruption and reinitialization of momentum boundary layers are also observed in the vectors from both microPIV system and CFD simulations. An interesting phenomenon

is that the fluid in adjacent main channels entering the oblique secondary channels experiences an expansion process and then flows back to its original rows, without showing notable mixing through the oblique secondary channels. This phenomenon is due to the combined effects of small fin length to fin pitch ratio, small fin width to main channel width ratio and large oblique angle. According to the study of Fan et al.[107], the increase of oblique angle will decrease the secondary flow percentage after the angle exceeding a certain value.

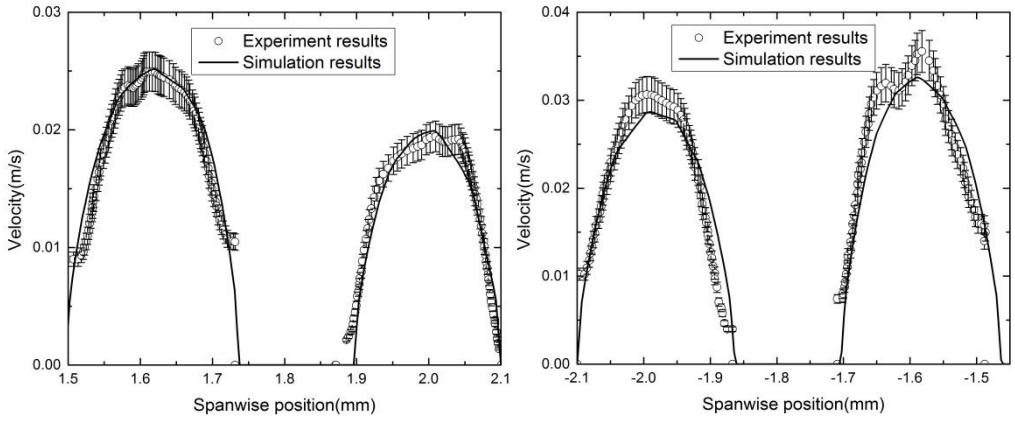

(a) **(b)**

Figure 3-9 Comparison of velocity magnitude from experiment and simulation for oblique fin geometry Case 2 along lines at (a) *x*=0.1mm in A area and (b) *x*= 2.92mm in B area

Further comparisons of velocity magnitude for experiment and simulation of oblique fin microchannel geometry Case 2 are shown in Figure 3-9. Good quantitative agreement is observed for both positions. The velocity distribution at observation positions away from the joint points presents a parabolic trend, which indicates a negligible influence of oblique secondary channels.

3.3.2. Pressure Drop Characteristics

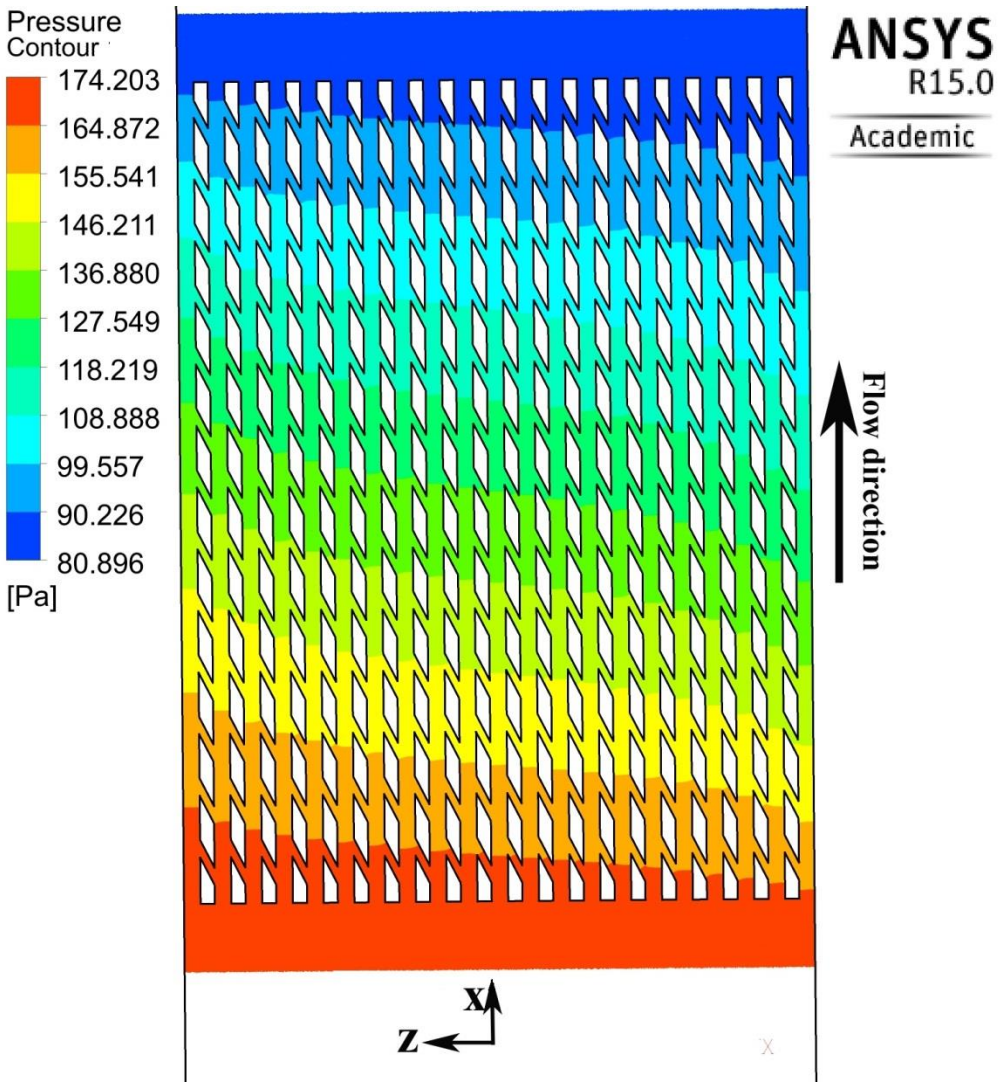

Figure 3-10 Pressure contour for oblique fin microchannel geometry Case 1 of full fin region from simulation (the coordinate here is just for showing direction)

The pressure contour for the oblique fin microchannel geometry Case 1 also presents a variation in the spanwise (z) direction corresponding to the diverse velocity distribution in main channels. In the upstream (small x region), fluid in main channels near the right sidewall (negative z) undergoes sharper pressure drop compared to that in the main channels near the left sidewall (positive z) due to the larger mass velocity. As the velocity decreases in main

channels near the right sidewall (negative *z*), the pressure drop also decreases, while the opposite is also true for the fluid in main channels near the left sidewall (positive *z*). Such a phenomenon could prevent a large difference of total pressure drop for fluid through channels near different sidewall.

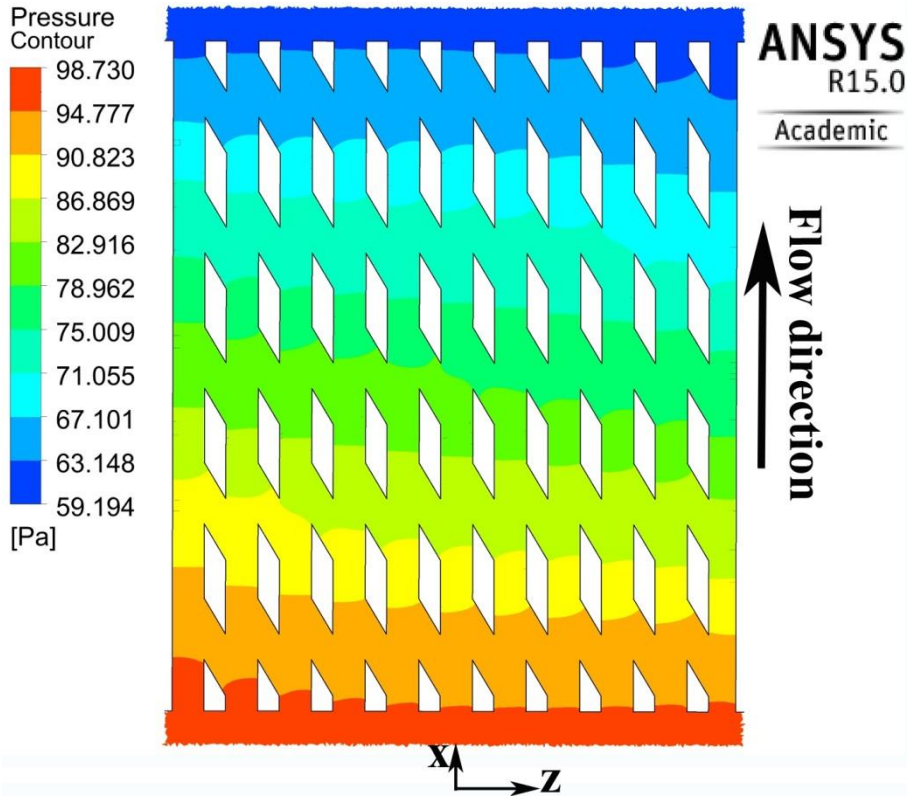

Figure 3-11 Pressure contour for oblique fin microchannel geometry Case 2 of full fin region from simulation (the coordinate here is just for showing direction)

Compared to the obvious variation in pressure distribution of geometry Case 1, the pressure change along spanwise (*z*) direction for Case 2 is not continuous. The isobars are relatively flat in the upstream (small *x* region) and downstream (large *x* region) except for two corners.

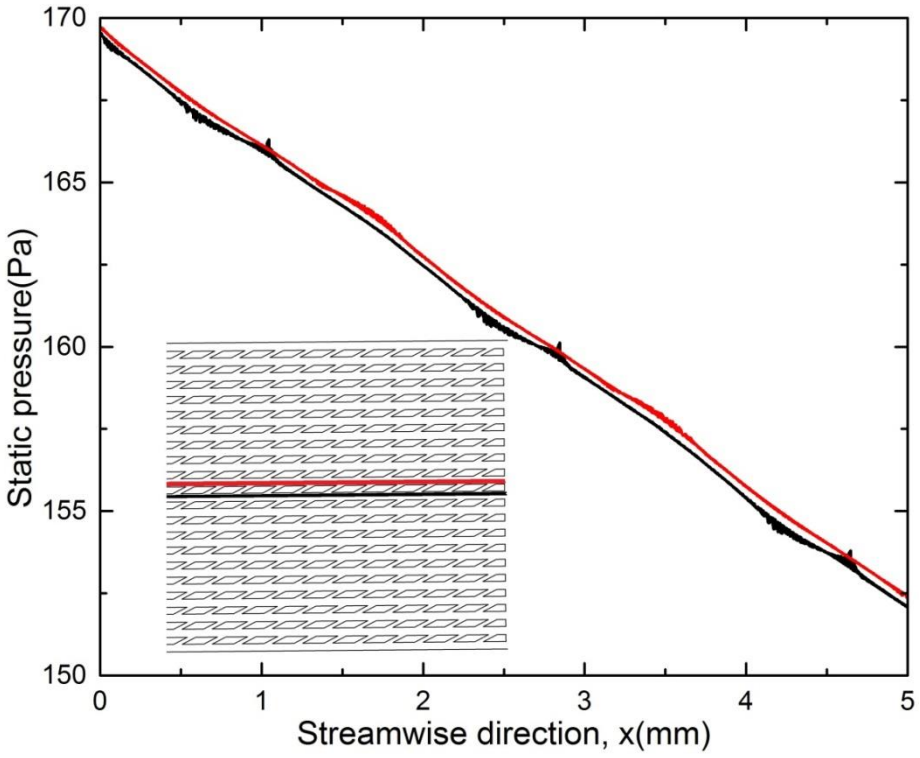

(a)

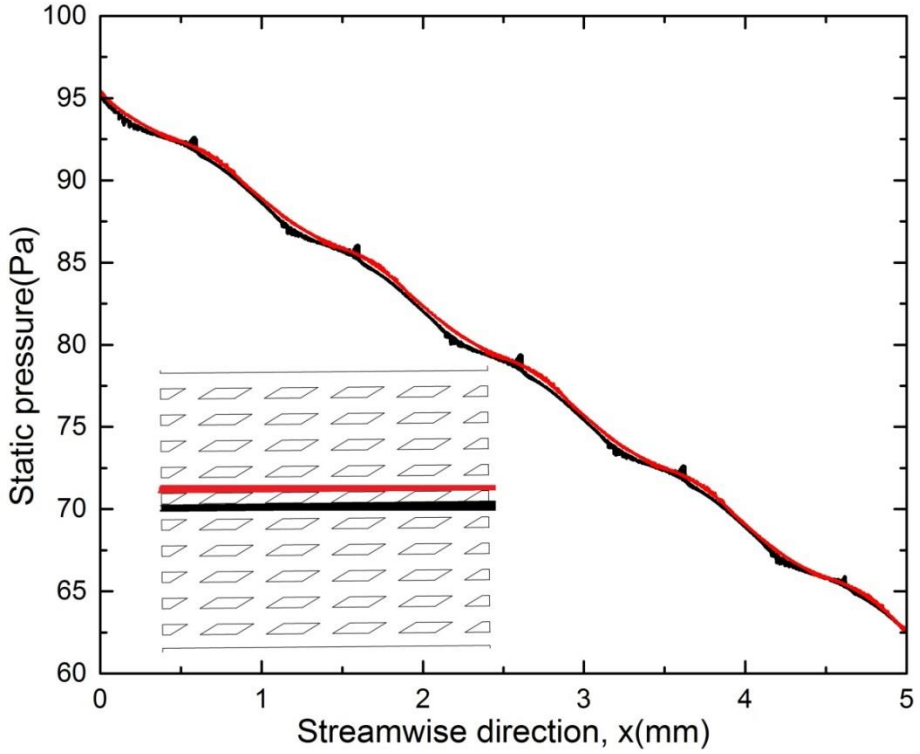

(b)

Figure 3-12 Local pressure profile comparisons between two rows of adjacent half main channels for (a) oblique fin microchannel geometry Case 1 and (b) oblique fin microchannel geometry Case 2

Figure 3-12 depicts the local pressure profile comparisons between the labeled areas (half of main channels located at Z=0mm and its adjacent half main channels). Due to the periodic fluid convergence and divergence from the oblique secondary channels, the pressure change in main channels experiences "periodic dips and spikes". From the local pressure profile of Case 1, the "dips and spikes" turn up at staggered positions and each phenomenon exists in the different half rows respectively due to the fact that fluid in the half channels with black label only experiences divergence and fluid in the half channels with red label only experiences convergence. In contrast, the "dips and spikes" turn up at collocated positions and exist in both rows for the Case 2. This phenomenon is quite consistent with the vectors shown in Figure 3-8. Fluid from the main channels enters the oblique secondary channels experiencing expansion and turns back rather than flows through the secondary channels, thus the "dips" alternate with "spikes" along the streamwise direction in the same half channels.

3.4. Conclusions

Velocity profiles for two different novel oblique fin microchannel geometries were experimentally and numerically investigated. The pressure drop characteristics for each geometry were also discussed. The following key finding can be drawn from the present study:

- The CFD model used in the present study is valid and reliable for the novel oblique fin microchannel geometry. The velocity vectors for both geometries obtained from the CFD simulations are highly coincident with the experiment results. The disruption and reinitialization of momentum boundary layer development in the main channels are also observed by both the microPIV system and the CFD simulation.

- The generation of secondary flow is highly dependent on the structural design even if small channels at a certain angle between two main liquid channels are added. Flow will not follow the oblique channel direction when oblique fin microchannel geometry is designed with a small fin length to fin pitch ratio, small fin width to main channel width ratio and large oblique angle (e.g. the values are 0.54, 0.67 and 30.8 respectively for the Case 2) .

- The continuous secondary flow in the same oblique direction leads to an obvious velocity and pressure variation in the spanwise direction in fin region. The flow is re-distributed in the inlet manifold and flow migration occurs within the fin array.

- In a majority of the oblique fin region, flow migration does not affect the local coolant velocity significantly. The velocity distribution in most main channels shows no observable difference from each other except for that

in the main channels lying near the sidewalls.

CHAPTER 4 REDUCED EQUIVALENT CIRCUIT FLUID FLOW MODEL

In this chapter, a reduced equivalent circuit fluid flow model is developed to rigorously and accurately predict the flow distribution in planar secondary flow generating oblique fin configurations. The highly *nonlinear* relationship between pressure drop and mass flow rate is modeled via resistive electrical circuits with nonlinear current (flow rate)-dependent resistances. Detailed numerical simulations are employed to fit parameters in correlations for the hydraulic resistances of main and secondary channels, and also for subsequent model validation. Detailed comparisons between the results of reduced model and numerical simulation are presented.

4.1. Introduction

As stated in Chapter 3, secondary flow generation and flow migration occurs continuously as the coolant travels downstream, thus leading to flow maldistribution in the planar oblique fin microchannel geometry. The phenomenon is common for a group of geometries that will purposely create second flow to enhance the heat transfer. When such a heat sink is used to cool an electrical component, the non-uniform temperature distribution might cause uneven thermal expansion of the device and could damage its electrical performance [8]. Thus, full domain simulations are needed when conducting

numerical studies on such geometries to capture the flow maldistribution effects.

However, full domain simulations are more cumbersome to set up and can be computationally expensive, which limit their use in practical engineering applications. As such, it is highly desirable to develop reduced models that are easy to use while at the same time reasonably accurate.

4.2. Theoretical Approach

The analogy between electrical and mechanical (including fluidic) systems has been widely used since the early of last century [109]. The well-known Hagen-Poiseuille law can be used to obtain an expression for the pressure drop Δp in terms of the flow rate Q:

$$\Delta p = R_{hyd} Q \tag{4-1}$$

where the proportionality factor R_{hyd} is the hydraulic resistance. The Hagen-Poiseuille Law is completely analogous to Ohm's law given by:

$$\Delta V = RI \tag{4-2}$$

which relates the electrical current I through a wire with the electrical resistance R of the wire and the electrical potential drop ΔV across the wire. Given the analogy between the Hagen-Poiseuille Law and Ohm's Law, it is quite appropriate to apply well-established methods from electric circuit

theory to microchannel flow ('microfluidic') networks. Utilizing this electrical analogy, it is possible to draw the equivalent electric circuit for a given microfluidic network. Channels with hydraulic resistances R_{hyd} become resistors, flow rates Q become currents, and pumps providing the pressure differences Δp become voltage sources (or current sources).

The electrical-hydraulic analogy is adopted here to simulate the complex flow in planar secondary flow generating oblique fin arrays. The basic scheme for this reduced equivalent circuit fluid flow model is shown in Figure 4-1. The circuit was built in Simulink, which is a graphical extension to MATLAB (Mathworks Inc., USA) for modeling and simulation of systems. With particular series/parallel coupling of resistors, the equivalent circuit is able to capture the flow characteristics of the complex flow in an oblique-finned geometry. In the oblique-finned configuration, small channels are added at a certain angle between two main liquid channels where the resultant pressure gradient drives the secondary flow from one main channel to the other. This characteristic is also captured by the equivalent circuit where the two terminals of the equivalent resistors for secondary channels are connected staggered, hence the resultant potential difference drives current through these resistors.

The determination of the hydraulic resistance plays a crucial role in the setup

of the equivalent circuit model. The friction factor as due to hydraulic developing flow (results of Curr et al.[141]) in microchannels is first considered. Meanwhile, based on the study in Chapter 3, we realize that the flow distribution in an oblique unit is the combined result of hydraulic characteristics of both main channels and secondary channels. The hydraulic resistance of each type of channel is therefore critically important for the reduced equivalent circuit fluid flow model. Thus, the present work develops rigorous methods to calculate hydraulic resistances in different parts of the oblique-finned geometry to improve the accuracy of the reduced model.

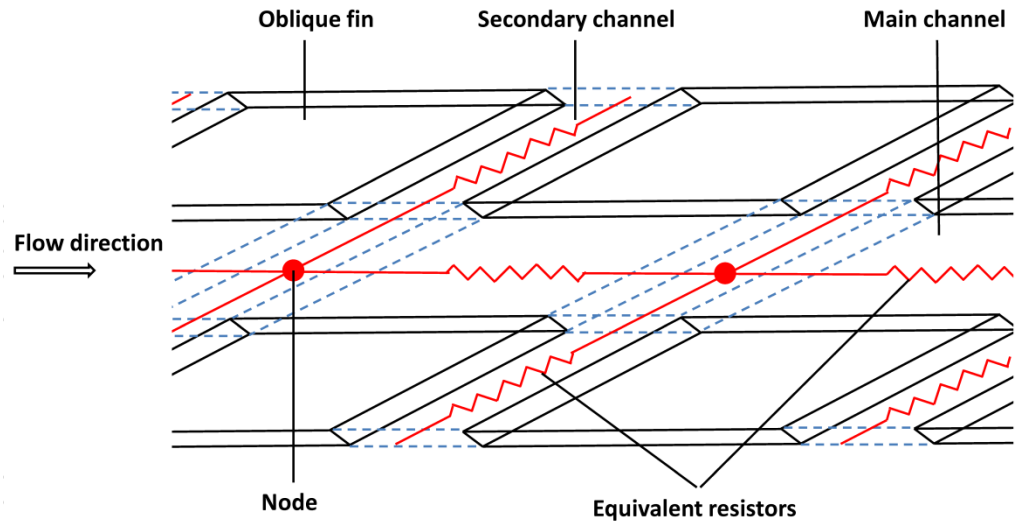

Figure 4-1 Schematic of flow paths of oblique-finned system and its reduced circuit

4.3. Design of Experiments

As mentioned above, and also detailed in Section 4.4 below, fluid flow patterns in the main and secondary channels within the oblique fin

configuration can differ greatly from 'classical' developing (or fully developed) flow in microchannels. Hence, in Section 4.4, we outline the development of new hydraulic resistance correlations for both primary and secondary channels. These new correlations are obtained by regression analysis on a sufficiently large database collected based on the Design of Experiments (DOE) methodology applied to reduced domain numerical (CFD) simulations detailed in Section 4.4. One of most important steps in DOE is to determine the factors that contribute to the response variable. In this study, the response variable is taken to be f Re. As the smallest domain of study is an oblique unit; a dimensional analysis is conducted, as outlined below, for an oblique unit to determine the factors that influence the response $(f \text{ Re})_{\text{unit}}$ to ensure that the test cases satisfy the basic principles of experimental design and fully account for the flow characteristics of oblique configurations.

4.3.1. Dimensional Analysis

In Fan et al. [107]'s parametric study on the oblique fin geometry, which assumed infinite fin height and fixed fin width and main channel width, a similarity analysis conducted by applying external forced convection theory to the oblique-finned configuration identified four dimensionless parameters (θ, w_{ob}/l_u, D_h/l_u, Re_{unit}) as having a significant influence on the average overall friction factor for an oblique fin unit. Here, hydraulic diameter is defined on a unit-base as:

$$D_h = \frac{4\times \textit{flow volume}}{\textit{heat transfer area}} = \frac{4\times H\times\left(l_u\times\left(w_w+w_{ch}\right)-l\times w_w\right)}{\left(l_u\times\left(w_w+w_{ch}\right)-l\times w_w\right)+2\times H\times\left(l+w_w/\sin\theta\right)} \tag{4-3}$$

Now, studies on both fully developed and developing laminar flow in ducts by Curr et al.[141], Shah and London [142] and Kakaç et al.[143] underscore that the aspect ratio is a key parameter in determining the friction factor for a rectangular channel. Therefore, H/w_{ch} (aspect ratio of main channel) and $H/(w_{ch}+w_w)$ (aspect ratio of oblique unit) should also be involved in the dimensionless groups that dictate the friction factor of an oblique unit. Through removing duplicate items, the final dimensionless parameters group for the oblique unit may be determined as (θ, H/w_{ch}, w_{ob}/l_u, $D_h/(w_{ch}+w_w)$, Re_{unit}).

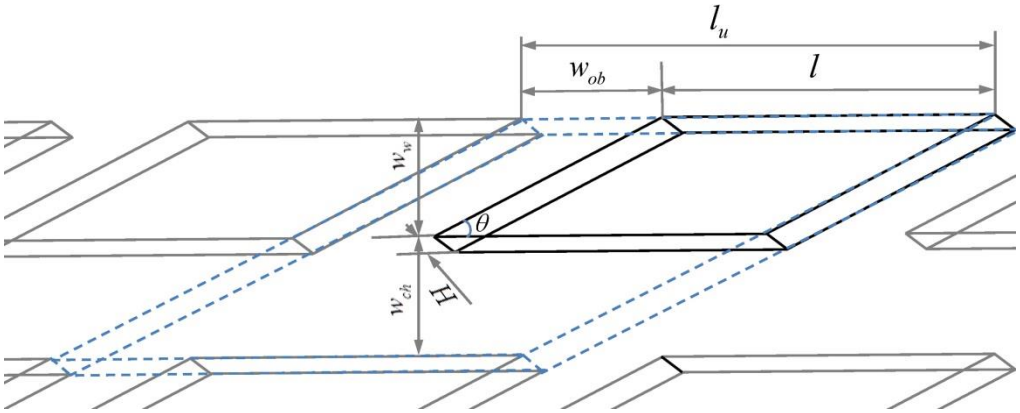

Figure 4-2 Schematic of oblique unit

4.3.2. Numerical Test Cases

Numerical 3D simulations were employed to generate the database required for the regression analysis to obtain new correlations for hydraulic resistances in the different elements of the oblique fin arrays. As identified by the

dimensional analysis of oblique unit in 4.3.1 above, dimensionless parameters (θ, H/w_{ch}, w_{ob}/l_u, $D_h/(w_{ch}+w_w)$, Re_{unit}).are chosen as influencing factors in DOE. The levels for each factor are listed in Table 4-1. As a well-known parametric study tool, Taguchi method [144] is used for the experimental design and 64 simulation cases are finally determined using an 8^5 orthogonal array.

Table 4-1 Factors and levels in design of experiment (DOE)

factors	Levels							
	1	2	3	4	5	6	7	8
Re	30	160	290	420	550	680	810	940
H/w_{ch}	0.3	0.8	1.3	1.8	2.3	2.8	3.3	3.8
w_{ob}/l_u	0.1	0.2	0.3	0.4	0.5	0.6	0.7	0.8
$D_h/(w_{ch}+w_w)$	0.2	0.3	0.4	0.5	0.6	0.7	0.8	0.9
θ (in degree)	20	23	26	29	32	35	38	41

4.4. Methodology

Two different methodologies will be introduced in details in this section. First, we describe numerical simulations using computational fluid dynamics (CFD). Next we describe the development of our equivalent circuit model, involving the analysis of flow patterns in oblique configurations and development of

new correlations for hydraulic resistances.

4.4.1. Numerical Simulation Methodology

3D numerical simulations on the forced convective flow through the oblique fin array were carried out using ANSYS R15.0 to (1) understand the uniqueness of flow pattern in oblique fin configurations and key differences between primary and secondary flow, (2) obtain the required database for DOE to develop correlations for friction factor and (3) serve as a benchmark for the reduced equivalent circuit fluid flow model. The oblique fin array exhibits a spanwise periodic pattern as seen from the 3D plan view in Figure 4-3(a) if the edge effect is neglected. Hence, in order to reduce the computation domain for all the 64 cases designed using Taguchi method in section 3, the periodic boundary condition consisting of a full width fin at the center and half width channels on each side as shown in Figure 4-3(b) was used. Based on the stated assumptions and model descriptions, the 3D double precision pressure based solver was selected with the standard SIMPLE algorithm as its pressure-velocity coupling method. Standard discretization scheme was used for the pressure equation while second order upwind discretization scheme was selected for the momentum equation. With regards to the material selection, water was selected for working fluid. The continuity equation and the Navier-Stokes equations in the steady, incompressible form which are described in Chapter 3, along with the associated boundary

conditions were solved using the general-purpose finite volume based CFD software package. Since the Navier-Stokes equations were solved inside the domain, no-slip boundary condition was applied on the channel walls for all cases. A prescribed velocity was applied at the inlet and gauge pressure at the outlet was set as 0 Pascal. A residual value of 1×10^{-6} was set as the convergence criteria for the continuity equation, x-velocity, y-velocity and z-velocity.

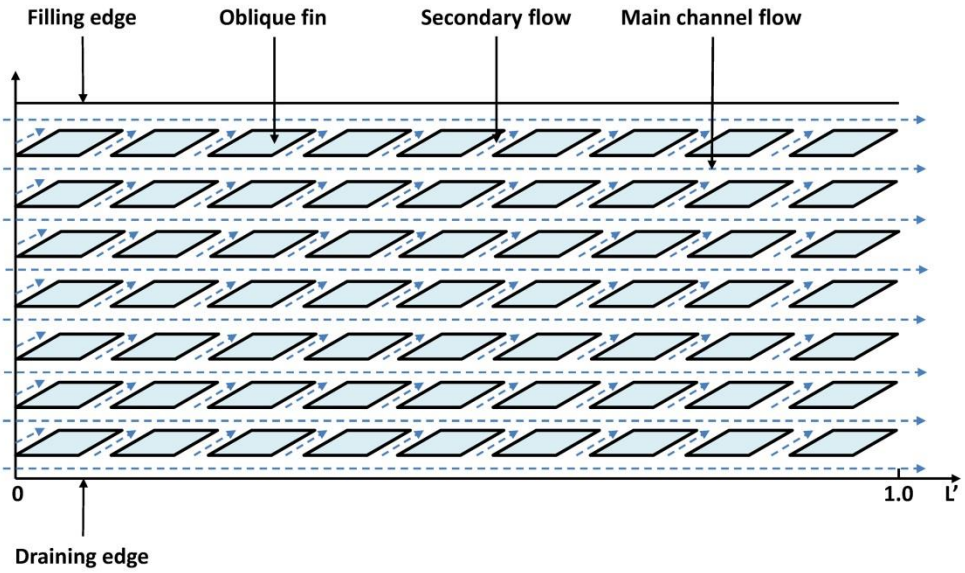

(a)

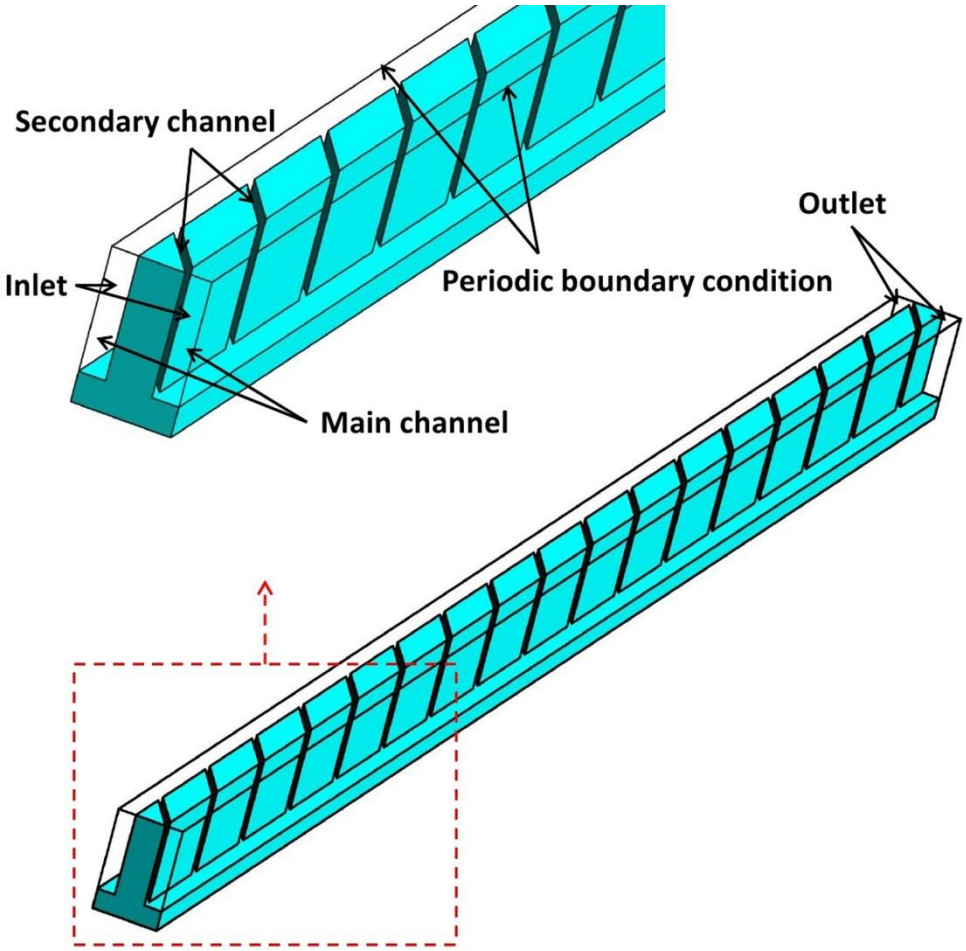

(b)

Figure 4-3 (a) Plan view of microchannel heat sink using oblique configurations (b) Computation reduced domain for oblique configurations

The grid size used in the numerical simulations in Chapter 3 was applied to the 64 simulation cases determined by Taguchi method. A total of 2,484,396 elements were finally selected for the fluid domain in order to preserve both accuracy and cost after the study of grid independence.

Full-domain geometry-based 3D simulations were also performed to serve as a benchmark for the equivalent circuit model. A sample domain is shown in Figure 4-4 and dimensional details are shown in Table 4-2.

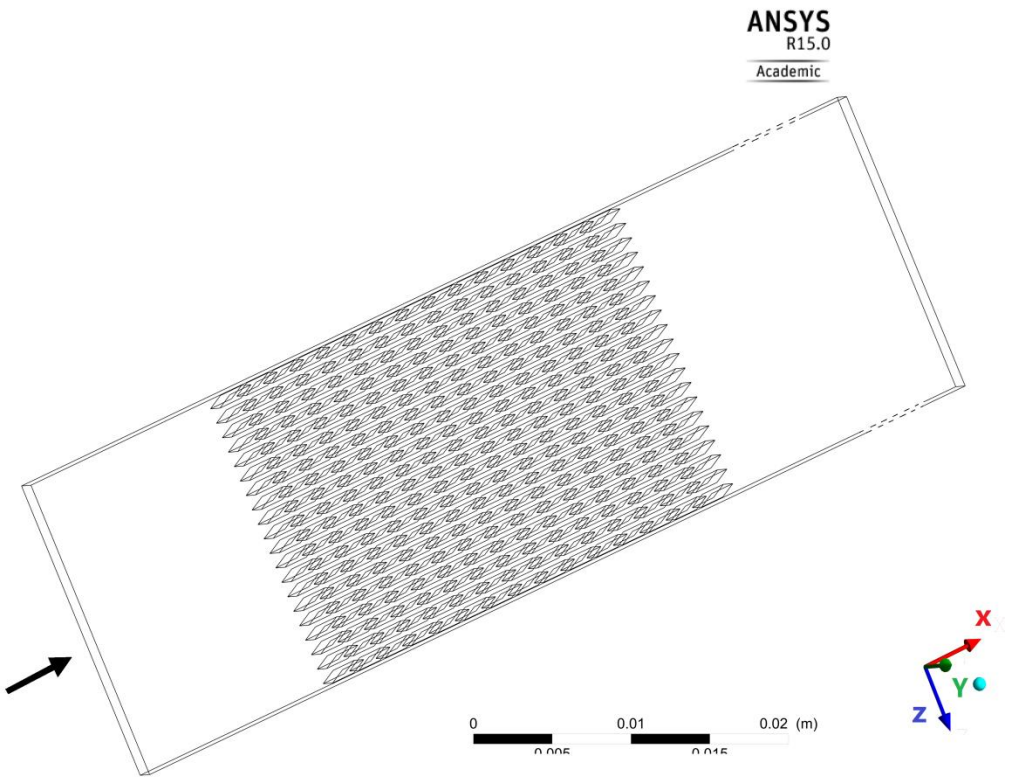

Figure 4-4 Full computation domain for oblique configurations

Table 4-2 Dimensional details for oblique configurations in full domain simulations

Case	w_{ch} (μm)	w_w (μm)	H (μm)	α	n	m	θ (deg)	l_u (μm)	l (μm)	u (m/s)
#1	500	500	525	1.05	12	16	27	2,000	1,500	0.05
#2	500	500	1,000	2	12	16	23	2,000	1,500	0.05
#3	500	500	1,500	3	20	15	27	2,000	1,600	0.03
#4	500	500	1,500	3	20	15	35	2,000	1,600	0.05
#5	500	500	1,000	2	30	15	27	2,000	1,400	0.05
#6	500	500	1,500	3	20	15	27	2,000	1,400	0.05
#7	400	350	1,000	2.5	40	20	27	1,500	1,125	0.05
#8	539	465	1,487	2.76	22	12	26.4	1,995	1,331	0.2
#9	500	500	1,500	3	20	15	27	2,000	1,600	0.25

4.4.2. Equivalent Circuit Fluid Flow Model

As stated in section 4.2, the equivalent circuit for a given microfluidic network is constructed based on the analogy between the Hagen-Poiseuille Law and Ohm's Law. Channels with hydraulic resistances R_{hyd} become resistors, flow rates Q become currents, and pumps providing the pressure differences Δp become voltage sources. It is therefore crucial to determine the relationship between pressure differences Δp and flow rates Q, that is, the expressions for hydraulic resistances R_{hyd}. The pressure drop due to friction in a channel of constant hydraulic diameter D_h over a length L is given by the expression:

$$\Delta p = \frac{2 f \rho u_m^2 L}{D_h} \tag{4-4}$$

Introducing Poiseuille number ($Po=fRe$), which depends on the flow channel geometry, into Eq. (4-4), the pressure drop can be expressed as:

$$\Delta p = \frac{2PoL\rho u_m^2}{\mathrm{Re}\, D_h} \tag{4-5}$$

which further yields

$$\Delta p = \frac{2PoL}{D_h^2}\mu u_m \tag{4-6}$$

Or

$$\Delta p = \frac{2PoL\mu}{D_h^2 \rho A_{eq}} Q \tag{4-7}$$

where Q is the mass flow rate through A_{eq}.

According to the Poiseuille's Law, in the case of smooth flow (laminar flow), the flow rate is given by the pressure difference divided by the viscous resistance. Hence combining Eq. (4-1) and (4-7), the flow resistance can then be obtained as:

$$R_{hyd} = \frac{2PoL\mu}{D_h^2 \rho A_{eq}} \tag{4-8}$$

In this expression, channel length l, hydraulic diameter D_h and cross area A_{eq} can be obtained or calculated directly from channel dimensions while viscosity μ and density ρ are fluid properties. Next, to move onwards and establish rigorous correlations for Poiseuille number ($Po=fRe$), results from the numerical simulation described in section 4.4.1 were first used to understand the uniqueness of flow pattern in oblique configurations and key differences between primary and secondary flow.

4.4.2.1. Main channel

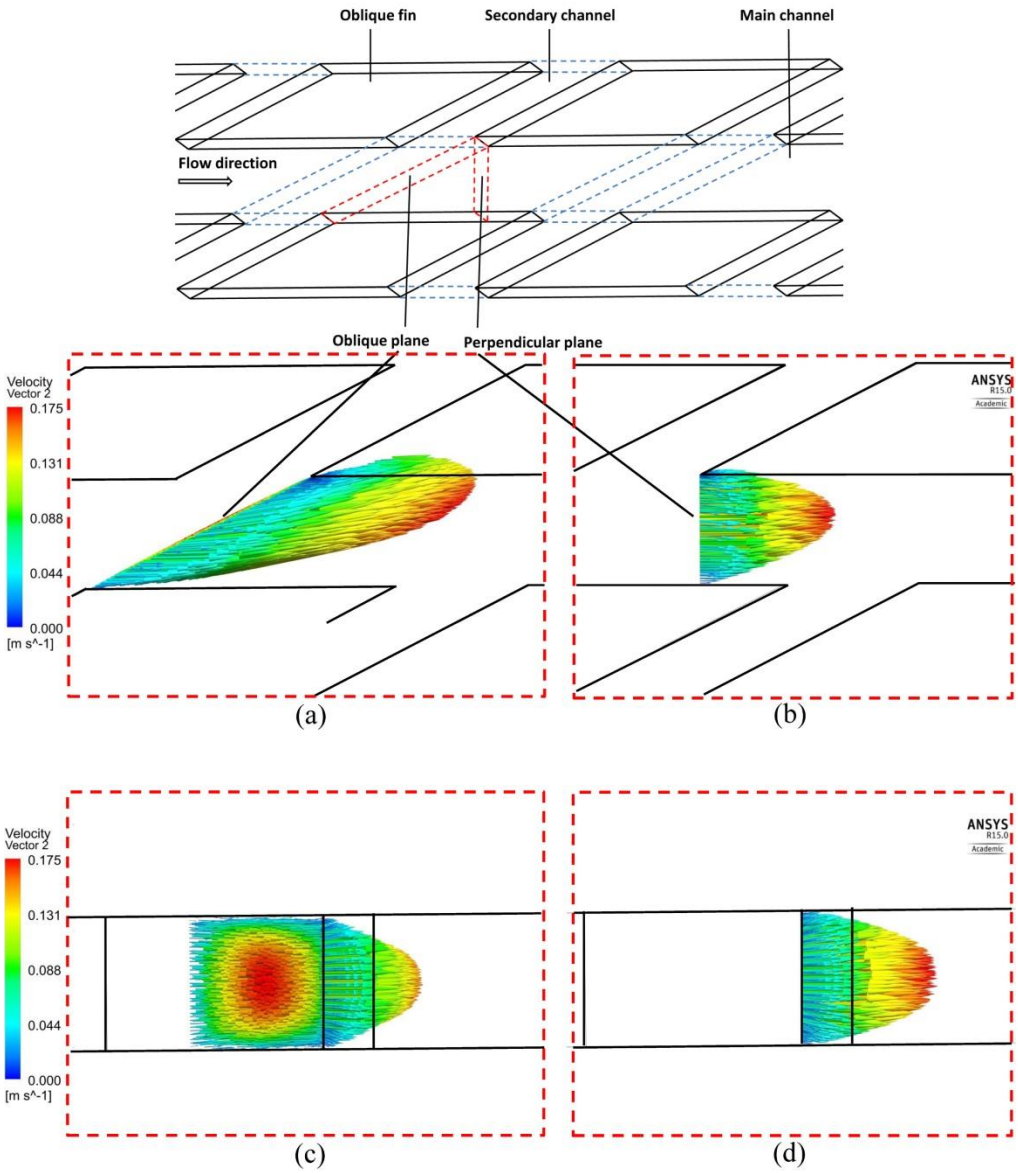

Figure 4-5 Velocity vector in main channel for Case 5 (a) along oblique direction on oblique inlet plane; (b) along perpendicular direction on perpendicular plane; (c) along fin height direction on oblique inlet plane; (d) along fin height direction on perpendicular plane

As shown in Figure 4-1, due to the unique oblique fin geometry, the main channel differs from a traditional rectangular duct. From the velocity vector plots shown in Figure 4-5, it can be seen that the velocity distribution along

the fin height follows a parabolic profile while being severely skewed along the oblique edges on the oblique inlet plane. The major difference between the velocity distributions along these two orthogonal directions due to the unique oblique geometry highlights that the calculation of friction factors for the main (primary) channel(s) in the oblique geometry will be more complicated than for the case of conventional rectangular ducts; the presence of secondary channels disrupts and reinitializes the boundary layer development at each oblique inlet plane of the main channels. Therefore the friction factors in the main channels can be calculated by invoking the developing flow assumption. Firstly, the dimensionless axial length in the flow direction for the main channel is defined as:

$$l^+ = \frac{l}{D_{hmain}\,\mathrm{Re}_{main}} \tag{4-9}$$

Now, due to the symmetry of flow in conventional rectangular ducts, aspect ratio is defined as the length ratio of the short side to the long side to guarantee that its value less than 1.0[141]. However, such a definition becomes inapplicable when the flow is not symmetric in the spanwise direction as a result of the presence of secondary flow. We therefore define a new characteristic parameter to replace the aspect ratio, which appropriately captures the unique flow characteristics in the oblique fin array main channel. Such a parameter should be always less than 1.0 in accordance with the aspect

ratio in conventional rectangular ducts, regardless of how the fin height and channel width changes. In keeping with the calculation method of Curr et al.[141], we define this new parameter as the ratio of perimeters of the perpendicular plane and oblique plane shown in Fig.5:

$$\alpha^* = \frac{P_{\text{perpendicular}}}{P_{oblique}} = \frac{w_{ch}+H}{\frac{w_{ch}}{\sin\theta}+H} \begin{cases} = \dfrac{\alpha+1}{\frac{\alpha}{\sin\theta}+1}, while & H > w_{ch} \\ = \dfrac{1+\alpha}{\frac{1}{\sin\theta}+\alpha}, while & H < w_{ch} \end{cases} \tag{4-10}$$

Finally, the factors of $(fRe)_{main}$ for developing flow in oblique main channels are calculated using information from the table provided in ANNEX A. The results of this method are compared with results from CFD simulation in Section 4.5, and agree well with the latter.

4.4.2.2. Secondary channel

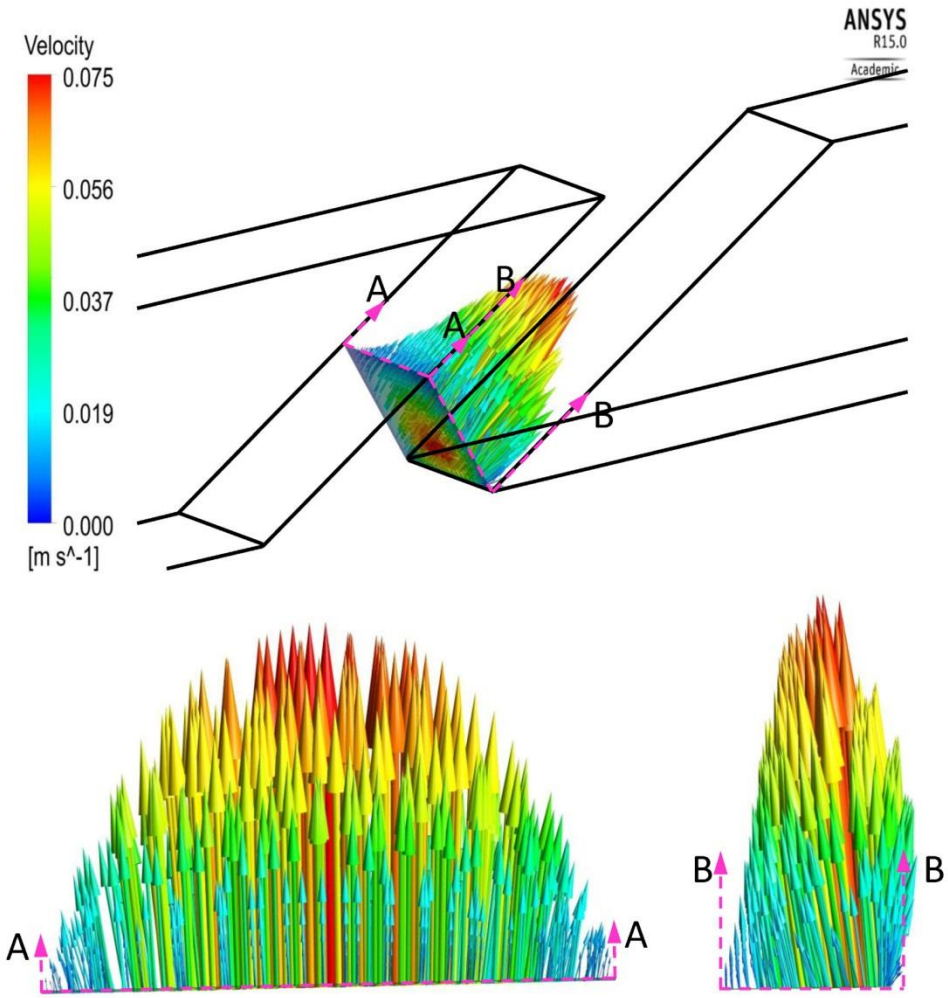

Figure 4-6 Velocity vectors of secondary channel flow for Case 5

The velocity vectors provided for a typical case in Figure 4-6 indicate that flow patterns in secondary channels reveal a much more complicated situation, that is, the maximum of velocity is not located at the centerline, but is skewed. Numerical simulations of flow patterns in secondary channels in [7, 107] also reveal the similar situation. However, the velocity vectors in Figure 4-6 indicate that the velocity distribution of secondary flow in the direction of fin height still follows a parabolic profile. Hence, the flow pattern in secondary

channel cannot be simply approximated as either a laminar internal flow or external flow, but may be considered a combination of both. Sahnoun et al.[145] studied friction factors for the louver fin geometry; in their analysis, the friction factor on the louvers was given by the flat Pohlhausen solution, which assumes that the flow on the louvers is a Falkner-Skan flow, and the predicted results showed good agreement with experimental results. Given the similarity of the louver fin geometry and oblique fin geometry, it is reasonable to consider the flow pattern in the secondary channel as the combination of internal flow and external flow, since certain parts of the flow is bounded one side only. Furthermore, due to the different flow behavior observed in main channels and secondary channels, different correlations have to be developed for the calculation of hydraulic resistances of the secondary channels, as discussed below

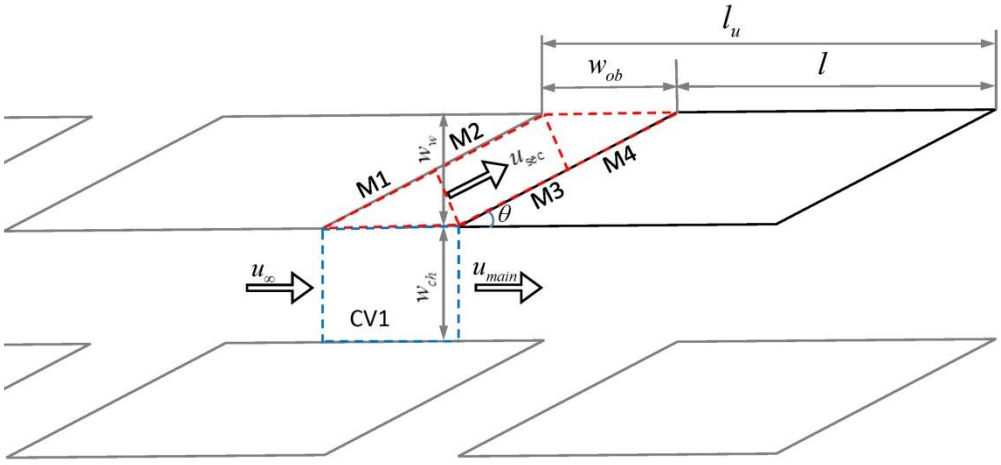

Figure 4-7 Plan view of oblique fin array

Considering both main channel and secondary channel have the same height,

the mass balance of control volume 1 (CV1) in Figure 4-7 can be expressed as:

$$\rho u_{\infty} w_{ch} = \rho u_{\sec} w_{ob} \sin\theta + \rho u_{main} w_{ch} \tag{4-3}$$

The above equation can be non-dimensionalised by defining the following dimensionless independent variables:

$$u_{\sec}^{+} = \frac{u_{\sec}}{u_{\infty}}, \quad u_{main}^{+} = \frac{u_{main}}{u_{\infty}}, \quad w_{ch}^{+} = \frac{w_{ch}}{l_u}, \quad w_{ob}^{+} = \frac{w_{ob}}{l_u} \tag{4-4}$$

Substituting these dimensionless independent variables in Eq.(4-4) into Eq.(4-3) and eliminating the constant fluid density (ρ), the mass balance of CV1 becomes:

$$w_{ch}^{+} = u_{\sec}^{+} w_{ob}^{+} \sin\theta + u_{main}^{+} w_{ch}^{+} \tag{4-5}$$

Hence, the dimensionless velocity in main channel and secondary channel will be a function of $w_{ch}{}^{+}$, $w_{ob}{}^{+}$ and θ.

$$u_{\sec}^{+}, u_{main}^{+} \sim g(\theta, w_{ch}^{+}, w_{ob}^{+}) \tag{4-6}$$

As shown in Figure 4-7, the flow over sides M1 and M4 in the secondary channel can be considered unbounded. Thus the vertical fin walls in a secondary channel can be partitioned into four sections by two perpendicular planes, such that flow can be assumed to be Falkner-Skan flow along M1 and M4, and internal flow along M2 and M3.

From the Falkner-Skan solution for flow with free-stream velocity varying as $u_{\infty} = Cx^{m}$ where $m = \dfrac{-\theta/\pi}{2-(-\theta/\pi)}$, the friction factor f is given by

$$f = \frac{2\zeta''(0)}{\left(u_{\infty} x/\upsilon\right)^{1/2}} \tag{4-15}$$

where $\zeta''(0)$ is available as a numerical solution related to *m*.

Next, considering a developing fluid flow in a rectangular duct with a short side a and a long side b, its channel aspect ratio is defined as $\alpha=a/b$, for such flow, the *fRe* factors can be approximated by the following equation[142]:

$$fRe = 24(1-1.3553\alpha+1.9467\alpha^2-1.7012\alpha^3+0.9564\alpha^4-0.2537\alpha^5) = 24f(\alpha) \tag{4-16}$$

With the known parameters of fluid density, average velocity and hydraulic diameter, the total pressure drop can be obtained by summing the pressure drop across the different sections:

$$\Delta p_{total} = \sum \Delta p = \frac{2\rho u_m^2}{D_h} \sum (fL) \tag{4-7}$$

Therefore the friction factor of secondary channel will be integrated along each sectional length and then averaged by the total length.

$$(f\,\mathrm{Re})_{\sec} = \frac{\mathrm{Re}_{\sec}}{2w_w/\sin\theta}\left(\int_0^{w_{ob}\cos\theta} f_{M1}dx + \int_{w_{ob}\cos\theta}^{w_w/\sin\theta} f_{M2}dx + \int_0^{(w_w/\sin\theta - w_{ob}\cos\theta)} f_{M3}dx + \int_{(w_w/\sin\theta - w_{ob}\cos\theta)}^{w_w/\sin\theta} f_{M4}dx\right) \tag{4-18}$$

where

$$f_{M1} = f_{M4} = \frac{2\zeta''(0)}{(u_\infty x/\upsilon)^{1/2}} \tag{4-19}$$

$$f_{M2} = f_{M3} = \frac{24f(\alpha)}{\mathrm{Re}_{\sec}} = \frac{24f(\alpha)}{u_{\sec}D_{h_{\sec}}/\upsilon} \tag{4-20}$$

$$\alpha_c = \frac{w_{ob}\sin\theta}{H} \tag{4-21}$$

$$D_{h_{\sec}} = \frac{2Hw_{ob}\sin\theta}{H + w_{ob}\sin\theta} \tag{4-22}$$

From equations 4-15 to 4-22, we can see that there are seven parameters, that is six dimensional parameters ($u_{\sec}, u_\infty, H, w_{ob}, w_w, \upsilon$) and oblique angle θ, for

the response variable $(fRe)_{sec}$. From Eq.(4-14), it is understood that $\frac{u_{\sec}}{u_\infty}$ is already a function of dimensionless parameters group $(\theta, \frac{w_{ch}}{l_u}, \frac{w_{ob}}{l_u})$, and u_∞ can be non-dimensionalized by introducing Reynolds number Re_{main} which represents the Reynolds number of flow in the main channel when no fluid enters secondary channel:

$$\mathrm{Re}_{main} = \frac{u_\infty D_{h_{main}}}{\upsilon} \tag{4-23}$$

Here the hydraulic diameter is defined as follows:

$$D_h = \frac{4 \times \textit{flow volume}}{\textit{fluid contact surface area}} \tag{4-24}$$

Therefore, the $(fRe)_{sec}$ factor in secondary channel can be expressed by dimensionless parameter group $(\mathrm{Re}_{main}, \frac{w_{ch}}{l_u}, \frac{w_{ob}}{l_u}, \frac{w_w}{H}, \theta)$.

The laminar friction factor for secondary channels through 64 different oblique fin array configurations can thus be correlated in the following form:

$$(f\,\mathrm{Re})_{\sec} = C_1 \mathrm{Re}^{C_2} \times (\mathrm{w}_{ob}/l_u)^{C_3} \times (\mathrm{w}_w/\mathrm{H})^{C_4} \times (\mathrm{w}_{ch}/l_u)^{C_5} \times \theta^{C_6} \tag{4-25}$$

The secondary channel in the middle of periodic simulation domain was chosen as the sample channel. Pressure drops and mass flow rates through this channel were collected in ANSYS R15.0 for all 64 cases. Using the definition given in Eq. (4-6)

$$(f\,\mathrm{Re})_{\sec} = \frac{\Delta p}{Q} \frac{D_h^2 \rho A_{eq}}{2L\mu} \tag{4-8}$$

A database containing $(fRe)_{sec}$ factors and corresponding $(\mathrm{Re}_{main}, \frac{w_{ch}}{l_u}, \frac{w_{ob}}{l_u}, \frac{w_w}{H}, \theta)$ for all 64 cases were built. Eq. (4-25) was then solved by encoding the program in OriginPro 9.0 using a multiple regression technique based on the

previous numerical data. After the procedure converged, the five coefficients were determined as follows: C_1= 85.95, C_2 =0.084, C_3 =0.302, C_4 =0.028, C_5 =1.113. The COD (coefficient of determination) of R^2 is 0.986. Therefore, the actual correlation becomes:

$$(f\,\mathrm{Re})_{sec} = 85.945 \times \mathrm{Re}^{0.084} \times (w_{ob}/l_u)^{0.321} \times (w_w/H)^{0.302} \times (w_{ch}/l_u)^{0.028} \times \theta^{1.113} \quad (4\text{-}27)$$

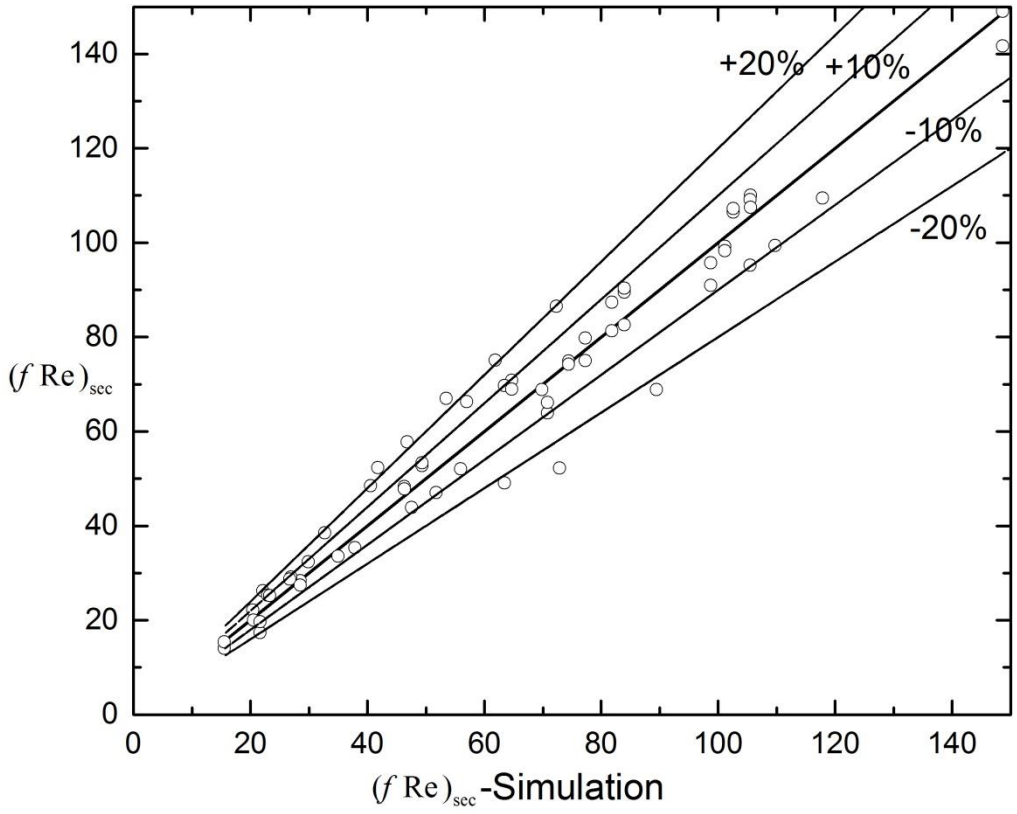

Figure 4-8 Comparison between predicted results and numerical data: variable in x-direction refers to the numerical data from CFD simulations

Figure 4-8 presents a comparison between predicted *(fRe)$_{sec}$* and numerical data; it can be seen that 76.5% of the data are within 10% deviation while 90.6% of the data are within 20% deviation.

4.5. Results and Discussion

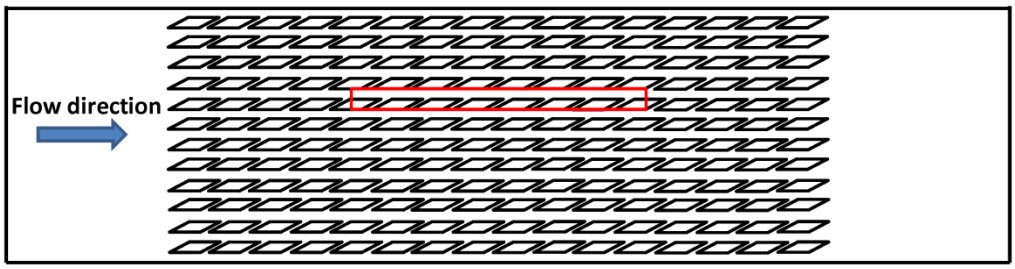

(a)

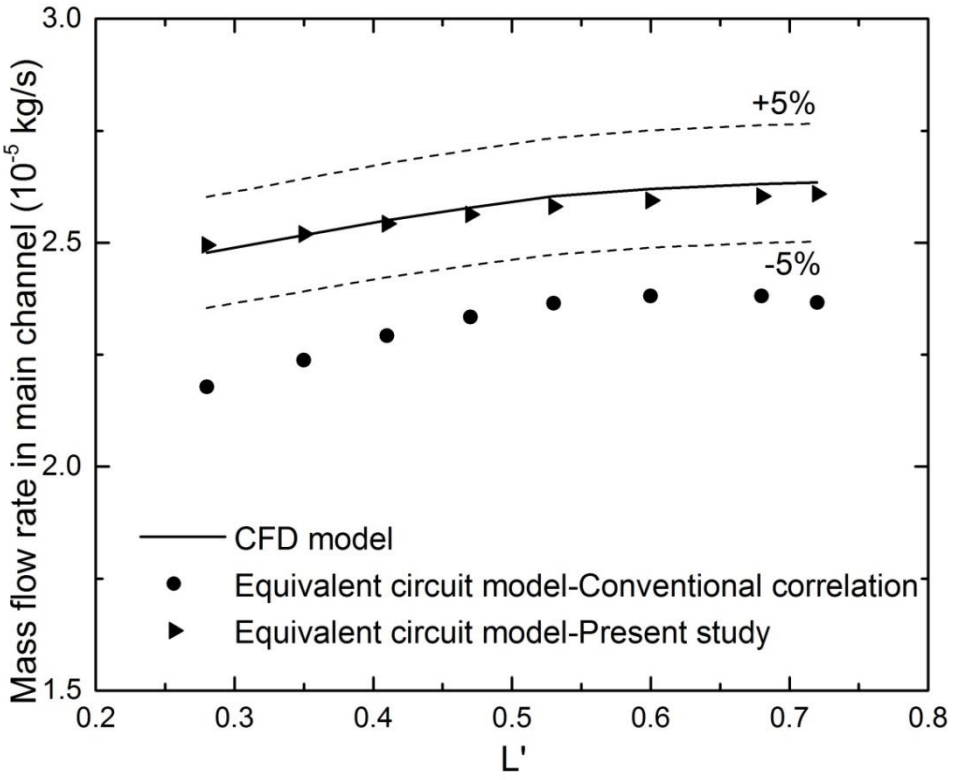

(b)

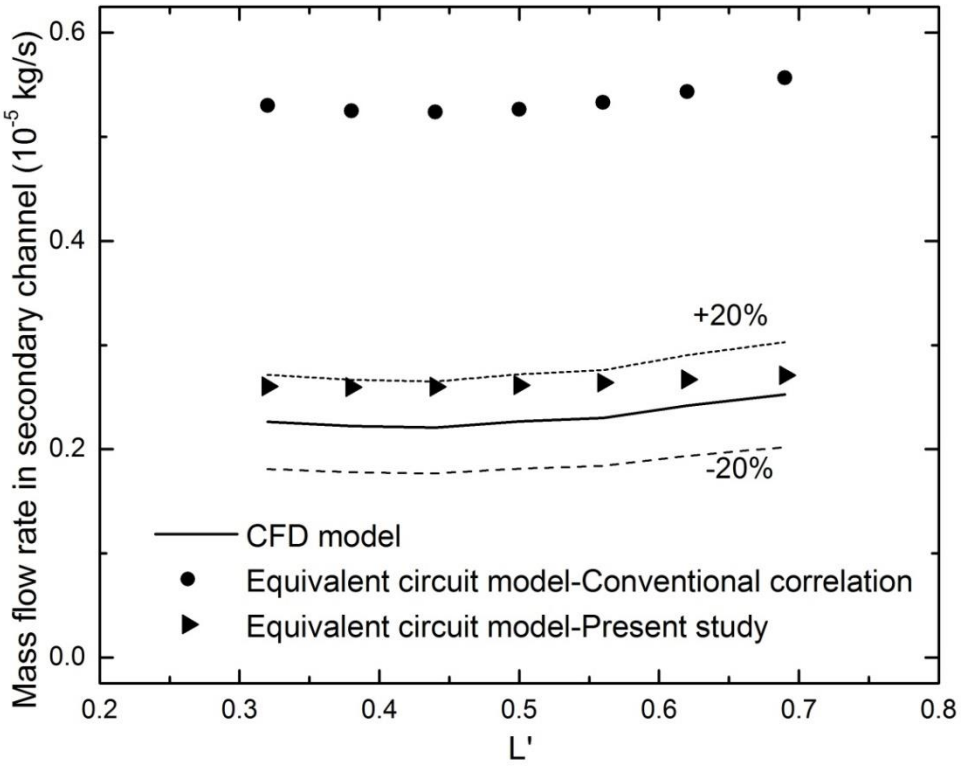

(c)

Figure 4-9 (a) Outline of flow configuration of Case 1, and comparison of mass flow rate in (b) main channels; (c) secondary channels

Channels in the 5th row of the 12x16 fin array (shown in Figure 4-9(a)) are investigated and it is found that the results from reduced flow model using conventional correlation of friction factor assuming hydraulic developing flow (results of Curr et al.[141]) showed large deviation from results from CFD model, especially in the prediction of secondary flow. Results from reduced flow model using the correlations developed in the present study are also presented in Figure 4-9. As shown in Figure 4-9, adopting the new correlations for hydraulic resistances in the primary and secondary channels significantly improves the accuracy of flow distribution prediction. The prediction of mass flow rate in the main channel almost overlaps with the results from CFD

simulation; the improvement in the prediction of secondary flow is even more prominent, where the deviation decreases from around 200% (using conventional correlation) to less than 20%.

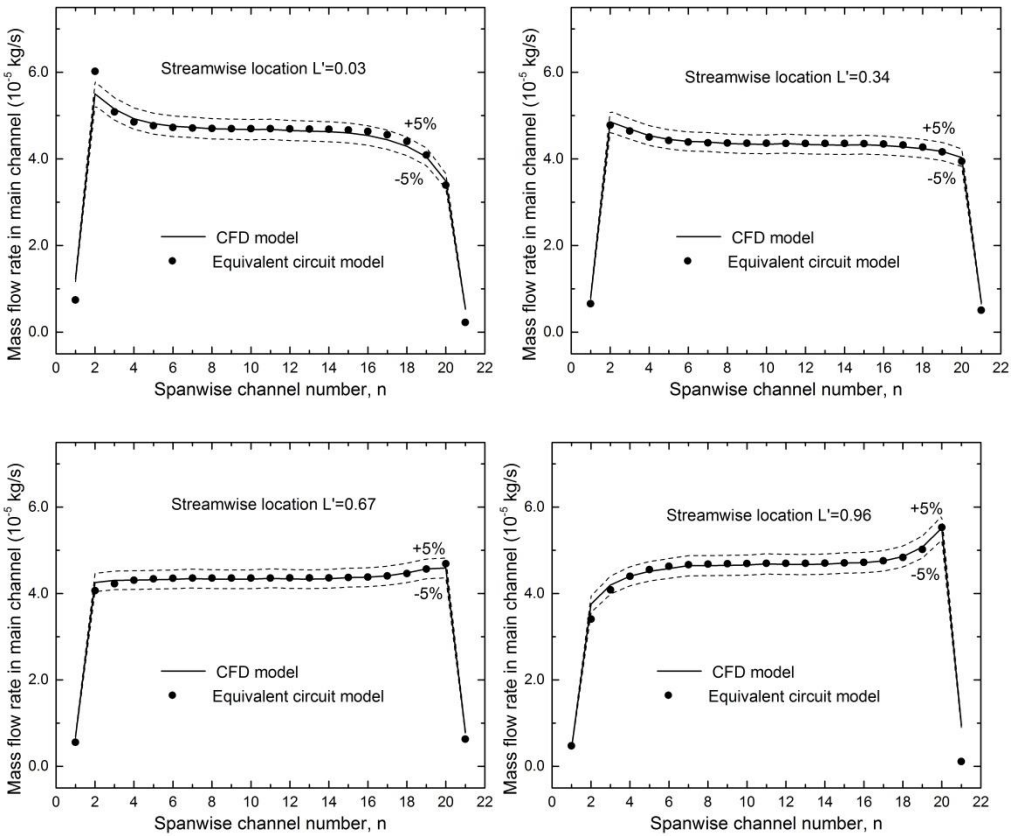

Figure 4-10 Comparison of mass flow rate in main channels of Case 2

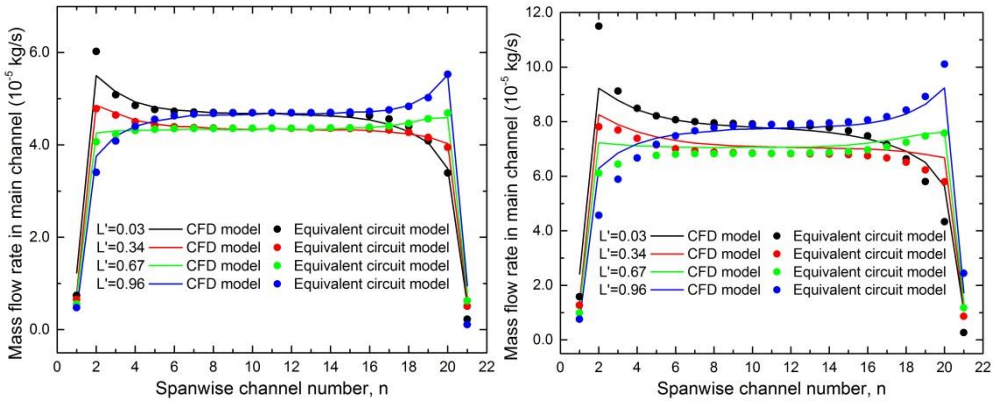

(a) **(b)**

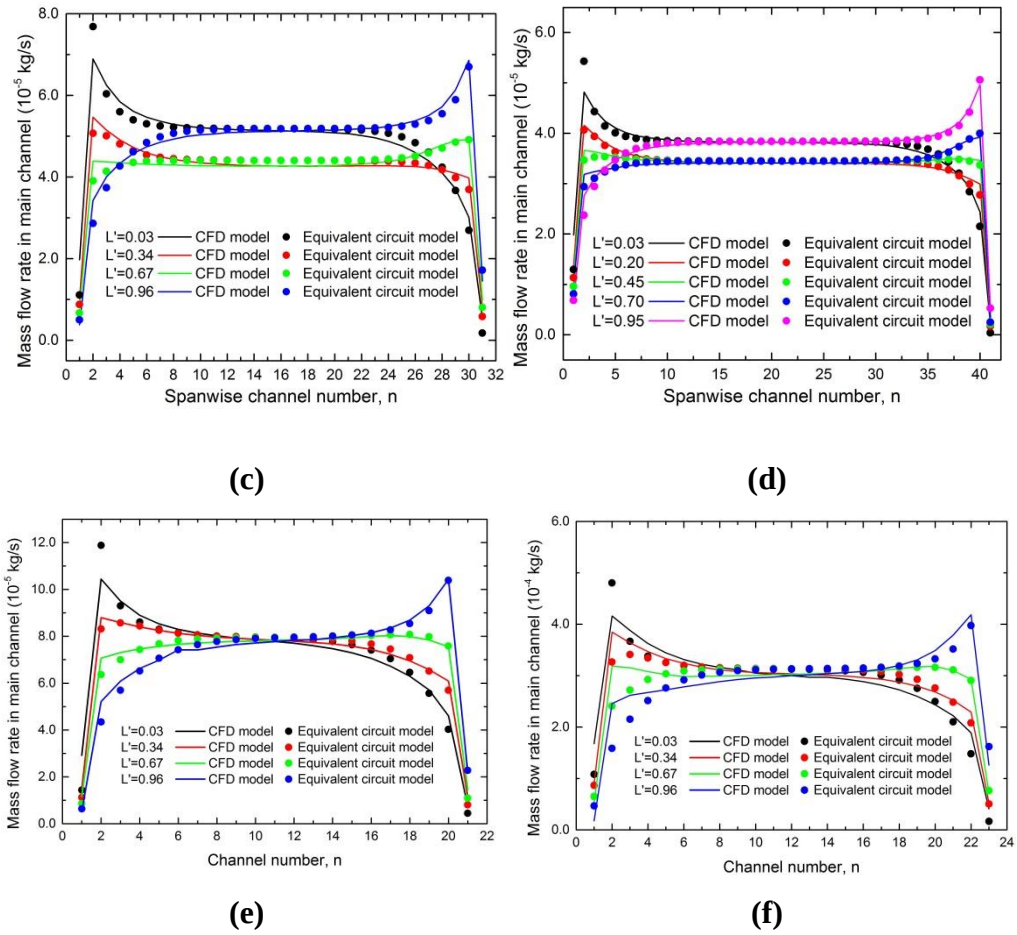

Figure 4-11 Comparison of mass flow rate in main channels of (a) Case 3; (b) Case 4; (c) Case 5; (d) Case 6; (e) Case 7 and (f) Case 8

Further comparisons between the equivalent circuit model of this study and CFD simulations for Case 2 to case 8 are shown in Figure 4-10 and Figure 4-11. Restricting the ratio of unit length to unit width around 2, fin number, aspect ratio, fin pitch, fin length, oblique angle and inlet velocity were varied, and almost all predicted results fall within ±5% deviation from the results of CFD models, especially for the regions away from side walls of simulation domains. This highlights the suitability of the methods used in this study for friction factor calculations in planar secondary flow generating oblique configurations. The equivalent circuit model, which utilizes these calculations

to estimate hydraulic resistances, is thus able to predict the mass flow distribution within oblique configurations with excellent accuracy while greatly shortens the calculation time (i.e. the calculation time of Case 7 is shortened to less than 15 minutes from around 4 days).

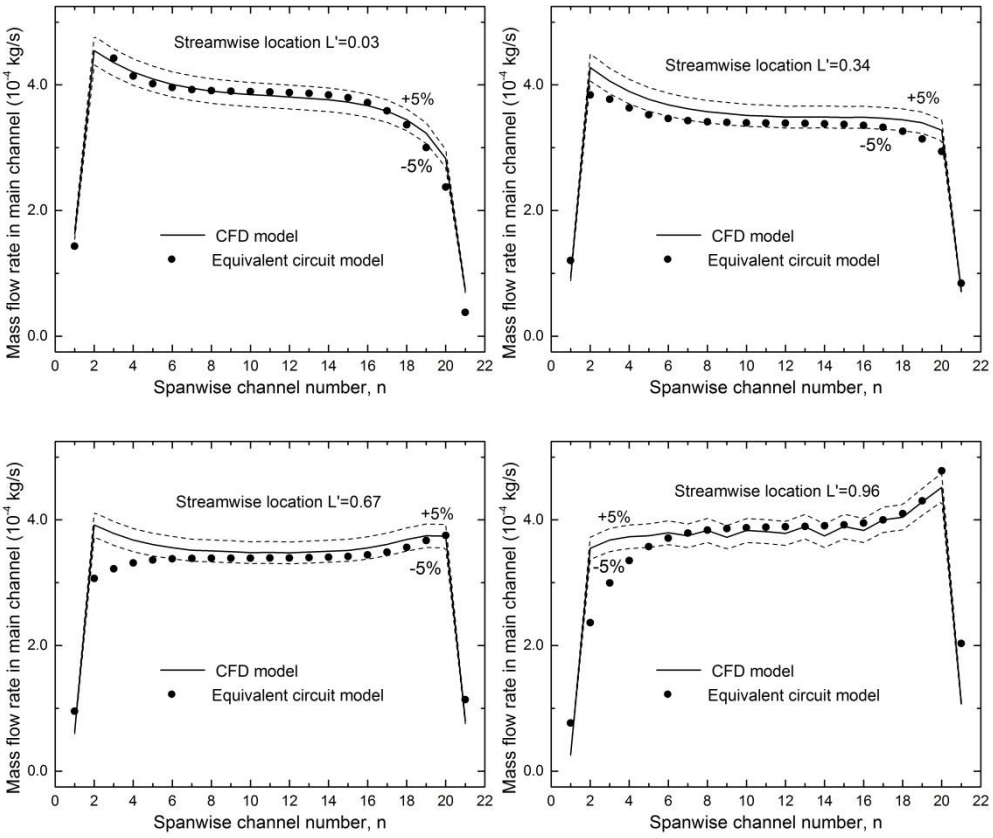

Figure 4-12 Comparison of mass flow rate in main channels of Case 9

Finally, Figure 4-12 shows the comparison of mass flow rate in main channels of case 9. Case 9 shares the same geometry design with case 3 except that its inlet velocity increases to 8 times larger. From the comparison, most results of reduced flow model still fall within ±5% from the results of CFD model but a large deviation occurs for spanwise channel number smaller than 6 at the streamwise location L'=0.67 and L'=0.96, which is also observed in the

comparison of case 8 shown in Figure 4-11. Such large deviation can be attributed to the complex flow caused by large velocity. Figure 4-13 shows the velocity streamlines of Case 9. It is seen that when the fluid leaves the fin region, many vortexes are formed. The largest vortex is exactly situated in small spanwise channel number, which has a great impact on the flow distribution in fin regions nearby. Now, the equivalent circuit model is not able to capture the flowing situation outside the fin region, hence the impact of such vortices is neglected. This simplification is a limitation, and may therefore lead to deviations in prediction of flow distributions in affected areas under certain flow conditions.

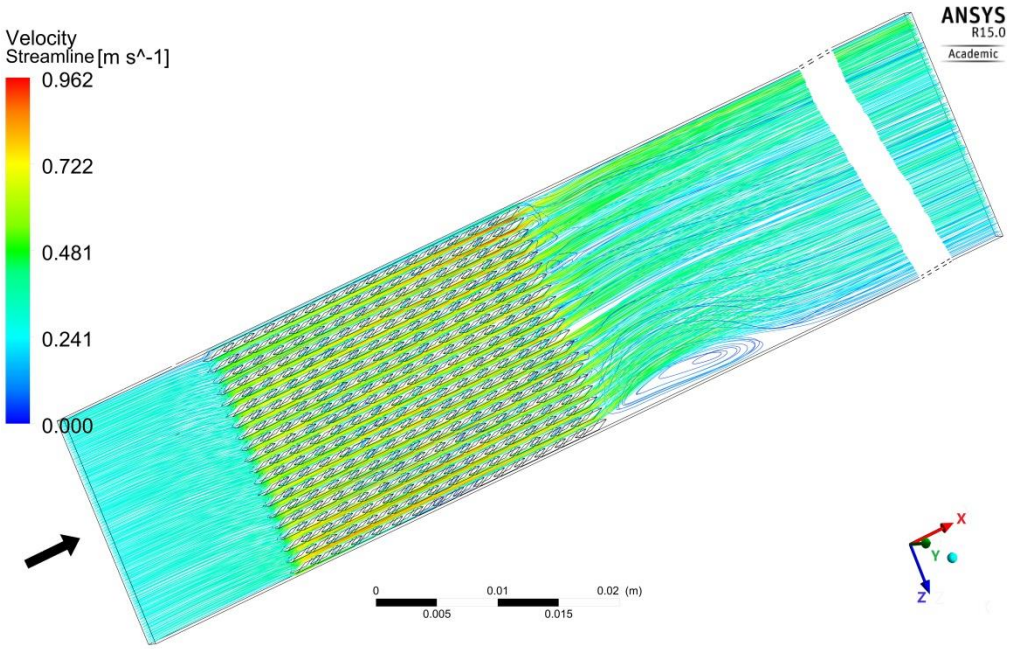

Figure 4-13 Velocity streamlines of Case 9

4.6. Conclusion

A reduced equivalent circuit fluid flow model has been developed to predict

the flow distribution in planar secondary flow generating oblique fin configurations. Separate correlations for friction factors, and therefore hydraulic resistances, in the main and secondary channels have been developed, which appropriately capture the unique features of fluid flow in each. Full-domain geometry-based simulations were performed using CFD approach serving as a benchmark for the equivalent circuit fluid flow model. Detailed comparisons between the results of the reduced model and numerical simulation by CFD approach demonstrated that the model can accurately predict the mass flow distribution with the fin number, aspect ratio, fin pitch, fin length, oblique angle and inlet velocity varying within the actual application scope. The deviation from the results of full domain numerical simulation is generally less than $\pm$5%. Slightly higher deviation exists at the high inlet velocity as a result of vortexes lying close to the end of the trailing edge of the oblique fin region. The advantages of this new model are that it (1) greatly simplifies simulation procedures, (2) shortens the simulation time and post-processing time; (3) reduces the dependence on computer performance.

Related Publications:

- N. Mou, P.S. Lee, S.A. Khan, Coupled equivalent circuit models for fluid flow and heat transfer in large connected microchannel networks – the case of oblique fin heat exchangers, International Journal of Heat and Mass Transfer, Accepted
- N. Mou, P.S. Lee, S.A. Khan, A Simplified ‘Effective Circuit’Fluid Flow Model for Forced Convection in Oblique Fin Configuration, ASME 2014

International Mechanical Engineering Congress and Exposition, American Society of Mechanical Engineers, 2014, pp. V8A-V10A.

CHAPTER 5 REDUCED EQUIVALENT CIRCUIT THERMAL MODEL

In this chapter, a reduced equivalent circuit thermal model is developed to predict temperature distribution in an oblique fin array used in enhanced heat transfer applications. Appropriate Nusselt number correlations and thermal resistance models are employed to predict the temperature distribution associated with the mass flow distribution obtained from the equivalent circuit flow model described in Chapter 4. Detailed full-domain numerical (CFD) simulations are performed to serve as benchmarks for the proposed equivalent circuit model. Detailed comparisons between the results of reduced model and numerical simulation are performed.

5.1. Theoretical Approach

Similar to the electrical-hydraulic analogy, there exists an electrical analogy with heat transfer that can be exploited to solve problems of thermal potential 'circuit' distributions. Here, the heat flow rate q is analogous to current I, and the temperature difference ΔT is analogous to voltage drop ΔV. From this perspective, we can define an Ohm's law analog for thermal circuits as:

$$\Delta T = R_t q \tag{5-1}$$

where R_t is the thermal resistance.

For conductive and convective heat transfer, R_t is calculated respectively as:

$$R_{t,cond} = \frac{l_b}{Ak} \tag{5-2}$$

$$R_{t,conv} = \frac{1}{Ah} \tag{5-3}$$

Where l_b is the thickness of thermal conduction material, k is the thermal conductivity, A is the cross-sectional area or convective heat transfer area, h is the convective heat transfer coefficient.

The electrical-thermal analogy can be adopted to simulate the complex heat transfer in planar secondary flow generating oblique fin units. A basic scheme for the equivalent circuit for convective heat transfer in an oblique unit is provided in Figure 5-1. The total electrical potential drop ΔV of this equivalent circuit represents the average temperature difference between the heating surface and fluid domain. A representative oblique unit is depicted in Figure 5-1(a) and (b). Its corresponding reduced equivalent circuit model is shown in Figure 5-1(c). Resistor 1 represents the thermal conduction resistance across the base of the heat sink, resistor 2 represents the thermal conduction resistance across the fin, resistor 3 represents the thermal convection resistance on the fin surface, and resistor 4 represents the thermal convection resistance on exposed base surface between fins.

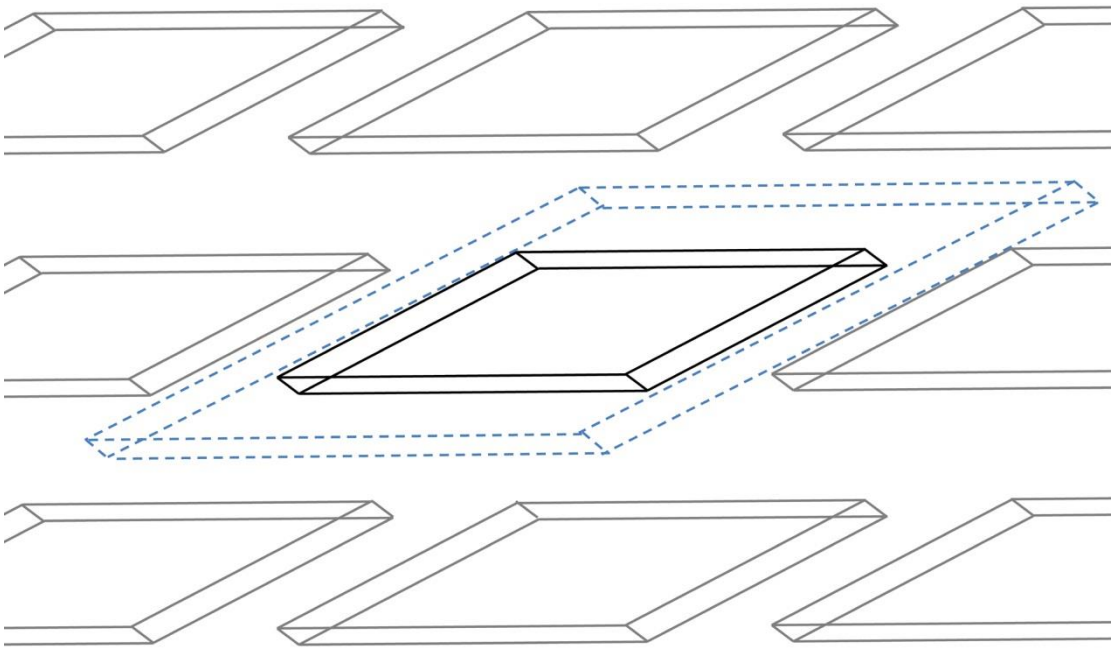

(a)

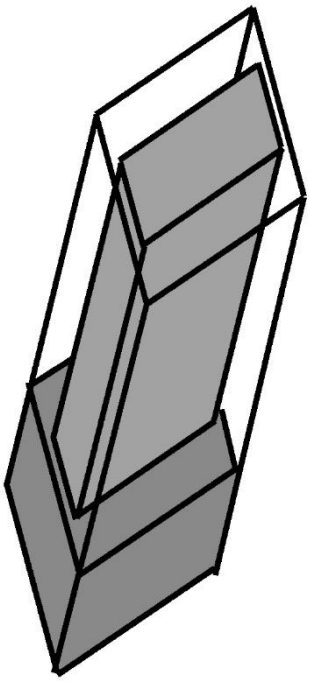

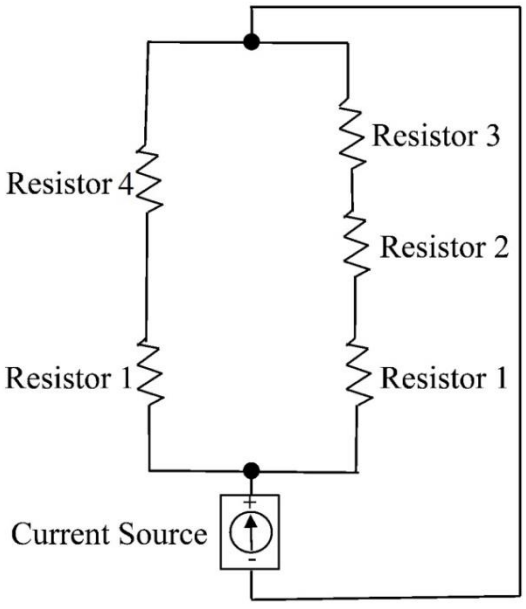

(b) **(c)**

Figure 5-1 Schematic of an equivalent circuit for convective heat transfer in an oblique unit

5.2. Methodology

Two different methodologies will be introduced in details in this section. First, we describe numerical simulations using computational fluid dynamics (CFD). Next we describe the development of our equivalent circuit model, involving the assumptions and determination of resistances and thermal resistance models.

5.2.1. Numerical Simulation Methodology

3D conjugated numerical simulations on the forced convective flow through the oblique fin array were carried out using ANSYS R15.0 to (1) understand the uniqueness of heat transfer in oblique fin configurations and (2) serve as a benchmark for the reduced equivalent circuit model.

The flow model set and governing equations for fluid domain were the same as described in Chapter 3 and Chapter 4. The thermal energy equation is added to the governing equations as:

$$\nabla\bullet\left(\rho u h\right)=\nabla\bullet\left(\lambda\nabla T\right)+\tau:\nabla u+S_E \tag{5-4}$$

The inlet temperature of the coolant (liquid-water in this case) was set as room temperature 298.15K (25 $^{\circ}C$). A prescribed velocity was applied at the inlet and gauge pressure at the outlet was set as 0 Pascal. In the 3D conjugated simulation, the substrate material is copper. The heat flux of 10W/cm^2 for Case 7 and 65W/cm^2 for Case 8 was supplied evenly from the bottom of the

substrate respectively while the top surface of the copper material was assumed bonded with an adiabatic material. A residual value of 1×10^{-6} was set as the convergence criteria for the continuity equation, x-velocity, y-velocity z-velocity and energy equation. The same grid size as described in Chapter 4 was also used.

A sample of the full simulation domain is shown in Figure 5-2 and dimensional details are shown in Table 4-2 as Case 7 and Case 8.

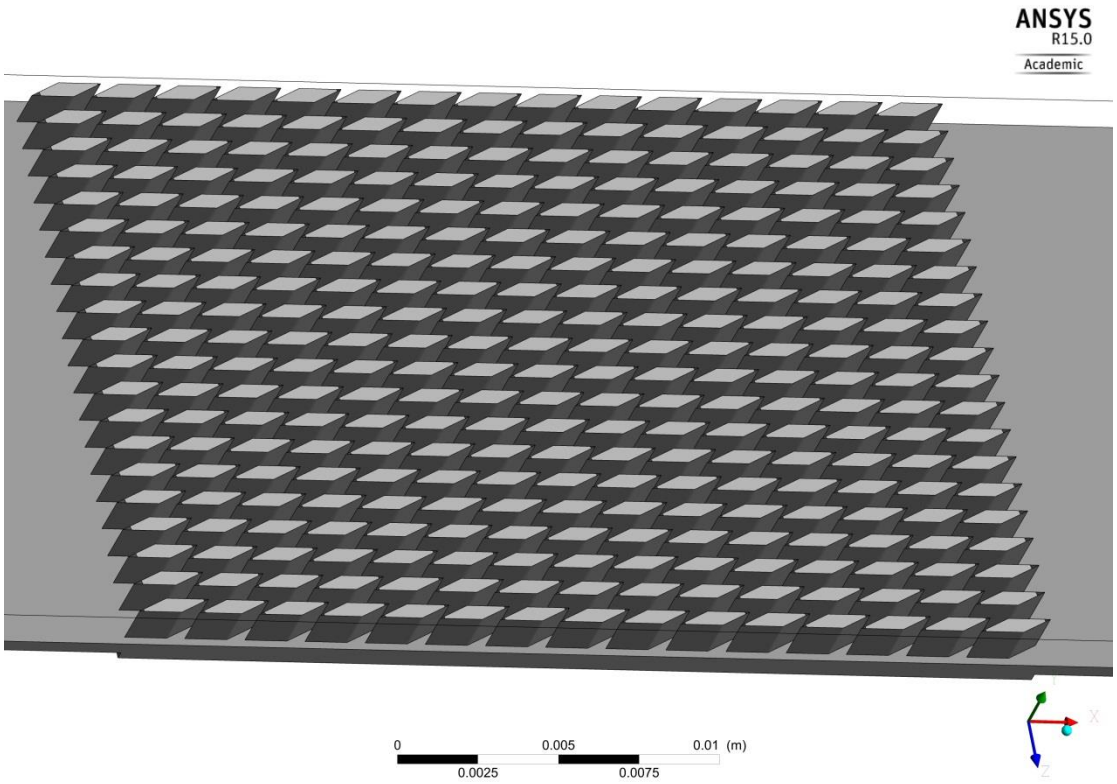

Figure 5-2 Full computation domain for oblique fin configurations

5.2.2 Reduced Equivalent Circuit Thermal Model

The corresponding reduced equivalent circuit model of a representative oblique unit is shown in Figure 5-1(c). The calculation of heat transfer is

divided into three steps: (i) determination of thermal resistance model, (ii) determination of heat flux and calculation of fluid temperature, and (iii) calculation of the substrate base temperature.

5.2.2.1. Determination of thermal resistance

As shown in Figure 5-1, the total thermal resistance is composed of the thermal conduction resistance across the base of the heat sink, the thermal conduction resistance across the fin, the thermal convection resistance on the fin surface and the thermal convection resistance on exposed base surface between fins. For the calculation of the thermal convection resistance on the fin surface and that on exposed base surface between fins, a unified convective heat transfer coefficient is employed.

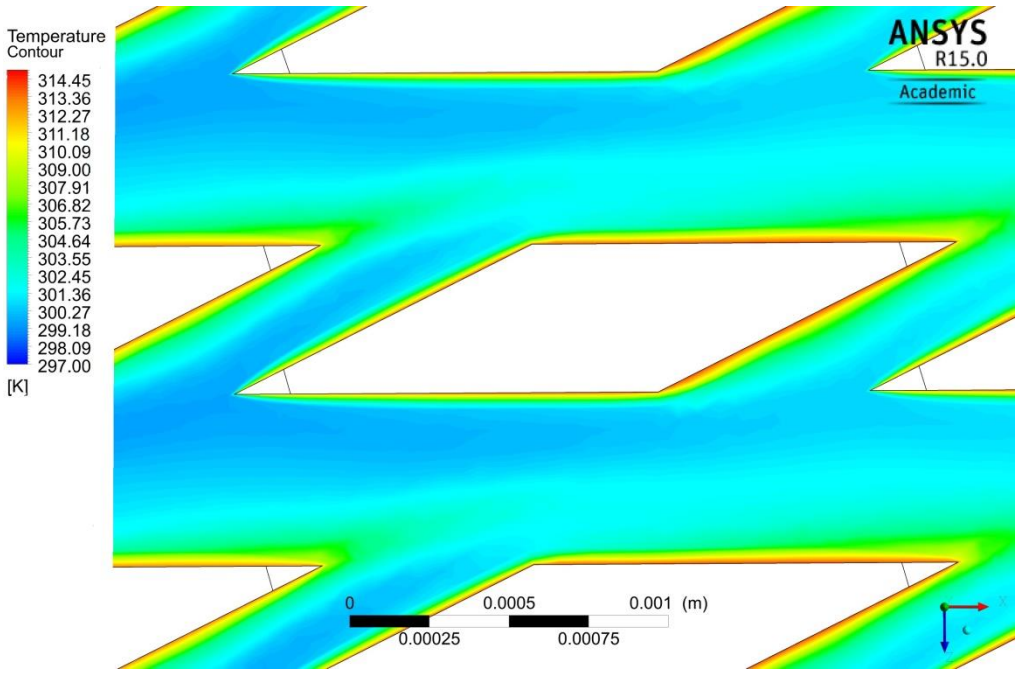

Figure 5-3 Fluid temperature contour of mid-depth plane for Case 8

As shown in Figure 5-3, due to the presence of oblique cuts, the thermal

boundary layer on each fin surface is periodically disrupted by the disappearance of attached surface and the impact of fluid from cross channel and then reinitialized. The length of oblique fin is designed so small that the convective heat transfer occurred on the oblique fin surfaces is maintained in the thermal developing regime. The demarcation between the developing regime and the fully developed regime proposed by Lee et al. [146] is employed to further valid this explanation with a dimensionless thermal entrance length z_{th}^* calculated as:

$$z_{th}^* = -1.275\times10^{-6}\alpha^{*6} + 4.709\times10^{-5}\alpha^{*5} - 6.902\times10^{-4}\alpha^{*4} + 5.014\times10^{-3}\alpha^{*3} - 1.769\times10^{-2}\alpha^{*2} + 0.01845\alpha^{*} + 0.05691 \tag{5-5}$$

Through calculation, the values of z_{th}^* for Case 7 and Case 8 are 62.69 and 62.71, both of which are much larger than their x^*. Thus, two different methods for the calculation of average Nusselt number in developing regime are considered. One method is the equation developed by Lee et al. [146] which calculates the average Nusselt number as:

$$Nu_{ave} = \frac{1}{C_1\left(x^*\right)^{C2} + C_3} + C_4 \tag{5-6}$$

where

$$x^* = \frac{l}{D_h \times \mathrm{Re} \times \mathrm{Pr}} \tag{5-7}$$

$$C_1 = -2.757\times10^{-3}\alpha^{*3} + 3.274\times10^{-2}\alpha^{*2} - 7.464\times10^{-5}\alpha^{*} + 4.476 \tag{5-8}$$

$$C_2 = 0.6391 \tag{5-9}$$

$$C_3 = 1.604\times10^{-4}\alpha^{*2} - 2.622\times10^{-3}\alpha^{*} + 2.568\times10^{-2} \quad (5\text{-}10)$$

$$C_4 = 7.301 - 13.11\times10/\alpha^{*2} + 15.19/\alpha^{*2} - 6.094/\alpha^{*3} \quad (5\text{-}11)$$

where α^{*} is the newly proposed aspect ratio in present study defined in Eq. (4-10). *l* is the length of an oblique fin.

The other is the Generalized Leveque Equation [128] which calculates the average Nusselt number as:

$$Nu = 0.403755\times\left(\xi\,\mathrm{Re}^2\,D_h P_r / l_u\right)^{1/3} \quad (5\text{-}12)$$

where l_u is the oblique fin pitch, and ξ is the friction coefficient. To compare the agreement of results from calculation methods with the results from numerical simulations and experiments, ξ was calculated from the numerical simulation using following equation:

$$\xi = \frac{2\times\Delta p\times D_h}{\rho\times L\times u_m^2} \quad (5\text{-}13)$$

Δp is the overall pressure drop across the fin region obtained from numerical simulation, and L is the total length of fin region. The comparison of average Nusselt number from experiment, numerical simulation, correlation of Lee et al. [146] and the Generalized Leveque Equation is shown and discussed in detail in section 5.3.

Using the Nusselt number obtain above, the heat transfer coefficient is given by

$$h_{ave} = \frac{Nu_{ave}\times k_{fluid}}{D_h} \quad (5\text{-}14)$$

To determine the resistances in the equivalent circuit thermal model, we use fin efficiency theory. The thermal conduction resistance across the base of the heat sink R_1 is calculated using Eq. (5-2), while the new thermal resistance model with correction coefficients proposed by Kang et al.[121] is employed to simulate the heat transfer from fin to fluid. Resistance 2, Resistance 3 and Resistance 4 are determined from the following equations:

$$R_2 = \frac{1-\eta_x}{\eta_x A_f h_{ave}} \tag{5-15}$$

$$R_3 = \frac{1}{A_f h_{ave}} \tag{5-16}$$

$$R_4 = \frac{1}{A_b h_{ave}} \tag{5-17}$$

where

$$\eta_x = \frac{\tanh\left(mL^{1.05} NTU_f^{0.008}\right)}{mL^{1.05} NTU_f^{0.008}} \tag{5-18}$$

$$NTU_f = \frac{A_f \times h_{ave}}{Q \times c_p} \tag{5-19}$$

$$mL = \left(\frac{h_{ave} \times A_f \times H}{k_{solid} \times A_c}\right)^{0.5} \tag{5-20}$$

For case 7 and case 8 in present study, the mL is equal to 0.5611 and 0.7512 respectively, and the NTU_f is with the ranges of 0.125~0.55 and 0.05~0.24. Both fall within the application range of the new thermal resistance model as $0< mL <2$ and $0< NTU_f <2.5$.

Finally, the total resistance can be obtained by:

$$R_{tot} = \frac{1}{\frac{1}{R_1 + R_4} + \frac{1}{R_1 + R_2 + R_3}} \tag{5-21}$$

5.2.2.2. Determination of heat distribution

To investigate the influence of the heat conduction between the units, the average heat flux on solid-fluid interface of each unit of Case 7, which is obtained from the CFD model, is presented in Figure 5-4. As shown in the figure, the average heat flux on the solid-fluid interface is distributed uniformly for an overwhelming majority of units, which indicates that the heat conduction between the units is negligible compared to the heat convection on the solid-fluid interface. Therefore it is reasonable to make the assumption that all heat imposed on the heating surface of a unit is transferred to the fluid flowing through the unit, so as to simplify the thermal resistance network model.

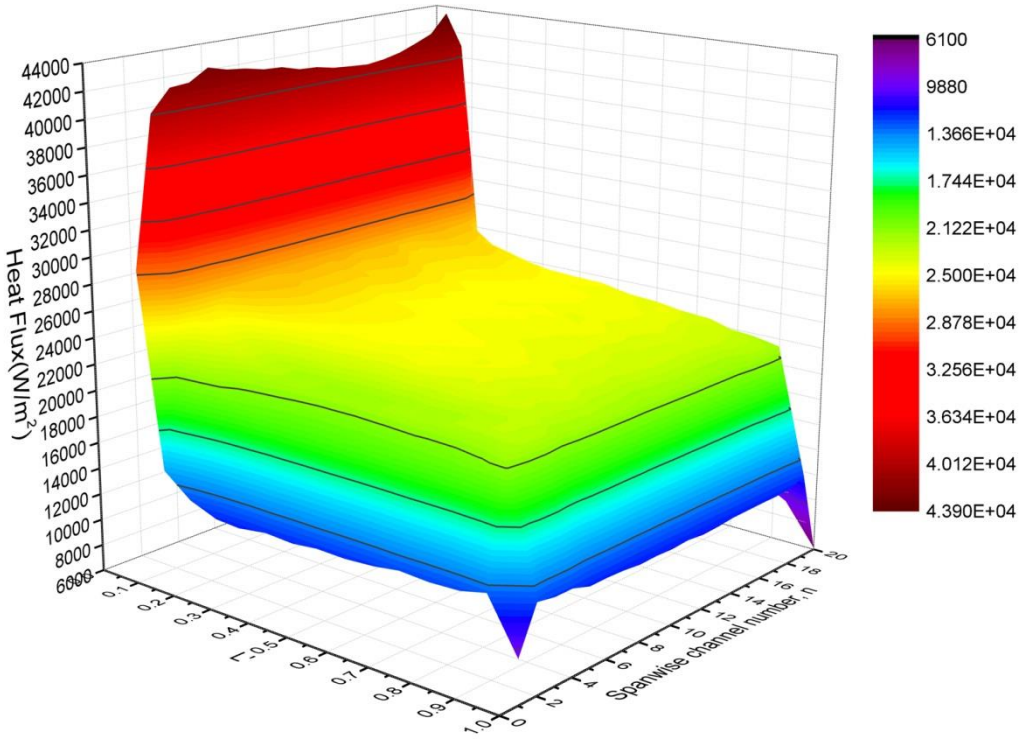

Figure 5-4 Average heat flux on solid-fluid interface of each unit for Case 7

5.2.2.3. Calculation of fluid temperature

With the assumptions that the fluid enters the fin region with a uniform temperature and all heat imposed on the heated surface of a unit is transferred to the fluid flowing through the unit, the average fluid outlet temperature of each unit can be obtained by applying the law of energy conservation and results from the equivalent circuit fluid flow model and calculated as:

$$T_{f_{out},unit} = T_{f_{in},unit} + \frac{q}{mc_p} \tag{5-22}$$

The average fluid temperature of each unit is then calculated as:

$$T_{f_{ave},unit} = \frac{T_{f_{in},unit} + T_{f_{out},unit}}{2} \tag{5-23}$$

5.2.2.4. Calculation of the substrate base temperature

With all the assumptions discussed above, the average substrate base temperature of each unit is then calculated as:

$$T_{s_{ave},unit} = T_{f_{ave},unit} + q \times R_{tot} \tag{5-24}$$

5.3. Results and Discussion

5.3.1. Validation of Numerical Simulation and Correlation Prediction

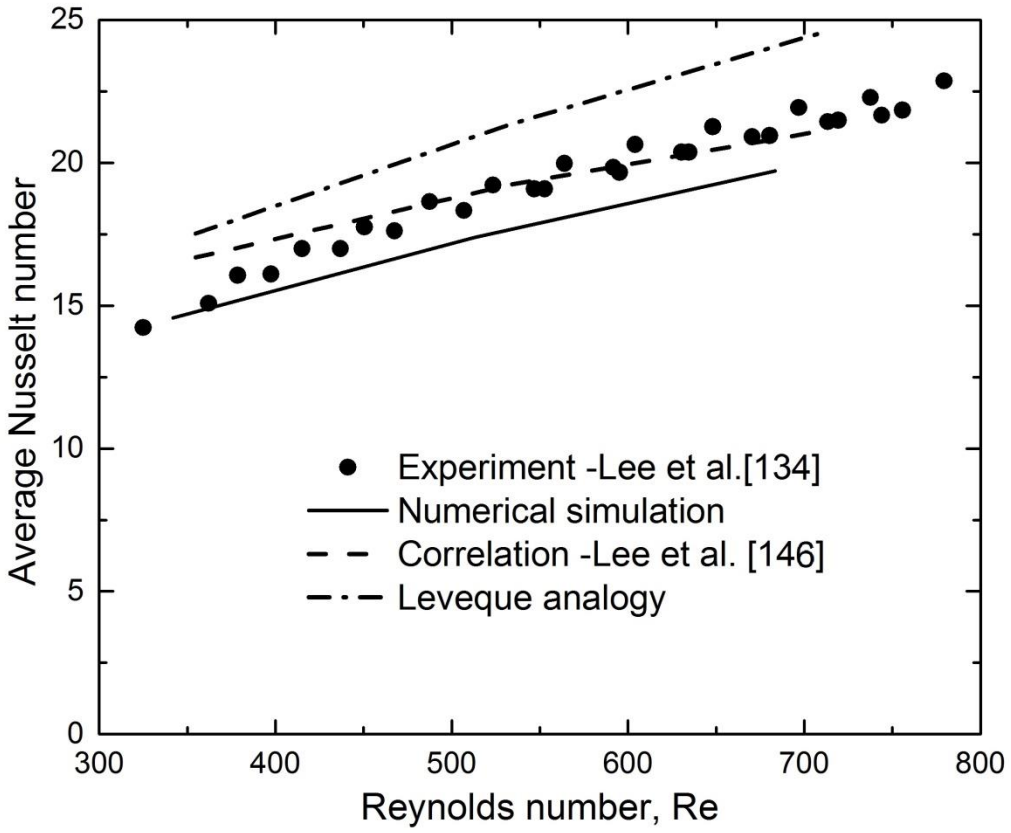

Figure 5-5 Comparison of average Nusselt number

The same grid size and model set were used to numerically simulate the configuration with 500μm nominal channel width described by Lee et al.[134] with dimensions being listed as case 8 in Chapter 4. The comparison of average Nusselt number between experiments, numerical simulation, correlation of Lee et al. [146] and Generalized Leveque Equation is shown in Figure 5-5. It is found that the deviation between results of experimental, numerical simulation and correlation of Lee et al. [146] is relatively small under all conditions, which indicates that the results of numerical simulation is

reliable to serve as a benchmark and using the correlation of Lee et al. [146] for the calculation of average Nusselt number of oblique fin geometry is appropriate. On the contrary, the results from the Generalized Leveque Equation show relatively larger deviation from the results of experiment and numerical simulation, thus the method is deprecated for the oblique fin geometry.

5.3.2. Comparison of Average Fluid Temperature

Figure 5-6 and Figure 5-7 show the comparison of average fluid temperature obtained from equivalent circuit model and CFD model for Case 7 and Case 8 respectively. Due to the fact that the fluid mass flow rate in the main channels varies in both spanwise and streamwise direction, sensible heat gain by fluid results in different local fluid temperature rise. The higher fluid flow rate results in the lower fluid temperature in small spanwise channel number at L'=0.03 and L'=0.34, while the opposite is also true for the large spanwise channel number. The fluid mass flow rate distribution changes as the fluid flows downstream, and thus the fluid temperature distribution in spanwise direction changes correspondingly. Slight difference is observed for the fluid temperature distribution at L'=0.96 of Case 8, which can be attributed to the vortexes explained in Section 4.5. The comparison indicates that the equivalent circuit model is able to capture the average fluid temperature variation trend accurately. The agreement is satisfactory, mostly within $\pm$5%.

Slightly higher deviations are detected in the edge regions, which can be attributed to deviation of mass flow prediction and the assumption of uniform heat flux distribution in the edge regions.

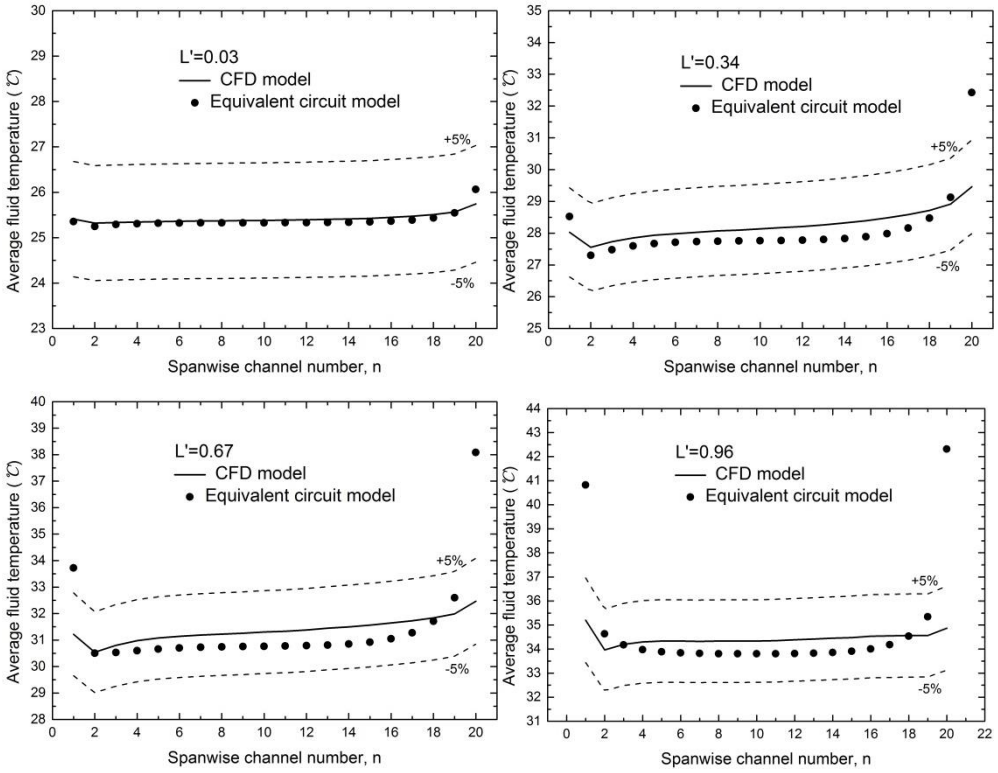

Figure 5-6 Comparison of average fluid temperature for Case 7

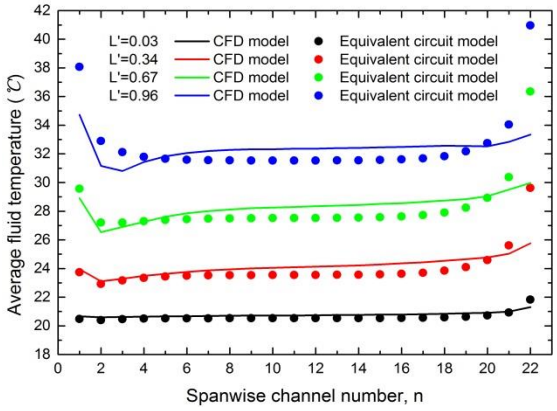

Figure 5-7 Comparison of average fluid temperature for Case 8

5.3.3. Comparison of Average Substrate Base Temperature

Figure 5-8 and Figure 5-9 show the comparison of average substrate base

temperature obtained from equivalent circuit model and CFD model for Case 7 and Case 8 respectively. It is found that the temperature distribution on the substrate base is also influenced by the flow migration within the fin region. The phenomenon is captured by both the CFD model and the equivalent circuit model. It is noticed that the variation of substrate base temperature is smoother compared to that of the average fluid temperature due to the large thermal conductivity of copper. Therefore, neglecting the horizontal heat conduction within the base introduces some deviation in the prediction of substrate base temperature distribution using equivalent circuit model. But the agreement is still satisfactory, mostly within $\pm$5%.

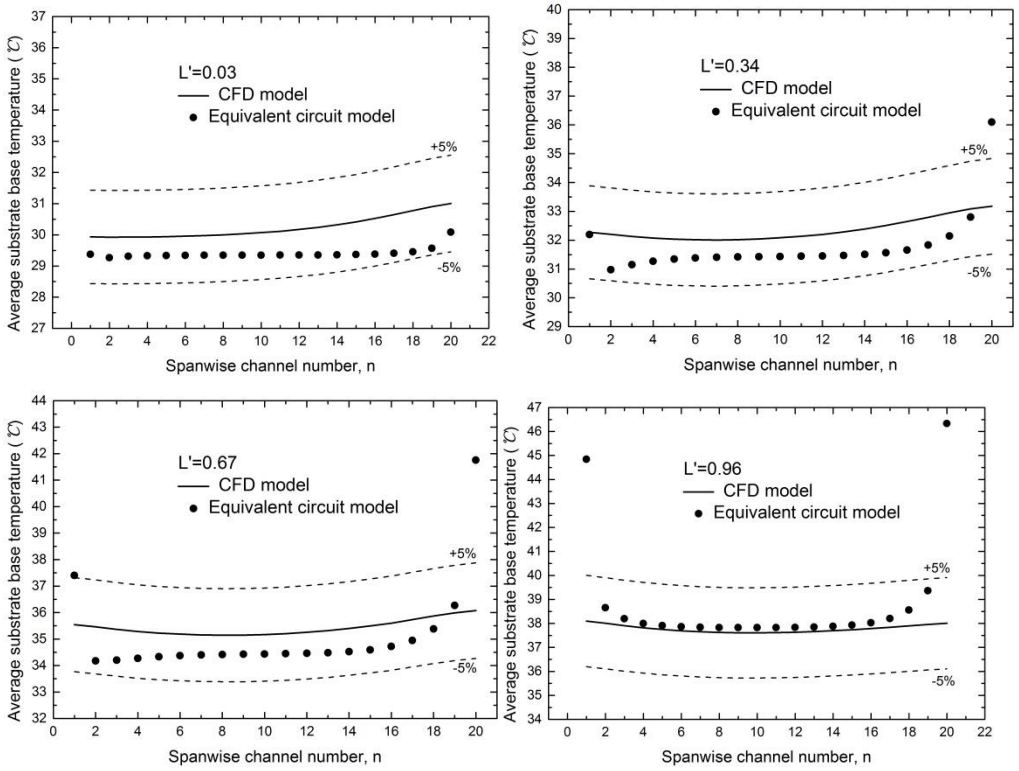

Figure 5-8 Comparison of average substrate base temperature for Case 7

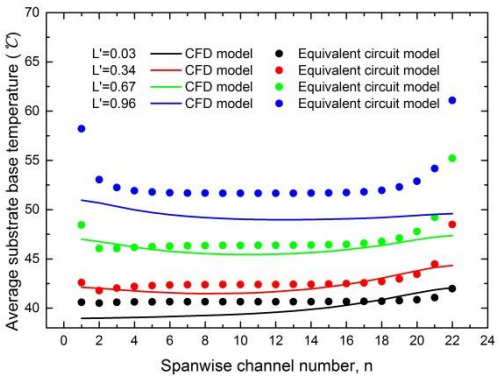

Figure 5-9 **Comparison of average substrate base temperature for Case 8**

5.4. Conclusions

A reduced equivalent circuit model has been developed to predict the temperature distribution in planar secondary flow generating oblique fin configurations. Appropriate Nusselt number correlations and thermal resistance models are employed to predict the temperature distribution associated with the mass flow distribution obtained from the reduced equivalent circuit fluid flow model. Full-domain geometry-based simulations were performed using CFD approach serving as a benchmark for the equivalent circuit model. Detailed comparisons between the results of the reduced model and numerical simulation by CFD approach demonstrated that the model can accurately predict the average temperature distribution of the fluid and the substrate base. The deviation from the results of full domain numerical simulation is generally less than $\pm$5%. Slightly higher deviation of temperature prediction is detected in the edge regions, which can be attributed to deviation of mass flow prediction and the assumption of uniform heat flux

distribution in the edge regions.

Related Publications:

- N. Mou, P.S. Lee, S.A. Khan, Coupled equivalent circuit models for fluid flow and heat transfer in large connected microchannel networks – the case of oblique fin heat exchangers, International Journal of Heat and Mass Transfer, Accepted

CHAPTER 6 NUMERICAL VALIDATION OF COUPLED EQUIVALENT CIRCUIT MODEL IN COMPLEX CASES

This chapter provides a further numerical validation of coupled equivalent circuit model in variable pitch oblique fin microchannel heat sink and novel spiral microchannel heat sink with curved cuts. Detailed full-domain numerical (CFD) simulations are performed to serve as benchmarks for the coupled equivalent circuit model. Detailed comparisons between the results of reduced model and numerical simulation are performed.

6.1. Variable Pitch Oblique Fin Microchannel Heat Sink

6.1.1. Introduction

Currently, most thermal management design and investigation are conducted based on the assumption of a uniform heat flux on the substrate base. Nevertheless, this assumption cannot be applicable in some actual heat sources and higher heat flux has to be specified to certain base regions. Thus, there is a strong motivation to introduce a new thermal management technique to cope with the hotspots on electronic devices, as the conventional cooling schemes, which are designed for uniform heat flux dissipation, are not effective in cooling hot spots [147]. For this reason, the effect of selectively varying the oblique fin pitch based on the local heat flux level was experimentally

examined by Lee et al.[148]. In a variable pitch oblique fin microchannel heat sink, as shown in Figure 6-1, different densities of oblique fin clusters can be obtained by varying the fin pitch locally. Shorter fin pitch leads to closely packed oblique fin and microchannels, which results in more intense thermal boundary layer reinitialization and secondary flow generation. Thus significant local heat transfer enhancement is achieved. Conversely, longer fin pitch reduces the density of secondary flow. And thus the heat transfer coefficient will be relatively lower compared to that of the area with dense oblique fin. Such a characteristic turns out to be ideal for the thermal management of heat sources with hot spots. Dense oblique fin cluster can be positioned directly on top of the hot spots to provide more effective heat removal. The experimental results of Lee et al. [148] showed that variable pitch oblique finned microchannel heat sink adapts well to various non-uniform heating conditions and provides effective hotspot suppression. Thus, as a methodology developed for facilitating the design and optimization of heat sinks, it is of great significance to examine the applicability of coupled equivalent circuit model on the variable pitch oblique fin microchannel heat sink.

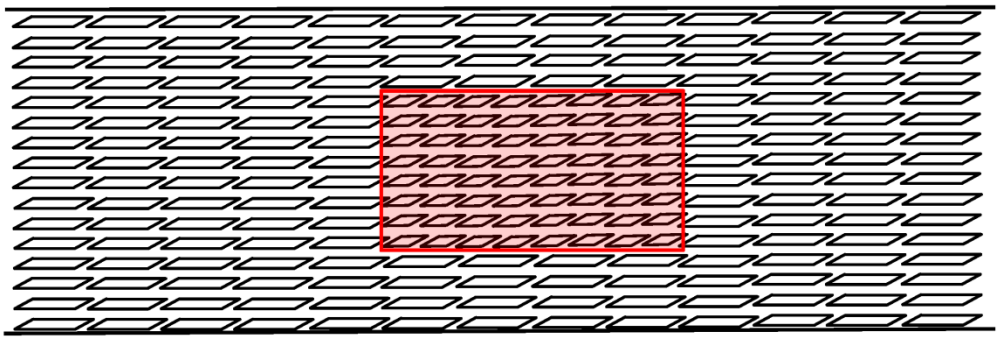

Figure 6-1 Plan view of variable pitch oblique finned microchannel heat sink with hot spot (red colour highlighted)

6.1.2. Methodology

Two different methodologies will be introduced in details in this section. First, numerical simulations using computational fluid dynamics (CFD) is described. Next we describe the coupled equivalent circuit model, involving the setup of reduced equivalent circuit flow model and reduced equivalent circuit thermal model.

6.1.2.1. Numerical Simulation Methodology

3D numerical simulations on the forced convective flow through the variable pitch oblique fin array were carried out using ANSYS R15.0 to serve as a benchmark for the coupled equivalent circuit model. The computational domain is shown in Figure 6-2 while detailed geometries of the model are tabulated in the Table 1. Smaller fin pitch of 388 μm is created directly on top of the hot spot while a larger fin pitch of 776 μm is used for the rest regions. The dimensionless streamwise direction across the oblique fin region and the

main channels/oblique units' number in the spanwise direction are the same as described in previous chapters. The SST model described in Chapter 3 and thermal energy equation described in Chapter 5 are also used in this study.

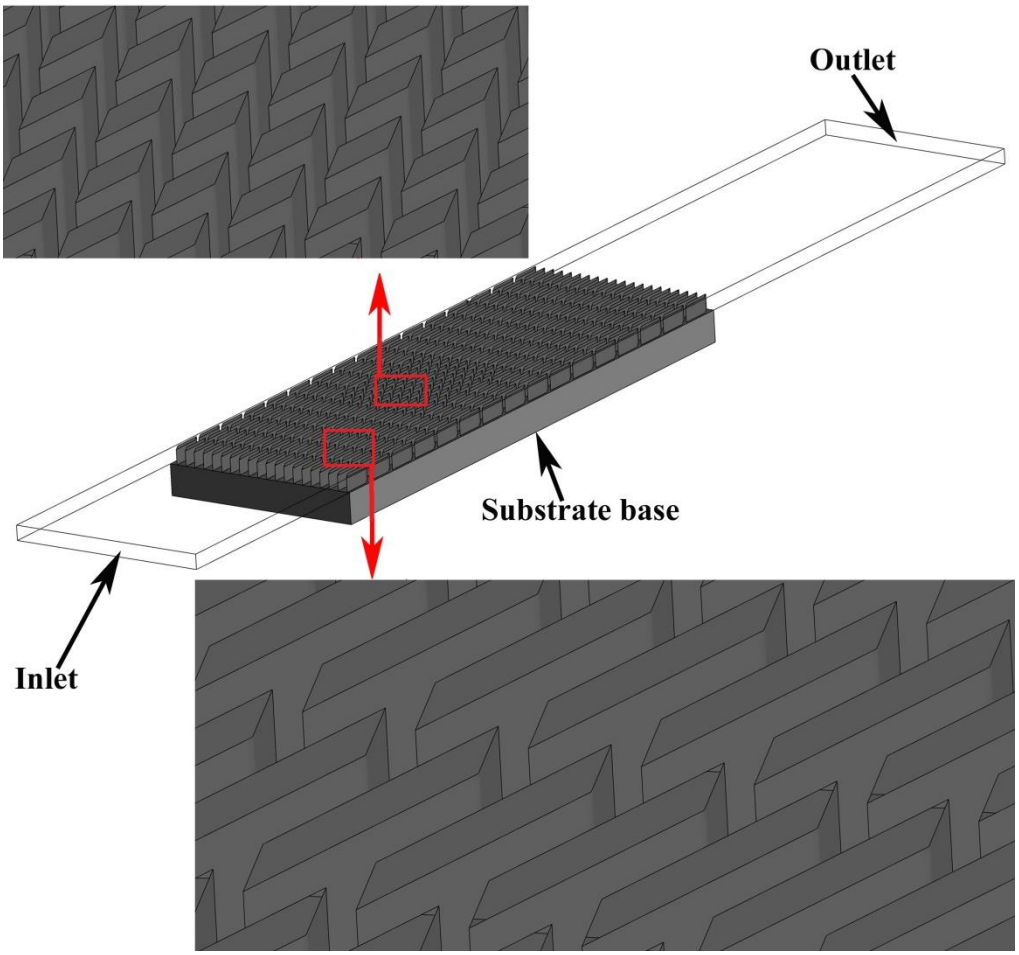

Figure 6-2 Computation domain of variable pitch oblique fin microchannel heat sink

Table 6- 1 Dimensional details of variable pitch oblique fin microchannel heat sink

Characteristic	Variable pitch oblique fin microchannel heat sink
Material	Copper
Footprint, width × lengh, (mm^2)	4.2 × 12.5
Number of fin row, n	20
Main channel width, w_{ch} (μm)	105

Fin width, w_w (μm)	105
Channel depth, H (μm)	312
Fin pitch, $l_{u,l}$ (μm)	776
Fin length, l_l (μm)	640
Fin pitch, $l_{u,s}$ (μm)	388
Fin length, l_s (μm)	252
Oblique angel, θ (*deg*)	26.8

The entire computational domain was meshed with max size of 0.08 mm and a total number of 21,660,638 elements were generated. Different grids have been tested, with different max sizes and different first layer thicknesses. Simulations with different grids show satisfactory grid independence. The resultant average Nusselt numbers of 16.62, 15.386, 14.30 and 14.189 were obtained with the mesh counts of 11,627,373; 19,265,033; 21,660,638 and 32,795,672 elements respectively. The variations in Nu_{ave} are 7.4% from the roughest to the rough mesh, and 7.1% from the rough to the finer grid while 0.78% from the finer to the finest grid. Therefore, the intermediate grid (21,660,638 elements) is selected in order to preserve both accuracy and cost.

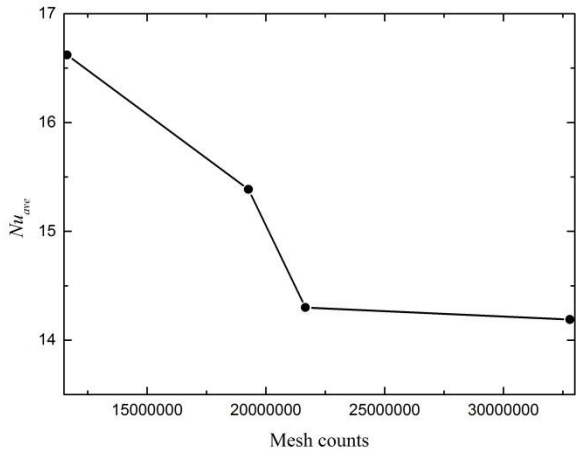

Figure 6-3 Grid independence

Boundary conditions for the numerical simulation include the no–slip and impermeability conditions on all solid boundaries. Water is assigned as the coolant with constant thermophysical properties. The inlet temperature of the liquid–water is set as 20 ℃. A uniform velocity profile of 0.84 m/s is applied at the inlet and pressure outlet condition is prescribed at the outlet. In the 3D conjugate simulation, the substrate material is copper with constant thermal conductivity, k_s = 401 W/mK, with a substrate thickness of 650 μm. The substrate base is divided into two regions with each being assigned with a constant heat flux. For Case 1, the background heat flux is set as 85W/cm^2 with a hot spot of 90W/cm^2. For Case 2, the background heat flux is set as 85W/cm^2 with a hot spot of 400W/cm^2. A residual of 10^{-6} is set as the convergence criteria for continuity equation, x-velocity, y-velocity, z-velocity and energy.

6.1.2.2. Coupled Equivalent Circuit Model

Details of circuit setup, hydraulic resistance calculation equations, equivalent circuit thermal model and assumptions are the same as described in Chapter 4. Besides, in order to improve the prediction accuracy and be consistent with the longer pitch geometry, the arrangement of equivalent resistors for channels in larger pitch region is specially treated. As shown in Figure 6-4, due to the larger fin length, the joint of secondary channels are no longer coincident as

for small fin length. Thus the main channel is divided into two sections by the joint point of secondary channel. To be consistent with such geometry, the equivalent circuit is slightly modified by separating the resistor for the main channel into two resistors connected by a node, which also connects to the corresponding branch of secondary channel.

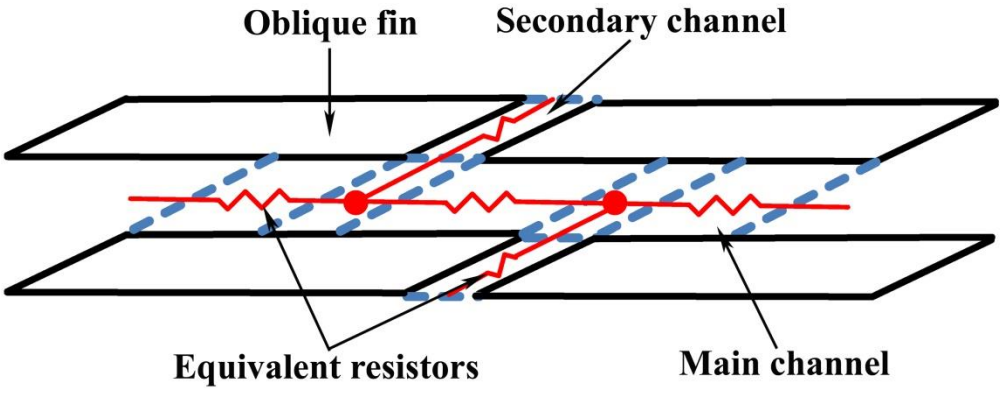

Figure 6-4 Schematic of flow paths of longer pitch oblique-finned system and its reduced circuit

6.1.3. Results and Discussion

The mass flow rate distribution in different main channels along the spanwise direction at different streamwise position is first compared between the results of CFD model and equivalent circuit model. The comparison of average fluid temperature for the two different cases are then presented and discussed respectively. The average substrate base temperature from CFD model and equivalent circuit model is finally compared.

6.1.3.1. Comparison of Mass Flow Distribution

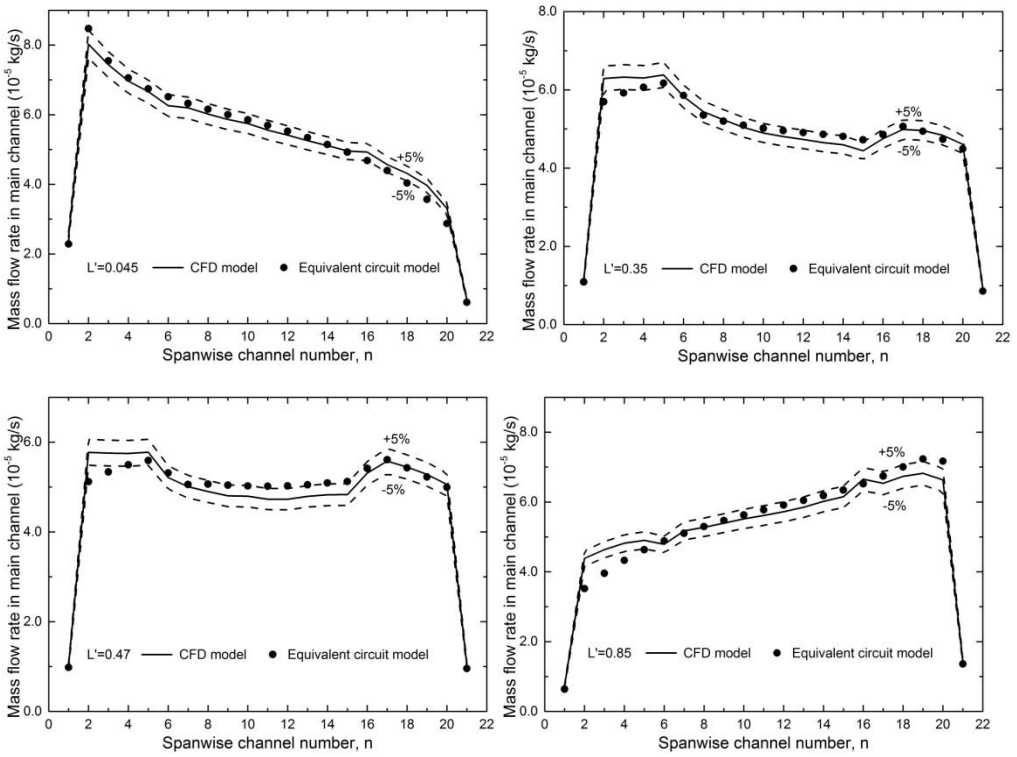

Figure 6-5 Mass flow rate in main channels from CFD model and equivalent circuit model for variable pitch oblique fin microchannel

Figure 6-5 shows the spanwise mass flow rate distribution in main channels at different streamwise positions from CFD model and equivalent circuit model. The comparison shows satisfactory agreement between the results from the two models. At the beginning fin region of L'=0.045 away from the hot spot, the mass flow rate in main channels keeps on reducing from the 2nd channel to the 20th channel along a relatively smooth oblique line. When the fluid flows downstream to L'=0.35 where dense oblique fin is positioned at the center region, the variation of mass flow rate in spanwise direction experiences fluctuations. Relatively lower mass flow rate in main channels is observed in

the dense oblique fin region. Similar fluctuations also turns up in the mass flow rate distribution in main channels at L'=0.47. The lower mass flow rate in main channels indicates a relatively higher percentage of secondary mass flow, which could leads to a more efficient heat removal capacity. As the fluid leaves the dense oblique fin region, the variation of mass flow distribution in spanwise direction returns to an oblique line trend. All these changes are accurately captured by the reduced equivalent circuit flow model precisely.

6.1.3.2. Comparison of Average Fluid Temperature Distribution

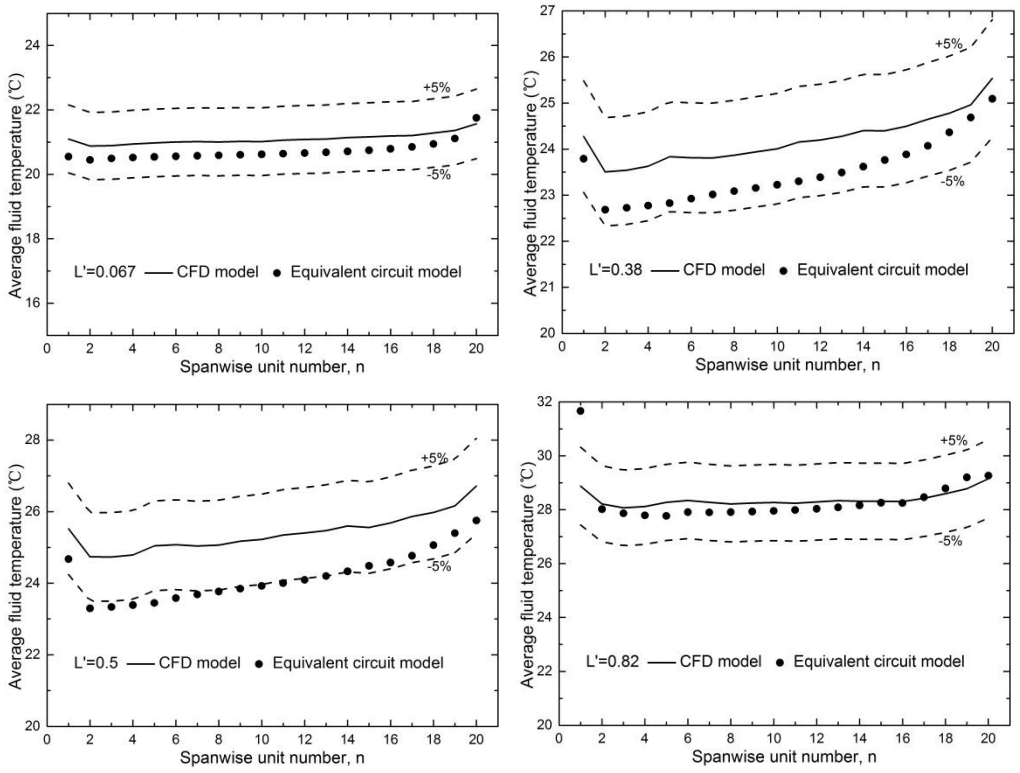

Figure 6-6 Comparison of average fluid temperature for Case 1

Figure 6-6 shows the comparison of average fluid temperature obtained from CFD model and equivalent circuit model for Case 1. Due to exist of hot spot,

the fluid temperature at L'=0.38 and L'=0.5 presents slight fluctuations at the center corresponding to the position of dense oblique fin cluster. The deviation of results from equivalent circuit model and CFD model is mostly within ±5%. Smaller deviation exists in the prediction of average fluid temperature in the upstream and downstream regions. At the center region where hot spot positions, relatively high deviation occurs due to the neglect of heat conduction from the hot spot to its surrounding solid area.

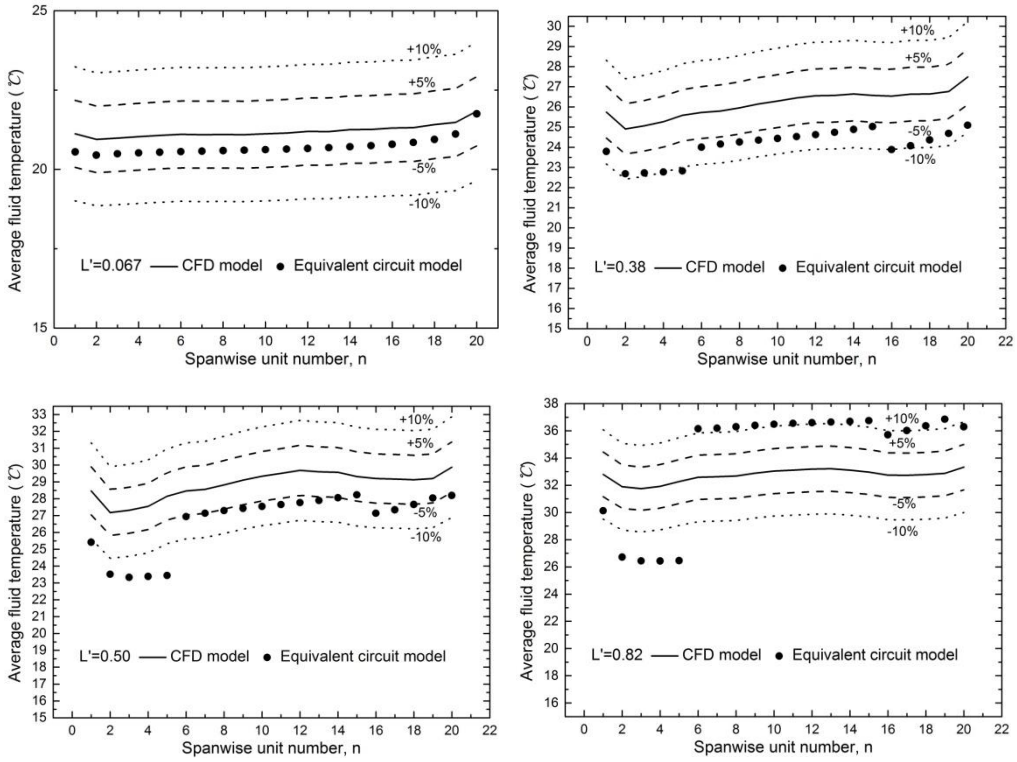

Figure 6-7 Comparison of average fluid temperature for Case 2

Figure 6-7 shows the comparison of average fluid temperature obtained from CFD model and equivalent circuit model for Case 2 with the heat flux imposed on the hot spot being as high as 400W/cm^2. The prediction of average fluid temperature at the position of L'=0.067 shows high accuracy compared

to the results from CFD model. However, due to the extremely high heat flux at hot spot, the effect of heat conduction from the hot spot to its surrounding solid area becomes significant, which leads to a relatively higher deviation in the prediction from equivalent circuit model as it ignores the heat conduction between units. From the results of CFD model at the position of L'=0.38 and 0.50, the fluid temperature at the dense oblique fin region is only slightly higher than the rest regions compared to the extremely high heat flux imposed on the substrate base of hot spot. The significant heat conduction could be attributed to the high thermal conductivity of copper and large difference of heat flux imposed. Therefore the assumption of no heat conduction between oblique units starts to be invalidated in this case. Thus the calculation of heat spreading in the substrate should be incorporated to increase the accuracy of the reduced equivalent circuit thermal model. This could be achieved by connecting the equivalent circuit for the oblique unit by resistors representing conductive thermal resistance between the units.

6.1.3.3. Comparison of Average Substrate Base Temperature Distribution

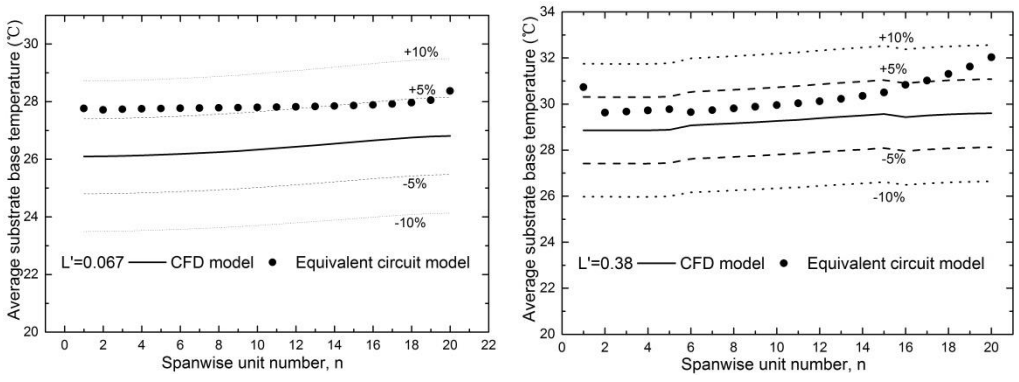

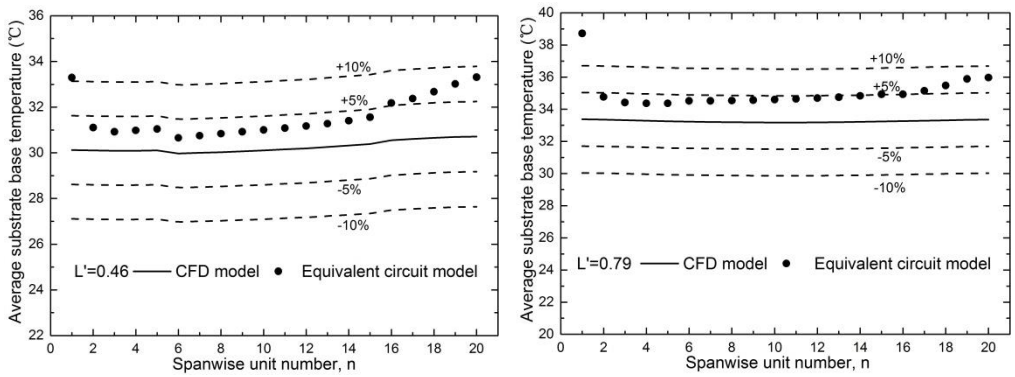

Figure 6-8 Comparison of average substrate base temperature for Case 1

Comparison of average substrate base temperature for Case 1 is showed in Figure 6-8. More than half of the deviation between the results from CFD model and equivalent circuit model falls within the range of ±5% and the rest falls with the range of ±10%. At the position of L'=0.46, the substrate base temperature from the CFD model shows slightly lower at the center than that of its surroundings due to the high heat removal capacity of dense oblique fin cluster. The same fluctuation trend is also observed in the results from the equivalent circuit model. Thus, for the variable pitch oblique fin microchannel heat sink with relatively small heat flux difference imposed, the coupled equivalent circuit model is still able to capture the temperature distribution on the substrate base of high accuracy.

Due to the relatively large deviation in the prediction of average fluid temperature for Case 2, the average substrate base temperature from the equivalent circuit thermal model, which is calculated from the average fluid temperature, is predestined to show a large deviation from the results from

CFD model, thus will not be further discussed in present study.

6.2. Novel Spiral Microchannel Heat Sink with Curved Cuts

6.2.1. Introduction

Compared to conventional straight fin channels, the boundary layer development in spiral channels are more complicated, causing skewed velocity profile and skewed temperature profile. The reason for this is the presence of secondary flows due to centrifugal forces that significantly affect heat and mass transport, as shown in Figure 6-9. In-plane spiral channels have been widely implemented in engineering application due to their higher heat transfer performance, compact structure, and ease of manufacture. However, this complicated fluid flow also results in the large overall pressure drop penalty.

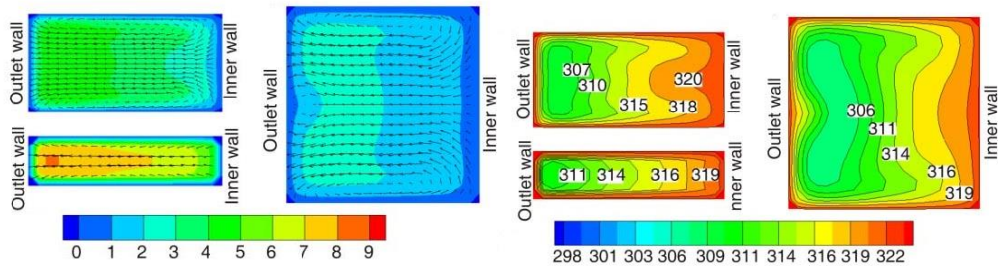

Figure 6-9 Axial velocity and temperature profile of air flow in in-plane spiral with rectangular cross-sections [79]

A novel spiral microchannel heat sink with curved cuts was proposed to fit over circular heat sources, as shown in Figure 6-10. With water entering from the centre of the circular base, the main channels are designed to be spiral,

which involves spiral flows to enhance heat transfer performance and also facilitates the outlet design as compared to the rectangular fins design. Curved cuts are generated along the spiral fins to create smaller secondary channels which are radial curves, as observed from the top of the heat sink. The curved flows shorten the flow path for part of the fluid obviously, and therefore reduce the overall pressure drop. Furthermore, the presence of curved cuts disrupts and reinitializes the thermal boundary layer development, enhances the fluid mixing and increase the effective heat transfer area, which would compensate for the heat transfer penalty due to the reduction of mass flow rate through each spiral channel.

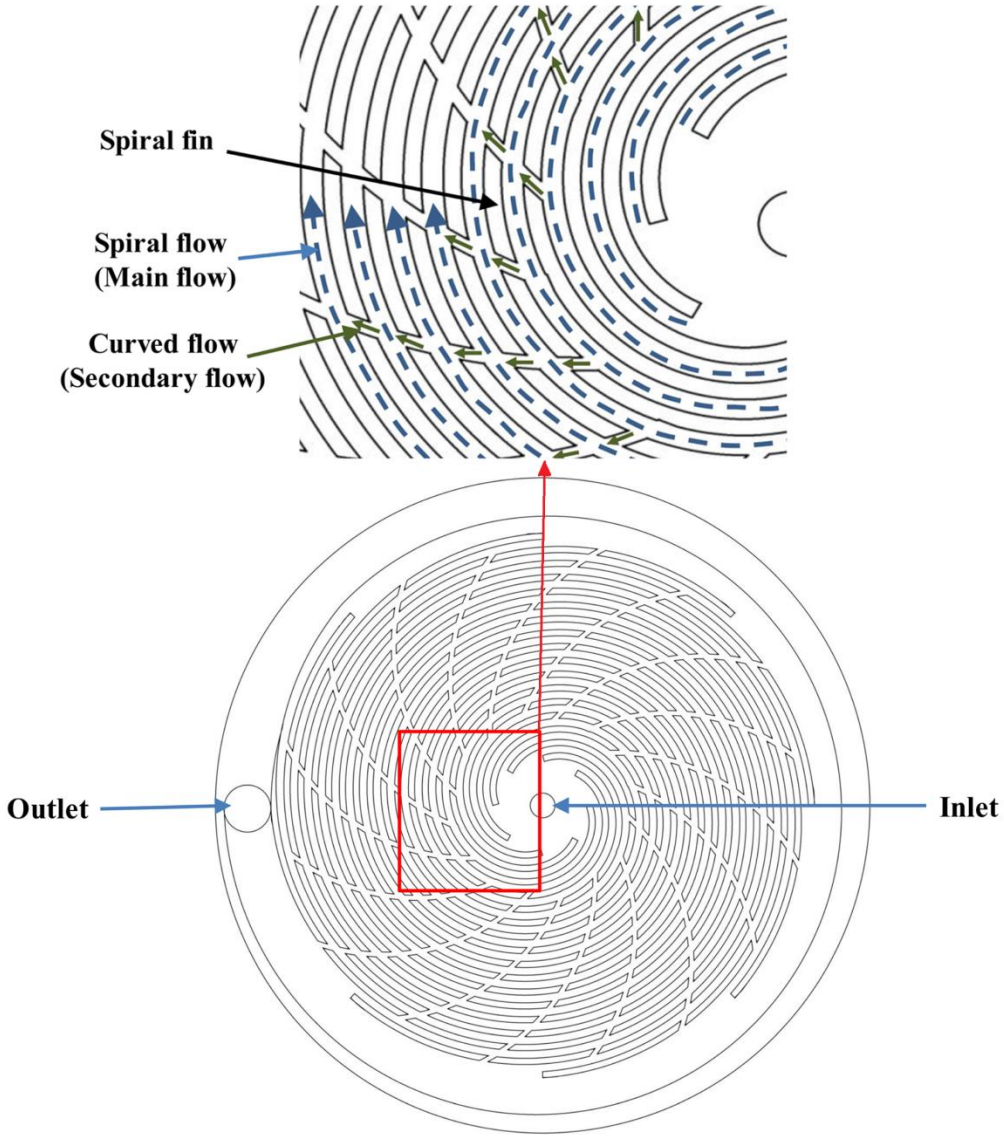

Figure 6-10 2D view of novel spiral microchannel heat sink with curved cuts

Meanwhile, due to the position of outlet, the introduction of curved cuts caused a non-uniform mass flow distribution across the fluid domain, which leads to a non-uniform temperature distribution on the same circumference. Especially for the channels near the outlet, the fluid tries to shorten the path to the outlet so that it disobeys the designed spiral flow direction and travels in reverse direction, resulting in the emergence of dead zones. Along with the

dissymmetry arrangement, it is scarcely possible to build a simplified domain for the numerical simulation of novel spiral mini/microchannel heat sink with curved cuts. Thus, it is of great significance to examine the applicability of coupled equivalent circuit model on the novel spiral mini/microchannel heat sink with curved cuts. Considering the complexity of the geometry, the reduced equivalent circuit flow model is first examined.

6.2.2. Methodologies

6.2.2.1. Numerical Simulation Methodology

A numerical 3D conjugate heat transfer simulation is carried out with considerations on both heat convection in the channel and conduction in the copper substrate. In present study, the following assumptions are made in modeling the heat transfer in microchannel in order to simplify the analysis: (1) steady fluid flow and heat transfer, (2) incompressible fluid, (3) negligible radiation heat transfer from the microchannel heat sink to the surroundings, (4) constant solid and fluid properties. The SST model described in Chapter 3 is adopted in this study.

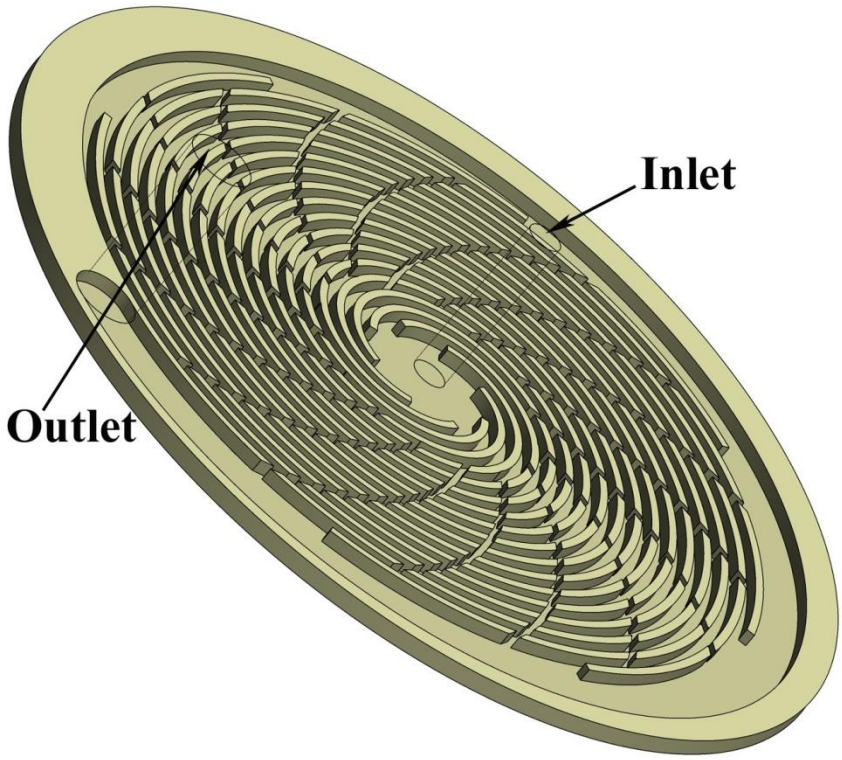

Figure 6-11 Computation domain for novel spiral microchannel heat sink with 16 curved cuts

Figure 6-11illustrates the 3D view of the computation domains for novel spiral microchannel heat sinks with 16 curved cuts. The geometry details of the spiral microchannel heat sink are presented inTable 6-2.

Table 6-2 Dimension details of novel spiral microchannel heat sink simulation models

Characteristic	16 curved cuts
Fluid	Water-liquid(h_2o<l>)
Material	Copper
Footprint diameter D_f,(mm)	53
Inlet diameter D_i,(mm)	2
Outlet diameter D_o,(mm)	3.8
Channel Depth H,(mm)	0.8

Fin width W_f,(mm)	0.5
Spiral channel width W_s, (mm)	0.625
Secondary channel width W_b, (mm)	0.5

The entire computational domain was meshed with max edge size of 0.08 mm and a total number of 57,358,065 cells were generated for the domain. Different grids have been tested, with different max sizes and different first layer thicknesses. Simulations with different grids show satisfactory grid independence for the results obtained with this mesh. The resultant average Nusselt numbers from different meshes used were in close proximity to each other. The resultant average Nusselt numbers from different meshes used were in close proximity to each other. For instance, Nu_{ave} of 6.35, 5.88 and 5.61 were obtained with the mesh counts of 43,523,967; 48,376,498 and 57,358,065 cells respectively. The variations in Nu_{ave} were 7.4% from the coarse to the medium mesh, and 4.5% from the medium to the fine grid. Therefore, the fine grid (57,358,065 cells) was selected in order to preserve both accuracy and cost.

Boundary conditions for the numerical simulation include the no–slip and impermeability conditions on all solid boundaries. The mass flow rate of 0.003kg/s was applied at the inlet and pressure outlet condition was prescribed at the outlet. A residual of 1×10^{-6} is set as the convergence criteria (Root Mean Square) based on the variations of the scaled residuals of the governing

equation for each simulation.

6.2.2.2. Reduced Equivalent Circuit Flow Model

For the spiral minichannel, the hydraulic diameter can be defined as:

$$D_h = \frac{4 \times W_s \times H}{2 \times (W_s + H)} \tag{6-1}$$

Where W_s is the width of the spiral channel and H is the channel depth. Thus, the Reynolds number in this work is defined by

$$\mathrm{Re} = \frac{\rho V D_h}{\mu} \tag{6-2}$$

where ρ is the fluid density, V is the average fluid velocity at A_{eq} and μ represents the fluid viscosity. The friction factor is defined as

$$f = \frac{\Delta P}{\frac{1}{2}\rho V^2 \frac{L}{D_h}} \tag{6-3}$$

where L is the average length of the inner wall and the outer wall for the spiral main channel. Details of circuit setup and hydraulic resistance calculation equations are the same as described in Chapter 4.

6.2.3. Results and Discussion

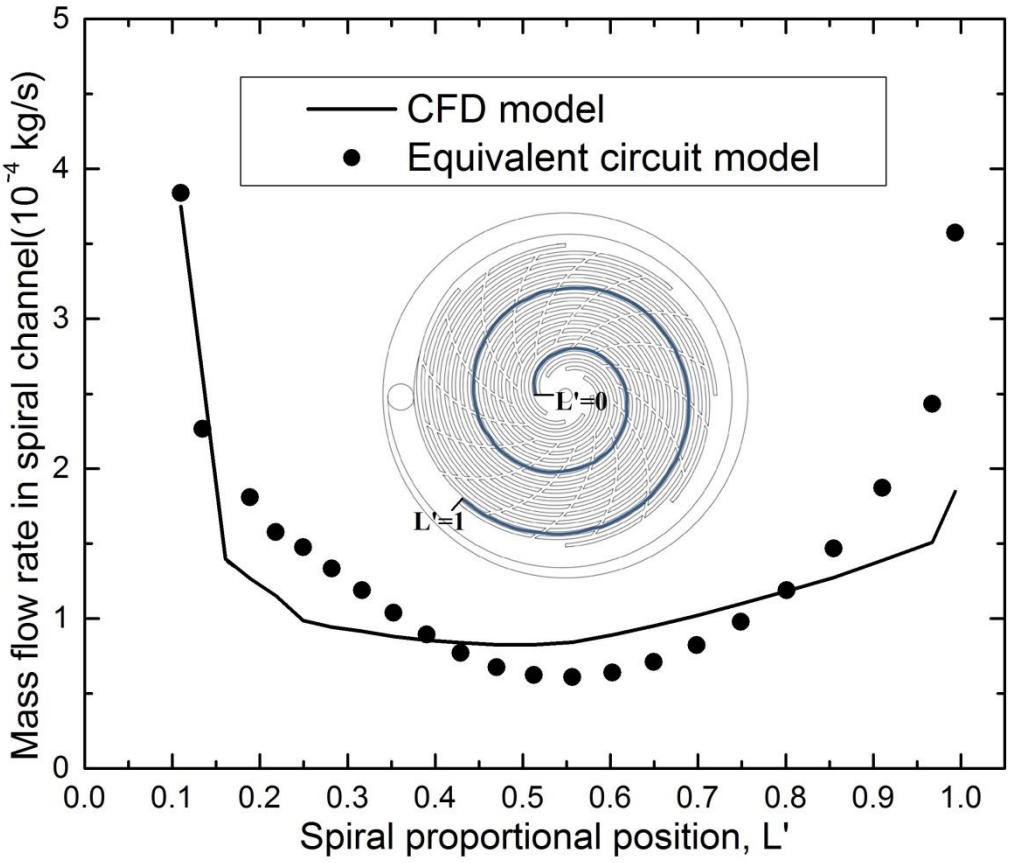

Figure 6-12 Comparison of mass flow rate in spiral main channels along the same spiral line

As shown in Figure 6-12, the mass flow rate in the spiral main channel at L'=0.1 is about 0.000375kg/s, which takes about 1/8 of the total inlet mass flow rate. It thus appears that the position of the outlet and the introduction of curved cuts show negligible effects on the flow distribution at the beginning of the fin region, which is quite different from the situation observed in planar oblique fin microchannel heat sink. As the fluid leaves the first spiral main channel, the generation of curved secondary flow leads to a sharp decrease in the mass flow rate in spiral main channel. The decrease continues about half of

the spiral flow path. As the destination of the investigated spiral line is quite near to the outlet, its spiral channels at the downstream face an influx of fluid flowing along adjacent spiral lines, leading to partial recovery of the mass flow rate in these spiral channels. The results from the equivalent circuit model shows a consistent variable trend along the spiral flow direction but fail to match the specific numbers with an acceptable deviation. The situation is quite similar to the initial prediction of mass flow distribution in planar oblique fin microchannel arrays when inapposite correlations were used. In the current calculation of hydraulic resistances, pressure difference is considered as the only force inducing the fluid flow while the centrifugal forces significantly affect the mass transport in the spiral channels especially for the inducing of curved secondary flow. However, the agreement of trends for the equivalent circuit model and CFD model and the ability of the former to capture flow migration phenomenon still validate the availability of the reduced equivalent circuit flow model for the novel spiral microchannel heat sink with curved cuts, whose accuracy could be further increased on adopting the effect of centrifugal force.

6.3. Conclusions

The applicability of coupled equivalent circuit model in variable pitch oblique fin microchannel heat sink and novel spiral microchannel heat sink with curved cuts is investigated. Detailed full-domain numerical (CFD) simulations

are performed to serve as benchmarks for the coupled equivalent circuit model. Detailed comparisons between the results of equivalent circuit model and CFD model are performed. The following key conclusions can be drawn from the study:

- The reduced equivalent circuit fluid flow model has been employed to predict the flow distribution in variable pitch oblique fin microchannel heat sink. To be consistent with such geometry, the equivalent circuit is slightly modified by separating the resistor for main channel into two resistors by a node connecting the corresponding branch of the secondary channel. Detailed comparisons between the results of the reduced model and numerical simulation by CFD approach demonstrated that the model can accurately predict the mass flow distribution in the variable pitch oblique fin microchannel heat sink. The deviation from the results of full domain numerical simulation is generally less than ±5%.

- The prediction of average fluid temperature and average substrate base temperature from the reduced equivalent thermal shows satisfactory agreement for the variable pitch oblique fin microchannel heat sink with the background heat flux of 85W/cm^2 and hot spot heat flux of 90W/cm^2. Relatively higher deviation exists in the prediction of average fluid temperature when the heat flux of hot spot is raised to 400 W/cm^2. Thus

the calculation of heat spreading in the substrate should be involved to increase the accuracy of the reduced equivalent circuit thermal model for heat sinks fabricated by materials with high thermal conductivity in all directions with large heat flux difference existing on the substrate base.

- The prediction of mass flow distribution in novel spiral microchannel heat sink with curved cuts fails to match the specific numbers with an acceptable deviation due to the neglect of the centrifugal forces which significantly affect the mass transport in the spiral channels especially for the inducing of curved secondary flow. However, the agreement of trends for the equivalent circuit model and CFD model and the ability of the former to capture flow migration phenomenon still validate the availability of the reduced equivalent circuit flow model for the novel spiral microchannel heat sink with curved cuts, whose accuracy could be further increased on adopting the effect of centrifugal force.

Related Publications:

- N Mou, Y Fan, LW Jin, XX, Kong, Ps Lee, TS Liang, A New Design for Heat Transfer Enhancement Using Curved Cuts, 2012 International Symposium on Refrigeration Technology, Zhu Hai.

CHAPTER 7 CONCLUSIONS AND RECOMMENDATIONS FOR FURURE WORK

A coupled equivalent circuit model, which exploits the electric-hydraulic analogy and electric-thermal analogy, is developed to predict the mass flow distribution and temperature distribution in an oblique fin array used in enhanced heat transfer applications. Full domain numerical investigation and Micro-PIV validation of fluid flow in oblique fin microchannels were conducted. Detailed comparisons between the results of reduced models and numerical simulations were presented to validate the application of reduced models in equal pitch oblique fin microchannel heat sink. In addition, the availability of the reduced models in variable pitch oblique fin microchannel heat sink and novel spiral microchannel heat sink with curved cuts was investigated. Key accomplishments of the present study and recommendations for future work are summarized below.

7.1. Conclusions

(1) The CFD model used in present study is valid and reliable for the novel oblique fin microchannel geometry. The velocity vectors for both geometries obtained from the CFD simulations are highly coincident with the experiment results. The disruption and reinitialization of momentum boundary layer development in the

main channels are also observed by both the microPIV system and the CFD simulation.

(2) The generation of secondary flow is highly dependent on the structural design even if small channels at a certain angle between two main liquid channels are added. Flow will not follow the oblique channel direction when oblique fin microchannel geometry is designed with small fin length to fin pitch ratio, small fin width to main channel width ratio and large oblique angle.

(3) The continuous secondary flow in the same oblique direction leads to an obvious velocity and pressure variation in the spanwise direction in fin region. The flow is re-distributed in the inlet manifold and flow migration occurs within the fin array.

(4) In a majority of the oblique fin region, flow migration does not affect the local coolant velocity significantly. The velocity distribution in most main channels shows no observable difference from each other except for that in the main channels lying near the sidewalls.

(5) A coupled equivalent circuit fluid flow model, which exploits the electric-hydraulic analogy and electric-thermal analogy, has been developed to predict the flow distribution and temperature distribution in planar secondary flow generating oblique fin

configurations.

(6) Separate correlations for friction factors, and therefore hydraulic resistances, in the main and secondary channels have been developed, which appropriately capture the unique features of fluid flow in each. Appropriate Nusselt number correlations and thermal resistance models are also employed to predict the temperature distribution associated with the mass flow distribution obtained from the reduced equivalent circuit fluid flow model.

(7) Detailed comparisons between the results of the coupled equivalent circuit model and numerical simulation by CFD approach demonstrated that the model can accurately predict the mass flow distribution and temperature distribution with the fin number, aspect ratio, fin pitch, fin length, oblique angle and inlet velocity varying within the actual application scope. The deviation from the results of full domain numerical simulation is generally less than $\pm 5\%$.

(8) Slightly higher deviation of temperature prediction is detected in the edge regions, which can be attributed to deviation of mass flow prediction and the assumption of uniform heat flux distribution in the edge regions.

(9) The case studies show that this new model is able to greatly simplify

simulation procedures, shorten the simulation time and post-processing time and reduce the dependence on computer performance.

(10) The reduced equivalent circuit fluid flow model, which is slightly modified by separating the resistor for main channel into two resistors by a node connecting the corresponding branch of the secondary channel, has been employed to predict the flow distribution in variable pitch oblique fin microchannel heat sink. Detailed comparisons between the results of the reduced model and numerical simulation by CFD approach demonstrated that the model can accurately predict the mass flow distribution in the variable pitch oblique fin microchannel heat sink. The deviation from the results of full domain numerical simulation is generally less than ±5%.

(11) The prediction of average fluid temperature and average substrate base temperature from the reduced equivalent thermal shows satisfactory agreement for the variable pitch oblique fin microchannel heat sink with the background heat flux of 85W/cm^2 and hot spot heat flux of 90W/cm^2. Relatively higher deviation exists in the prediction of average fluid temperature when the heat flux of hot spot is raised to 400 W/cm^2. Thus the calculation of heat spreading in the substrate

should be involved to increase the accuracy of the reduced equivalent circuit thermal model for heat sinks fabricated by materials with high thermal conductivity in all directions with large heat flux difference existing on the substrate base.

(12) The prediction of mass flow distribution in novel spiral microchannel heat sink with curved cuts fails to match the specific numbers with an acceptable deviation due to the neglect of the centrifugal forces which significantly affect the mass transport in the spiral channels especially for the inducing of curved secondary flow. However, the agreement of trends for the equivalent circuit model and CFD model and the ability of the former to capture flow migration phenomenon still validate the availability of the reduced equivalent circuit flow model for the novel spiral microchannel heat sink with curved cuts, whose accuracy could be further increased on adopting the effect of centrifugal force.

7.5. Recommendations for Future Work

Encouraged by the achievements of present investigations and validation of the coupled equivalent circuit model, the major extended works for future research are recommended and outlined as follows:

(1) The criterion that defines laminar flow and turbulent flow in oblique fin

configuration is still not clearly stated. As the friction factor of flow in oblique fin configuration is not only a function of Reynolds number but affected by a parameter group defined as (θ, H/w_{ch}, w_{ob}/l_u, $D_h/(w_{ch}+w_w)$, Re_{unit}), the Reynolds number may not be the only criterion for flow pattern either. This study is quite fundamental and necessary. It will fill the basic theory gap of our current research on oblique fin configuration in hydromechanics and heat transfer and also can be extended to similar configurations.

(2) A large vortex was found close to the trail of the oblique fin region for high velocity cases in present study. However, its origin, its influence and the corresponding treatment method is still vacant and need to be clearly stated. Micro-PIV technology can be employed to complement and validate the studies from numerical simulations. Meanwhile, its findings will also help to further improve the coupled equivalent circuit model.

(3) The further optimization of the prediction for flow and temperature on both side edges, and the promoted application of the coupled equivalent circuit model could be conducted. New correlations used for the friction calculation of channels on both side edges could be developed.

(4) The heat spreading model could be developed and added to the equivalent circuit thermal model to increase the temperature prediction for

non-uniform heat flux imposed on the substrate base, especially when large difference in applied heat flux exists.

(5) The model can be further generalized to other coolant and secondary flow generating configurations, and the development of new correlations or modification of current correlations should also be involved, if necessary.

References:

[1] Moore, G.E., 1998, Cramming More Components Onto Integrated Circuits, P Ieee 86, pp. 82-85.

[2] Black, J.R., 1969, Electromigration—A brief survey and some recent results, Electron Devices, IEEE Transactions on 16, pp. 338-347.

[3] Tuckerman, D.B., Pease, R.F.W., 1981, High-performance heat sinking for VLSI, Electron Device Letters, IEEE 2, pp. 126-129.

[4] Cowell, T.A., Heikal, M.R., Achaichia, A., 1995, Flow and heat transfer in compact louvered fin surfaces, Exp Therm Fluid Sci 10, pp. 192-199.

[5] Lee, Y.J., Lee, P.S., Chou, S.K., Enhanced microchannel heat sinks using oblique fins, 2009, ASME.

[6] Fan, Y., Lee, P.S., Jin, L., 2013, A simulation and experimental study of fluid flow and heat transfer on cylindrical oblique-finned heat sink, Int J Heat Mass Tran 61, pp. 62-72.

[7] Lee, Y.J., Lee, P.S., Chou, S.K., 2013, Numerical Study of Fluid Flow and Heat Transfer in the Enhanced Microchannel With Oblique Fins, Journal of Heat Transfer 135, pp. 41901.

[8] http://www.businessweek.com/articles/2013-01-18/why-the-batteries-in-boeings-787-are-burning.

[9] https://en.wikipedia.org/wiki/Integrated_circuit.

[10] Sheng-Chih, L., Banerjee, K., 2008, Cool Chips: Opportunities and Implications for Power and Thermal Management, Electron Devices, IEEE Transactions on 55, pp. 245-255.

[11] Lawless, P.B., 2009, Advanced Aerodynamics for Electronics Cooling Fans, Electronics Cooling Volume 15, pp. 28-29.

[12] Smith, N., High efficiency electronic cooling fans, 2009, Semiconductor Thermal Measurement and Management Symposium, 2009. SEMI-THERM 2009. 25th Annual IEEE, pp. 92-97.

[13] Miyahara, M., 2009, Small Fans for Cooling Small Electronic Devices, Electronics Cooling Volume 15, pp. 30-32.

[14] Belady, C.L., 2007, In the data center, power and cooling costs more than the it equipment it supports, Electronics Cooling Volume 13, pp. 6-9.

[15] Whitenack, K., 2008, Liquid Cooling for Datacom Equipment Centers, Electronic Cooling Volume 14, pp. 28-32.

[16] http://www.techradar.com/news/mobile-computing/laptops/this-is-how-the-world-s-first-liquid-cooled-gaming-laptop-was-made-1310793/1.

[17] Garner, S.D., 1996, Heat Pipes for Electronics Cooling Applications, Electronics Cooling, pp.

[18] Soule, C.A., 2001, Future trends in heat sink design, Electronics Cooling, pp.

[19] Elnaggar, M.H.A., Abdullah, M.Z., Abdul Mujeebu, M., 2012, Characterization of working fluid in vertically mounted finned U-shape twin heat pipe for electronic cooling, Energ Convers Manage 62, pp. 31-39.

[20] Sangchandr, B., Afzulpurkar, V., 2009, A novel approach for cooling electronics using a combined heat pipe and thermoelectric module, J. Eng. Appl. Sci 2, pp. 603-610.

[21] De Volder, M.F., Tawfick, S.H., Baughman, R.H., 2013, Carbon nanotubes: present and future commercial applications, Science 339, pp. 535-539.

[22] Klemens, P.G., Pedraza, D.F., 1994, Thermal conductivity of graphite in the basal plane, Carbon 32, pp. 735-741.

[23] Petroski, J., 2006, Thermal Challenges In LED Cooling, Electronics Cooling, pp.

[24] Weng, C., 2009, Advanced thermal enhancement and management of LED packages, Int Commun Heat Mass 36, pp. 245-248.

[25] http://www.electronicsweekly.com/news/products/led/osram-reveals-best-headlamp-led-yet-2015-09/.

[26] Jen-Hau, C., Chun-Kai, L., Yu-Lin, C., Cooling performance of silicon-based thermoelectric device on high power LED, 2005, Thermoelectrics, 2005. ICT 2005. 24th International Conference on, pp. 53-56.

[27] Jang, D., Yu, S., Lee, K., 2012, Multidisciplinary optimization of a pin-fin radial heat sink for LED lighting applications, Int J Heat Mass Tran 55, pp. 515-521.

[28] Kim, J., Kim, S.J., 2013, Heat transfer characteristics of a centrifugal heat sink, Int J Heat Mass Tran 56, pp. 188-196.

[29] Xiaobing, L., Wei, X., Ting, C., Design and optimization of horizontally-located plate fin heat sink for high power LED street lamps, 2009, Electronic Components and Technology Conference, 2009. ECTC 2009. 59th, pp. 854-859.

[30] Lai, Y., Cordero, N., Barthel, F., 2009, Liquid cooling of bright LEDs for automotive applications, Appl Therm Eng 29, pp. 1239-1244.

[31] XIANG, J., ZHANG, C., JIANG, F., 2011, Fabrication and testing of phase change heat sink for high power LED, T Nonferr Metal Soc 21, pp. 2066-2071.

[32] Lu, X., Hua, T., Wang, Y., 2011, Thermal analysis of high power LED package with heat pipe heat sink, Microelectron J 42, pp. 1257-1262.

[33] Li, J., Lin, F., Wang, D., 2013, A loop-heat-pipe heat sink with parallel condensers for high-power integrated LED chips, Appl Therm Eng 56, pp. 18-26.

[34] Lin, Z., Wang, S., Huo, J., 2011, Heat transfer characteristics and LED heat sink application of aluminum plate oscillating heat pipes, Appl Therm Eng 31, pp. 2221-2229.

[35] http://web.archive.org/web/20110309140814/http://www.rise.org.au/info/Tech/lowtemp/hotwatersys.html.

[36] Ekramian, E., Etemad, S.G., Haghshenasfard, M., 2014, Numerical Analysis of Heat Transfer Performance of Flat Plate Solar Collectors, Journal of Fluid Flow, Heat and Mass Transfer Vol. 1, pp. 38-42.

[37] Minardi, J.E., Chuang, H.N., 1975, Performance of a “black” liquid flat-plate solar collector, Sol Energy 17, pp. 179-183.

[38] J. Trentleman, P.H.W., 1977, Performance analysis of a black liquid absorbing collector (BLAC), Proc. Ann. Mtg. Am. Section Int. Solar Energy Soc. (61st edition) 1, pp. 21-25.

[39] R. S. Daryan, P.K.C.P., 1978, A black liquid flat plate collector for economical applications.

[40] B. J. Huang, T.Y.W.S., 1979, Thermal analysis of a black liquid cylindrical parabolic collector, Sol Energy 22, pp. 221.

[41] Camera-Roda, G., Bertel à, M., 1988, A model of black-liquid solar collector, Sol Energy 40, pp. 197-209.

[42] Abdelrahman, M., Fumeaux, P., Suter, P., 1979, Study of solid-gas-suspensions used for direct absorption of concentrated solar radiation, Sol Energy 22, pp. 45-48.

[43] Otanicar, T.P., Phelan, P.E., Golden, J.S., 2009, Optical properties of liquids for direct absorption solar thermal energy systems, Sol Energy 83, pp. 969-977.

[44] Otanicar, T.P., Phelan, P.E., Prasher, R.S., 2010, Nanofluid-based direct absorption solar collector, Journal of Renewable and Sustainable Energy 2, pp. 33102.

[45] Sharp, K.V., Adrian, R.J., Beebe, D.J., 2000, Anomalous transition to turbulence in microtubes,Proceedings of Int. Mech. Eng. Cong. Expo., 5th Micro-Fluidic Symp., pp. 150-158.

[46] Xu, B., Ooti, K.T., Wong, N.T., 2000, Experimental investigation of flow friction for liquid flow in microchannels, Int Commun Heat Mass 27, pp. 1165-1176.

[47] Ding, L.S., Sun, H., Sheng, X.L., 2000, Measurement of friction factors for R134a and R12 through microchannels,Proceedings of Symposium on Energy Engrg. in the 21st Century, pp. 650-657.

[48] Araki, T., Soo, K.M., Hiroshi, I., 2000, An experimental investigation of gaseous flow characteristics in microchannels, in: Microscale, I.C.O.H.(Ed.),Proceedings of International Conference on Heat Transfer and Transport Phenomena in Microscale, pp. 155-161.

[49] Judy, J., Maynes, D., Webb, B.W., 2000, Liquid flow pressure drop in microtubes, in: Celata, G.P.(Ed.)pp. 149-154.

[50] Yang, C.J., Park, E.B., Hwang, Y.S., 2000, The effect of Co on the enhanced magnetic properties of Fe3B/Nd2Fe14B magnets, J Magn Magn Mater 212, pp. 168-174.

[51] Gao, P., Le Person, S., Favre-Marinet, M., 2002, Scale effects on hydrodynamics and heat transfer in two-dimensional mini and microchannels, Int J Therm Sci 41, pp. 1017-1027.

[52] Mokrani, O., Bourouga, B., Castelain, C., 2009, Fluid flow and convective heat transfer in flat microchannels, Int J Heat Mass Tran 52, pp. 1337-1352.

[53] Harms, T.M., Kazmierczak, M.J., Gerner, F.M., 1999, Developing convective heat transfer in deep rectangular microchannels, Int J Heat Fluid Fl 20, pp. 149-157.

[54] Warrier, G.R., Dhir, V.K., Momoda, L.A., 2002, Heat transfer and pressure drop in narrow rectangular channels, Exp Therm Fluid Sci 26, pp. 53-64.

[55] Tso, C.P., Mahulikar, S.P., 2000, Experimental verification of the role of Brinkman number in microchannels using local parameters, Int J Heat Mass Tran 43, pp. 1837-1849.

[56] Rahman, M.M., 2000, Measurements of heat transfer in microchannel heat sinks, Int Commun Heat Mass 27, pp. 495-506.

[57] Morini, G.L., 2004, Single-phase convective heat transfer in microchannels: a review of experimental results, Int J Therm Sci 43, pp. 631-651.

[58] Li, J., Peterson, G.P., 2007, 3-Dimensional numerical optimization of silicon-based high performance parallel microchannel heat sink with liquid flow, Int J Heat Mass Tran 50, pp. 2895-2904.

[59] Ryu, J.H., Choi, D.H., Kim, S.J., 2002, Numerical optimization of the thermal performance of a microchannel heat sink, Int J Heat Mass Tran 45, pp. 2823-2827.

[60] Liu, D., Garimella, S.V., 2005, Analysis and optimization of the thermal performance of microchannel heat sinks, Int J Numer Method H 15, pp. 7-26.

[61] Lee, P.S., Chou, S.K., Lee, Y.J., Optimization of the Thermal Performance of Microchannel Heat Sinks Using Thermally Developing Nusselt Number Correlation, 2008, Electronics Packaging Technology Conference, 2008. EPTC 2008. 10th, IEEE, Singapore, pp. 545-551.

[62] Lee, P.S., Garimella, S.V., 2006, Thermally developing flow and heat transfer in rectangular microchannels of different aspect ratios, Int J Heat Mass Tran 49, pp. 3060-3067.

[63] Lee, P.S., Garimella, S.V., Liu, D., 2005, Investigation of heat transfer in rectangular

microchannels, Int J Heat Mass Tran 48, pp. 1688-1704.

[64] Steinke, M.E., Kandlikar, S.G., 2006, Single-phase liquid friction factors in microchannels, Int J Therm Sci 45, pp. 1073-1083.

[65] Hewitt, G., Shires, G., Polezhaev, Y., International Encyclopedia of Heat and Mass Transfer, 1997, CRC Press, New York.

[66] Naphon, P., Wongwises, S., 2006, A review of flow and heat transfer characteristics in curved tubes, Renewable and sustainable energy reviews 10, pp. 463-490.

[67] Acharya, N., Sen, M., Chang, H., 2001, Analysis of heat transfer enhancement in coiled-tube heat exchangers, Int J Heat Mass Tran 44, pp. 3189-3199.

[68] Chen, H., Zhang, B., 2003, Fluid flow and mixed convection heat transfer in a rotating curved pipe, Int J Therm Sci 42, pp. 1047-1059.

[69] Garimella, S., Richards, D.E., Christensen, R.N., 1988, Experimental Investigation of Heat Transfer in Coiled Annular Ducts, Journal of Heat Transfer 110, pp. 329-336.

[70] Ko, T.H., 2006, Thermodynamic analysis of optimal mass flow rate for fully developed laminar forced convection in a helical coiled tube based on minimal entropy generation principle, Energ Convers Manage 47, pp. 3094-3104.

[71] Dean, W.R., 1927, XVI. Note on the motion of fluid in a curved pipe, The London, Edinburgh, and Dublin Philosophical Magazine and Journal of Science 4, pp. 208-223.

[72] Dean, W.R., 1928, LXXII. The stream-line motion of fluid in a curved pipe (Second paper), The London, Edinburgh, and Dublin Philosophical Magazine and Journal of Science 5, pp. 673-695.

[73] Mori, Y., Uchida, Y., Ukon, T., 1971, Forced convective heat transfer in a curved channel with a square cross section, Int J Heat Mass Tran 14, pp. 1787-1805.

[74] Kalb, C.E., Seader, J.D., 1972, Heat and mass transfer phenomena for viscous flow in curved circular tubes, Int J Heat Mass Tran 15, pp. 801-817.

[75] Goering, D.J., Humphrey, J., Greif, R., 1997, The dual influence of curvature and buoyancy in fully developed tube flows, Int J Heat Mass Tran 40, pp. 2187-2199.

[76] Naphon, P., Suwagrai, J., 2007, Effect of curvature ratios on the heat transfer and flow developments in the horizontal spirally coiled tubes, Int J Heat Mass Tran 50, pp. 444-451.

[77] Bai, B., Guo, L., Feng, Z., 1999, Turbulent heat transfer in a horizontal helically coiled tube, Heat Transfer-Asian Research 28, pp. 395-403.

[78] Yoo, G., Choi, H., Dong, W., 2012, Fluid flow and heat transfer characteristics of spiral coiled tube: Effects of Reynolds number and curvature ratio, Journal of Central South University 19, pp. 471-476.

[79] Kurnia, J.C., Sasmito, A.P., Mujumdar, A.S., 2012, Laminar convective heat transfer for in-plane spiral coils of noncircular cross sections ducts: A computational fluid dynamics study, Thermal science 16, pp. 109-118.

[80] Gyves, T.W., Irvine Jr., T.F., 2000, Laminar conjugated forced convection heat transfer in curved rectangular channels, Int J Heat Mass Tran 43, pp. 3953-3964.

[81] Egner, M.W., Burmeister, L.C., 2005, Heat Transfer for Laminar Flow in Spiral Ducts of Rectangular Cross Section, Journal of Heat Transfer 127, pp. 352-356.

[82] Hashemi, S.M., Akhavan-Behabadi, M.A., 2012, An empirical study on heat transfer and pressure drop characteristics of CuO – base oil nanofluid flow in a horizontal helically coiled tube under constant heat flux, Int Commun Heat Mass 39, pp. 144-151.

[83] Ghobadi, M., Muzychka, Y.S., 2015, Heat transfer and pressure drop in a spiral square channel,

Exp Heat Transfer 28, pp. 546-563.

[84] Steinke, M.E., Kandlikar, S.G., Single-phase heat transfer enhancement techniques in microchannel and minichannel flows, 2004, Second International Conference on Microchannels and Minichannels, NY, pp. 17-19.

[85] Webb, R.L., Narayanamurthy, R., Thors, P., 1999, Heat Transfer and Friction Characteristics of Internal Helical-Rib Roughness, Journal of Heat Transfer 122, pp. 134-142.

[86] Kidd, G.J., 1969, Heat transfer and pressure drop for nitrogen flowing in tubes containing twisted tapes, Aiche J 15, pp. 581-585.

[87] Manglik, R.M., Bergles, A.E., 1993, Heat Transfer and Pressure Drop Correlations for Twisted-Tape Inserts in Isothermal Tubes: Part II—Transition and Turbulent Flows, Journal of Heat Transfer 115, pp. 890-896.

[88] Biswas, G., Mitra, N.K., Fiebig, M., 1994, Heat transfer enhancement in fin-tube heat exchangers by winglet type vortex generators, Int J Heat Mass Tran 37, pp. 283-291.

[89] Li, H., Chen, C., Chao, S., 2013, Enhancing heat transfer in a plate-fin heat sink using delta winglet vortex generators, Int J Heat Mass Tran 67, pp. 666-677.

[90] Yang, K., Jhong, J., Lin, Y., 2010, On the heat transfer characteristics of heat sinks: with and without vortex generators, Components and Packaging Technologies, IEEE Transactions on 33, pp. 391-397.

[91] Ahmed, H.E., Mohammed, H.A., Yusoff, M.Z., 2012, An overview on heat transfer augmentation using vortex generators and nanofluids: approaches and applications, Renewable and Sustainable Energy Reviews 16, pp. 5951-5993.

[92] Kays, W.M., London, A.L., 1984, Compact Heat Exchangers, 3rd Edition ed., McGraw-Hill, New York,pp.

[93] Tatsumi, K., Yamaguchi, M., Nishio, Y., Heat Transfer and Pressure Loss Characteristics of Obliquely-Arranged Cut-Fins, 2006, International Heat Transfer Conference 13, Begel House Inc..

[94] Ko, T.H., 2006, A numerical study on entropy generation and optimization for laminar forced convection in a rectangular curved duct with longitudinal ribs, Int J Therm Sci 45, pp. 1113-1125.

[95] Chang, S.W., Chiang, K.F., Kao, J.K., 2011, Heat transfer and pressure drop in a square spiral channel roughened by in-line skew ribs, Int J Heat Mass Tran 54, pp. 3167-3178.

[96] Yu, S., Lee, K., Yook, S., 2010, Natural convection around a radial heat sink, Int J Heat Mass Tran 53, pp. 2935-2938.

[97] Jang, D., Yu, S., Lee, K., 2012, Multidisciplinary optimization of a pin-fin radial heat sink for LED lighting applications, Int J Heat Mass Tran 55, pp. 515-521.

[98] Sparrow, E.M., Vemuri, S.B., 1986, Orientation effects on natural convection/radiation heat transfer from pin-fin arrays, Int J Heat Mass Tran 29, pp. 359-368.

[99] Zografos, A.I., Edward Sunderland, J., 1990, Natural convection from pin fin arrays, Exp Therm Fluid Sci 3, pp. 440-449.

[100] Peles, Y., Koşar, A., Mishra, C., 2005, Forced convective heat transfer across a pin fin micro heat sink, Int J Heat Mass Tran 48, pp. 3615-3627.

[101] Zhimin, W., Joshi, Y., Pressure drop and heat transfer characteristics of square pin fin enhanced microgaps in single phase microfluidic cooling, 2014, Thermal and Thermomechanical Phenomena in Electronic Systems (ITherm), 2014 IEEE Intersociety Conference on, pp. 649-657.

[102] Springer, M.E., Thole, K.A., 1998, Experimental design for flowfield studies of louvered fins, Exp Therm Fluid Sci 18, pp. 258-269.

[103] DeJong, N.C., Jacobi, A.M., 2003, Flow, heat transfer, and pressure drop in the near-wall region of louvered-fin arrays, Exp Therm Fluid Sci 27, pp. 237-250.
[104] Springer, M.E., Thole, K.A., 1999, Entry region of louvered fin heat exchangers, Exp Therm Fluid Sci 19, pp. 223-232.
[105] Perrotin, T., Clodic, D., 2004, Thermal-hydraulic CFD study in louvered fin-and-flat-tube heat exchangers, International Journal of Refrigeration 27, pp. 422-432.
[106] Webb, R.L., Trauger, P., 1991, How structure in the louvered fin heat exchanger geometry, Exp Therm Fluid Sci 4, pp. 205-217.
[107] Fan, Y., Lee, P.S., Jin, L., 2014, A parametric investigation of heat transfer and friction characteristics in cylindrical oblique fin minichannel heat sink, Int J Heat Mass Tran 68, pp. 567-584.
[108] Fan, Y., Lee, P.S., Chua, B.W., 2014, Investigation on the influence of edge effect on flow and temperature uniformities in cylindrical oblique-finned minichannel array, Int J Heat Mass Tran 70, pp. 651-663.
[109] Firestone, F.A., 1933, A NEW ANALOGY BETWEEN MECHANICAL AND ELECTRICAL SYSTEMS, The Journal of the Acoustical Society of America 4, pp. 249-267.
[110] Brask, A., Goranović, G., Bruus, H., 2003, Theoretical analysis of the low-voltage cascade electro-osmotic pump, Sensors and Actuators B: Chemical 92, pp. 127-132.
[111] Takamura, Y., Onoda, H., Inokuchi, H., 2003, Low-voltage electroosmosis pump for stand-alone microfluidics devices, Electrophoresis 24, pp. 185-192.
[112] Tao, W.Q., Ti, H.C., 1998, Transient analysis of gas pipeline network, Chem Eng J 69, pp. 47-52.
[113] Ke, S.L., Ti, H.C., 2000, Transient analysis of isothermal gas flow in pipeline network, Chem Eng J 76, pp. 169-177.
[114] Taherinejad, M., Hosseinalipoor, S.M., Madoliat, R., 2014, STEADY FLOW ANALYSIS AND MODELING OF THE GAS DISTRIBUTION NETWORK USING THE ELECTRICAL ANALOGY (RESEARCH NOTE), International Journal of Engineering-Transactions B: Applications 27, pp. 1269.
[115] Bruus, H., Theoretical Microfluidics. Oxford Master Series in Condensed Matter Physics, 2008, Oxford University Press Oxford.
[116] Lee, S., 1998, Calculating Spreading Resistance in Heat Sinks, Electronics Cooling, pp.
[117] Muzychka, Y.S., Culham, J.R., Yovanovich, M.M., 2003, Thermal spreading resistance of eccentric heat sources on rectangular flux channels, J Electron Packaging 125, pp. 178-185.
[118] Culham, J.R., Khan, W.A., Yovanovich, M.M., 2007, The influence of material properties and spreading resistance in the thermal design of plate fin heat sinks, J Electron Packaging 129, pp. 76-81.
[119] Guenin, B., Heat Spreading Calculations using thermal circuit elements, 2008, Electronics Cooling, pp. 8-12.
[120] Simons, R.E., Estimating Parallel Plate-Fin Heat Sink Thermal Resistance, 2003.
[121] Kang, H., 2012, Evaluation of Fin Efficiency and Heat Transfer Coefficient for Fined Tube Heat Exchange, pp.
[122] Kabir, H., Ortega, A., A new model for substrate heat spreading to two convective heat sinks: Application to the BGA package, 1998, Semiconductor Thermal Measurement and Management Symposium, 1998. SEMI-THERM Proceedings 1998., Fourteenth Annual IEEE, pp. 24-30.
[123] Simons, R.E., 2005, Using an Equivalent Heat Transfer Coefficient to Model Fins on a Fin,

Electronics Cooling, pp.
[124] Drofenik, U., Kolar, J.W., 2006, A thermal model of a forced-cooled heat sink for transient temperature calculations employing a circuit simulator, IEEJ Transactions on Industry Applications 126, pp. 841-851.
[125] Lévêque, A., 1928, Les lois de la transmission de chaleur par
convection, Ann. Mines 13, pp. 201-415.
[126] Martin, H., 1996, A theoretical approach to predict the performance of chevron-type plate heat exchangers, Chemical Engineering and Processing: Process Intensification 35, pp. 301-310.
[127] Kumar Das, S., Nanda, P., 2000, Use of artificial neural network and leveque analogy for the exergy analysis of regenerator beds, Chemical Engineering and Processing: Process Intensification 39, pp. 113-120.
[128] Martin, H., 2002, The Generalized Leveque Equation (GLE) and its use to predict heat and mass transfer from fluid friction, HEAT TRANSFER 3, pp. 135-140.
[129] Martin, H., 2002, The generalized Lévêque equation and its practical use for the prediction of heat and mass transfer rates from pressure drop, Chem Eng Sci 57, pp. 3217-3223.
[130] Badarinath, K., Balaji, D.S., Prasad, C., 2006, Application of Leveque Analogy to Offset Strip-Fin Surfaces for Prediction of Heat Transfer Characteristics, INTERNATIONAL JOURNAL OF HEAT EXCHANGERS 7, pp. 75.
[131] Hofmann, R., Frasz, F., Ponweiser, K., 2007, Heat transfer and pressure drop performance comparison of finned-tube bundles in forced convection, WSEAS Trans. Heat Mass Transfer 2, pp. 72-88.
[132] Dietrich, B., Kind, M., Martin, H., The Le´ve ˆque Analogy: Does it Work for Solid Ceramic Sponges Too? 2010, 2010 14th International Heat Transfer Conference, American Society of Mechanical Engineers, pp. 829-835.
[133] J., B., P., H., T., C., 1997, Turbulence modeling validation, American Institute of Aeronautics and Astronautics.
[134] Lee, Y.J., Lee, P.S., Chou, S.K., 2012, Enhanced Thermal Transport in Microchannel Using Oblique Fins, Journal of Heat Transfer 134, pp. 101901.
[135] Adrian, R.J., 1991, Particle-imaging techniques for experimental fluid mechanics, Annu Rev Fluid Mech 23, pp. 261-304.
[136] Meinhart, C.D., Prasad, A.K., Adrian, R.J., 1993, A parallel digital processor system for particle image velocimetry, Measurement Science and Technology 4, pp. 619.
[137] Meinhart, C.D., Wereley, S.T., Santiago, J.G., 1999, PIV measurements of a microchannel flow, Exp Fluids 27, pp. 414-419.
[138] Adrian, R.J., Westerweel, J., 2011, Particle image velocimetry, Cambridge University Press.
[139] Iwaki, C., Cheong, K.H., Monji, H., 2004, PIV measurement of the vertical cross-flow structure over tube bundles, Exp Fluids 37, pp. 350-363.
[140] Forliti, D.J., Strykowski, P.J., Debatin, K., 2000, Bias and precision errors of digital particle image velocimetry, Exp Fluids 28, pp. 436-447.
[141] Curr, R.M., Sharma, D., Tatchell, D.G., 1972, Numerical predictions of some three-dimensional boundary layers in ducts, Comput Method Appl M 1, pp. 143-158.
[142] Shah, R.K., London, A.L., Laminar Flow Forced Convection in Ducts: a Source Book for Compact Heat Exchanger Analytical Data, Supl. 1, 1978, Academic Press, New York.
[143] Kakaç, S., Shah, R.K., Aung, W., 1987, Handbook of single-phase convective heat transfer,

Wiley New York et al.
[144] Taguchi, G., Chowdhury, S., Wu, Y., 2004, Quality Engineering: The Taguchi Method, John Wiley & Sons, Inc., pp.*56-123.
[145] Sahnoun, A., Webb, R.L., 1992, Prediction of Heat Transfer and Friction for the Louver Fin Geometry, Journal of Heat Transfer 114, pp. 893-900.
[146] Lee, P., Garimella, S.V., 2006, Thermally developing flow and heat transfer in rectangular microchannels of different aspect ratios, Int J Heat Mass Tran 49, pp. 3060-3067.
[147] Bar-Cohen, A., Arik, M., Ohadi, M., 2006, Direct liquid cooling of high flux micro and nano electronic components, P Ieee 94, pp. 1549-1570.
[148] Lee, Y.J., Lee, P.S., Chou, S.K., 2013, Hotspot Mitigating With Obliquely Finned Microchannel Heat Sink - An Experimental Study, Components, Packaging and Manufacturing Technology, IEEE Transactions on 3, pp. 1332-1341.
[149] Phillips, R.J., 1987, Forced-convection, liquid-cooled, microchannel heat sinks, M.S., Massachusetts Institute of Technology, Cambridge.
[150] Kandlikar, S., Garimella, S., Li, D., 2005, Heat transfer and fluid flow in minichannels and microchannels, Access Online via Elsevier.

APPENDIX A: Laminar flow friction factor in the entrance region of rectangular ducts

Laminar flow friction factor in the entrance region of rectangular ducts [149, 150]

$x^+=(x/D_h)/Re$	*f Re*			
	$\alpha^*=1.0$	$\alpha^*=0.5$	$\alpha^*=0.2$	$\alpha^*\leq 0.1$ $\alpha^*\geq 10$
0	142.0	142.0	142.0	287.0
0.001	111.0	111.0	111.0	112.0
0.003	66.0	66.0	66.1	67.5
0.005	51.8	51.8	52.5	53.0
0.007	44.6	44.6	45.3	46.2
0.009	39.9	40.0	40.6	42.1
0.01	38.0	38.2	38.9	40.4
0.015	32.1	32.5	33.3	35.6
0.02	28.6	29.1	30.2	32.4
0.03	24.6	25.3	26.7	29.7
0.04	22.4	23.2	24.9	28.2
0.05	21.0	21.8	23.7	27.4
0.06	20.0	20.8	22.9	26.8
0.07	19.3	20.1	22.4	26.4
0.08	18.7	19.6	22.0	26.1
0.09	18.2	19.1	21.7	25.8
0.10	17.8	18.8	21.4	25.6
0.20	15.8	17.0	20.1	24.7
≥ 1.0	14.2	15.5	19.1	24.0

APPENDIX B: A simplified schematic of Simulink simulation

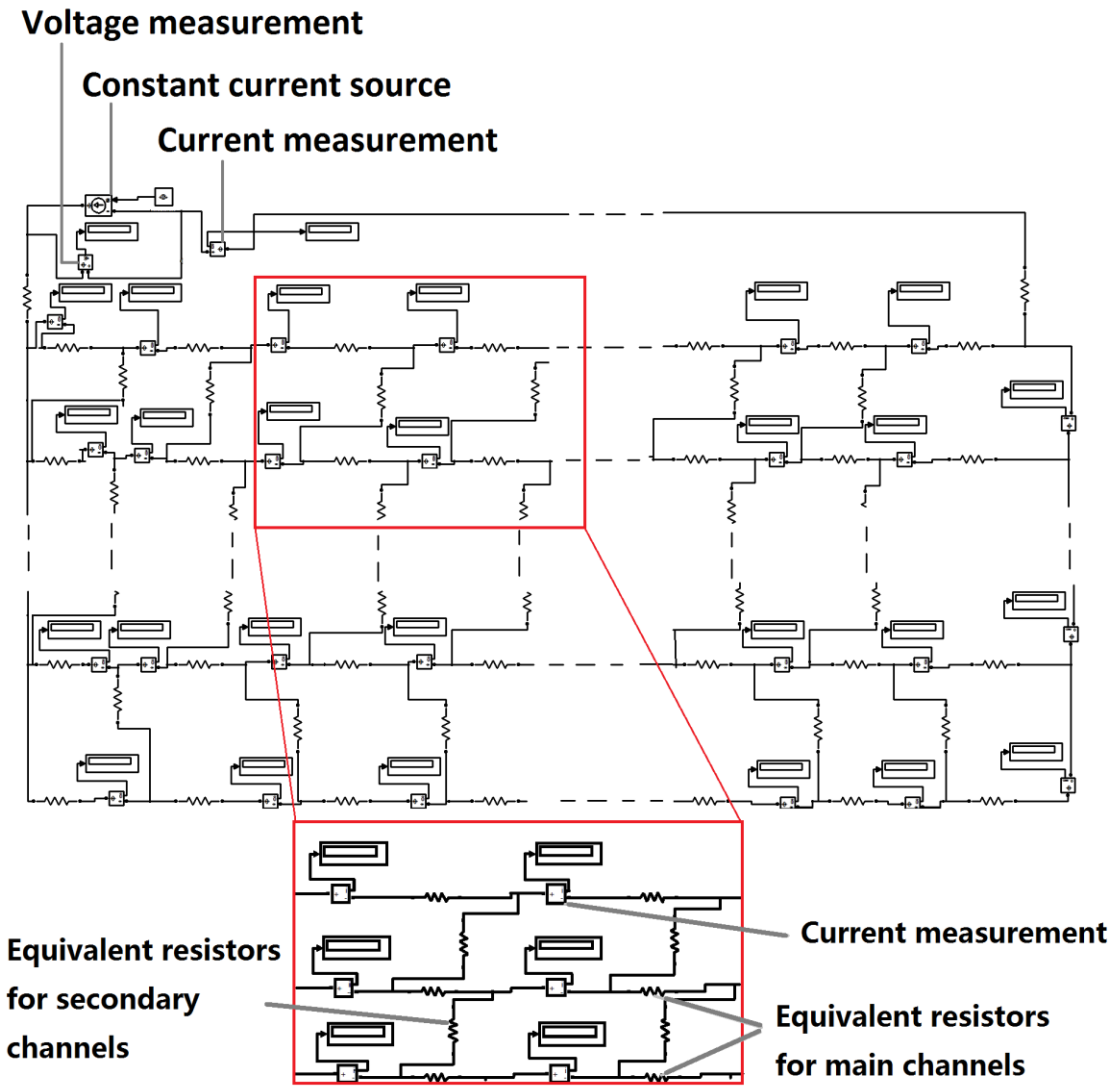

APPENDIX C: Dimension details of 64 simulation cases for Taguchi method

Re	H/w_{ch}	H /mm	θ / °	l_u /mm	w_u /mm	w_{ob} /mm	D_h /mm	u / m/s	l /mm	W_w /mm
30	0.3	0.096	20	2	1	0.2	0.2	0.151	1.8	0.677
30	0.8	0.208	23	2	1	0.4	0.3	0.100	1.6	0.739
30	1.3	0.307	26	2	1	0.6	0.4	0.075	1.4	0.763
30	1.8	0.379	29	2	1	0.8	0.5	0.060	1.2	0.789
30	2.3	0.421	32	2	1	1	0.6	0.050	1	0.817
30	2.8	0.437	35	2	1	1.2	0.7	0.043	0.8	0.844
30	3.3	0.437	38	2	1	1.4	0.8	0.037	0.6	0.867
30	3.8	0.431	41	2	1	1.6	0.9	0.033	0.4	0.886
160	0.3	0.098	38	2	1	1	0.3	0.535	1	0.673
160	0.8	0.060	41	2	1	1.2	0.2	0.803	0.8	0.924
160	1.3	0.198	32	2	1	1.4	0.5	0.321	0.6	0.848
160	1.8	0.132	35	2	1	1.6	0.4	0.401	0.4	0.926
160	2.3	1.233	26	2	1	0.2	0.7	0.229	1.8	0.464
160	2.8	1.061	29	2	1	0.4	0.6	0.267	1.6	0.621
160	3.3	1.840	20	2	1	0.6	0.9	0.178	1.4	0.442
160	3.8	1.493	23	2	1	0.8	0.8	0.200	1.2	0.607
290	0.3	0.161	35	2	1	0.4	0.4	0.728	1.6	0.461
290	0.8	0.376	32	2	1	0.2	0.5	0.582	1.8	0.529
290	1.3	0.073	38	2	1	0.8	0.2	1.456	1.2	0.944
290	1.8	0.173	41	2	1	0.6	0.3	0.971	1.4	0.904
290	2.3	0.779	20	2	1	1.2	0.8	0.364	0.8	0.661
290	2.8	1.143	23	2	1	1	0.9	0.323	1	0.592
290	3.3	0.276	26	2	1	1.6	0.6	0.485	0.4	0.916
290	3.8	0.418	29	2	1	1.4	0.7	0.416	0.6	0.89
420	0.3	0.170	26	2	1	1.2	0.5	0.844	0.8	0.43
420	0.8	0.174	29	2	1	1	0.4	1.055	1	0.781
420	1.3	0.104	20	2	1	1.6	0.3	1.406	0.4	0.919
420	1.8	0.063	23	2	1	1.4	0.2	2.110	0.6	0.965
420	2.3	1.261	38	2	1	0.4	0.9	0.468	1.6	0.451
420	2.8	1.493	41	2	1	0.2	0.8	0.527	1.8	0.467
420	3.3	0.889	32	2	1	0.8	0.7	0.602	1.2	0.73
420	3.8	0.970	35	2	1	0.6	0.6	0.703	1.4	0.745
550	0.3	0.226	41	2	1	1.2	0.7	0.789	0.8	0.245
550	0.8	0.323	38	2	1	1.4	0.8	0.690	0.6	0.596
550	1.3	0.175	35	2	1	1.6	0.5	1.105	0.4	0.865

550	1.8	0.216	32	2	1	1.8	0.6	0.921	0.2	0.88
550	2.3	0.346	29	2	1	0.4	0.3	1.842	1.6	0.849
550	2.8	0.472	26	2	1	0.6	0.4	1.381	1.4	0.831
550	3.3	0.032	23	2	1	0.8	0.1	5.526	1.2	0.99
550	3.8	0.080	20	2	1	1	0.2	2.763	1	0.979
680	0.3	0.096	23	2	1	1.4	0.3	2.277	0.6	0.679
680	0.8	0.179	20	2	1	1.2	0.4	1.708	0.8	0.775
680	1.3	0.026	29	2	1	1.8	0.1	6.832	0.2	0.98
680	1.8	0.059	26	2	1	1.6	0.2	3.416	0.4	0.967
680	2.3	0.837	35	2	1	0.6	0.7	0.976	1.4	0.636
680	2.8	1.387	32	2	1	0.4	0.8	0.854	1.6	0.505
680	3.3	0.279	41	2	1	1	0.5	1.366	1	0.915
680	3.8	0.637	38	2	1	0.8	0.6	1.138	1.2	0.832
810	0.3	0.240	29	2	1	1.6	0.8	1.017	0.4	0.198
810	0.8	0.259	26	2	1	1.8	0.7	1.162	0.2	0.675
810	1.3	0.347	23	2	1	1.2	0.6	1.356	0.8	0.733
810	1.8	0.261	20	2	1	1.4	0.5	1.627	0.6	0.855
810	2.3	0.227	41	2	1	0.8	0.4	2.034	1.2	0.901
810	2.8	0.118	38	2	1	1	0.3	2.712	1	0.958
810	3.3	0.158	35	2	1	0.4	0.2	4.069	1.6	0.952
810	3.8	0.034	32	2	1	0.6	0.1	8.138	1.4	0.991
940	0.3	0.115	35	2	1	1.8	0.4	2.361	0.2	0.614
940	0.8	0.092	32	2	1	1.6	0.3	3.148	0.4	0.884
940	1.3	0.058	41	2	1	1.4	0.2	4.722	0.6	0.955
940	1.8	0.027	38	2	1	1.2	0.1	9.44	0.8	0.985
940	2.3	0.848	23	2	1	1	0.8	1.18	1	0.631
940	2.8	1.069	20	2	1	0.8	0.7	1.34	1.2	0.618
940	3.3	0.972	29	2	1	0.6	0.6	1.574	1.4	0.705
940	3.8	1.165	26	2	1	0.4	0.5	1.889	1.6	0.693

APPENDIX D: The calculation steps of using reduced equivalent circuit model

1. Determination of dimension details of the fin heat sink

2. Calculation of *fRe* for main channels and secondary channels.

3. Calculation of hydraulic resistances for main channels and secondary channels.

4. Building the equivalent circuit in Simulink and assignment of resistors and current source.

5. Running of calculation.

6. Exporting the results of mass flow distribution to Excel.

7. Calculation of the heat transfer coefficient.

8. Calculation of the thermal resistances.

9. Calculation of the fluid temperature of each unit.

10. Calculation of the temperature of substrate base.